UNIVERSITY OF UDINE

Department of Electrical, Management and Mechanical Engineering

Doctorate School in Industrial and Information Engineering
- XXV Cycle -

Doctoral Thesis

STRUCTURAL ANALYSIS OF MECHANICAL COMPONENTS UNDER THERMAL LOADS

AN INDUSTRY-ORIENTED APPROACH

Supervisor:
Prof. FRANCESCO DE BONA

Candidate:
LUCIANO MORO

2013

A chi mi fa sorridere

”The pursuit of knowledge is hopeless and eternal”

Hubert J. Farnsworth - 2011

”A posto... Via!”

Carlo Lesa - Everyday

Abstract

This thesis investigates the structural behavior of mechanical components in presence of thermal loads. In many engineering situations there are evidences of failures related to parts that are not free to expand, and a carefully evaluation of stress and strain field related to the temperature distribution is crucial to prevent costly and catastrophic effects, or to provide suitable fire-resistive devices.

In the first part of the work the mechanisms which give rise to thermal stresses are investigated. In order to assess some basic problem solving techniques that can be of practical use in an industry-oriented approach, simplified models are developed. Material behavior under cyclic loading conditions has been investigated to individuate the best strategy to modeling cyclic plasticity and to obtain accurate life predictions in presence of thermal fatigue.

Examples concerning metallurgical plants and naval engineering are investigated in the second part of the thesis, where the interpretative models previously developed are shown to be capable of well describe the behavior of the components during operational conditions. Analytical and numerical models adopted to define stress levels and damage mechanisms are developed in order to guarantee a computational effort compatible for the daily industrial practice. The proposed thermo-mechanical analyses allow to detect some optimization parameters (related to both selected material and geometrical shape) that permits a longer life to be achieved. Furthermore, an experimental validation of the adopted methodologies is performed for a naval application, where temperature variation, as well as displacements induced by temperature gradients, have been monitored.

Contents

Abstract **vii**

List of Symbols **xi**

List of Figures **xv**

Introduction **1**

1 Thermal Loads: Theoretical Framework **3**
- 1.1 Overview of Heat Transfer 3
  - 1.1.1 Heat Transfer Mechanisms 4
  - 1.1.2 Simultaneous Heat Transfer Mechanisms 10
  - 1.1.3 Closed-Form Solutions 13
- 1.2 Thermal Stress 19
  - 1.2.1 Free Expansion 21
  - 1.2.2 Conversion of Thermal to Mechanical Strain 21
  - 1.2.3 Partial Constraint 22
  - 1.2.4 Simple Three- and Two-Dimensional Problems 24
  - 1.2.5 Problem Solving Technique 25
  - 1.2.6 Closed Form Solutions 28
- 1.3 Numerical Methods and Temperature Effects on Metals 35

2 Damage Induced by Repeated Thermal Loads **49**
- 2.1 Cyclic Thermal Stress 49
  - 2.1.1 Effect of Repeated Heating and Cooling 50
  - 2.1.2 Ratcheting 52
- 2.2 Considerations About Modeling of Cyclic Plasticity 55
  - 2.2.1 Plastic Behavior in Monotonic Loading 55
  - 2.2.2 Plastic Behavior in Cyclic Loading 58
  - 2.2.3 Simulated Cyclic Behavior 62
  - 2.2.4 Cyclic Stress-Strain Curve 72

2.3 Fatigue-Life Relations 75
    2.3.1 Stress- and Strain-Based Approach 75
    2.3.2 Critical Comparison 77
    2.3.3 High Temperature and Fatigue 82
    2.3.4 Predictive Models 84

3 Steel Industry Applications 89
3.1 Thermo-Mechanical Analysis of an Anode 90
    3.1.1 Component Description 90
    3.1.2 FE Model and Behavior After a Single Heating 91
    3.1.3 Considerations About Selected Materials 95
    3.1.4 Behavior Under Repeated Thermal Loads 98
3.2 Design Improvements for a Copper Mold 102
    3.2.1 Component Description 102
    3.2.2 Numerical Results and Interpretative Models 103
    3.2.3 Cycling Loads and Life Assessment 110
    3.2.4 Design Improvements 115

4 Naval Application: Fire Doors 121
4.1 Component Description 121
4.2 Experimental Observation During Standard Fire Tests 122
4.3 Thermo-Structural Analysis 128

Conclusions 137

Bibliography 141

List of Symbols

α	Coefficient of thermal expansion
ΔH_m	Enthalpy of melting, latent heat of fusion
ΔH_s	Enthalpy of sublimation
ΔH_v	Enthalpy of vaporization
ΔT	Temperature range
$\dot{Q}$	Rate of heat transfer
$\dot{q}$	Heat flux
κ	Thermal diffusivity
λ	Conductivity
μ	Auxiliary parameter
ν	Poisson's ratio
$\overline{\sigma}$	Stefan-Boltzmann constant
ρ	Density
σ_l	Endurance limit
σ_y	Yield stress
σ'_y	Cyclic yield stress
$\sigma_{1,2,3}$	Principal stress in 1, 2, 3 direction
$\sigma_{r,\vartheta,z}$	Stress in r-, ϑ-, z-direction
σ_{UTS}	Ultimate tensile strength

σ_{VM}	Von Mises stress
$\sigma_{x,y,z}$	Stress in x-, y-, z-direction
$\varepsilon_{1,2,3}$	Principal strain in 1-,2-, 3-direction
ε_{cr}	Creep strain
ε_{el}	Elastic strain
ε_{mec}	Mechanical strain
ε_{pl}	Plastic strain
$\varepsilon_{r,\vartheta,z}$	Strain in r-, ϑ-, z-direction
ε_{th}	Thermal strain
ε_{tot}	Total strain
$\varepsilon_{x,y,z}$	Strain in x-, y- z-direction
A	Heat transfer area
a, K	Coefficient terms of stress-life relation
c	Specific heat
C, γ	Chaboche model parameters
C_1, C_2,...	Constants of integration
C_1', C_2',...	Constants of integration
C_1'', C_2'',...	Constants of integration
D	Ductility
E	Young's modulus
e	Emissivity
E_t	Tangent modulus
G, b	Non-linear hardening law parameters
h	Convective heat transfer coefficient
H', n'	Parametres of cyclic stress-strain curve

I, J	Auxiliary functions
L	Thickness
l	Lenght
m	Mass
N_f	Number of cycles to failure
N_s	Number of sequences to failure
P	External load
Q	Amount of heat transfer
r	Radius
R_{cond}	Conductive thermal resistance
R_{conv}	Convective thermal resistance
$r_{i,f,e}$	Internal, frontier, external radius
R_{rad}	Radiative thermal resistance
RA	Reduction in area
T	Temperature
t	Time
T_0	Reference temperature (no stress)
T_∞	Bulk temperature
T_a	Ambient temperature
$T_{1,2}$	Temperature on the sides of the plate
T_{fi}	Fire temperature
$T_{i,f,e}$	Temperature at the internal, frontier, external radius
U	Internal energy
u	Displacement
V	Volume

W, N	Auxiliary functions
X, Y	Coefficient terms of total strain-life relation
x, y	Exponent terms of total strain-life relation

List of Figures

1.1 Conduction in a plane wall. 5
1.2 Schematic representation of thermal-electrical analogy: (a) series connection, (b) parallel connection. 7
1.3 Convection in a plane wall. 8
1.4 Radiation in a plane wall. 9
1.5 Plane wall subjected to initial (IC) and boundary (BC) conditions. 11
1.6 Temperature distribution into the plate. 13
1.7 Temperature distribution in a plane wall subjected to given temperatures on the surfaces. 16
1.8 Temperature evolution in radiative cooling of a billet. 17
1.9 Hollow cylinder subjected to heat flow and convective cooling. 20
1.10 Free expansion after heating. 21
1.11 Complete conversion of thermal to mechanical strain. 22
1.12 Two-bar assembly in which only one bar is heated. 23
1.13 Stress trends in two-bar assembly related to areas ratio. 24
1.14 (a) Confined hot region into a cold volume. (b) Confined hot area. 25
1.15 Steps to follow in solving problems involving thermal stresses. 27
1.16 Scheme of thermal stresses problem in a plate. 29
1.17 Thermal stresses in an hollow cylinder for different constraints and temperature distributions. 34
1.18 Coupled and uncoupled thermo-mechanical analysis. 36
1.19 Variation of (a) thermal conductivity and (b) specific heat of steel against temperature. 38
1.20 Variation against temperature of (a) thermal expansion and (b) reduction factors for Young's modulus and yield stress. . . 39
1.21 Strain vs. time curve under constant load and temperature. 1) primary creep, 2) secondary creep, 3) tertiary creep. 41
1.22 Phase changes from one state to another. 42

1.23 Temperature variation against time and enthalpy variation against temperature during phase changes. 43
1.24 Simple problem involving phase change. 44
1.25 Temperature distribution during transient heating. 46
1.26 Stress distribution after heating. 46
1.27 Techniques to simulate melting: (a) removed elements , (b) room temperature imposed and (c) melting temperature imposed. 47

2.1 Bar constrained at its ends and cyclically heated. 50
2.2 σ-ε curves for increasing values of temperature range: a) ΔT_1 not inducing plastic flow, b)$\Delta T_2 > \Delta T_1$ inducing plastic flow in tension, c) $\Delta T_3 > \Delta T_2$ inducing plastic flow in both tension and compression. 51
2.3 Elastic, plastic and thermal strain versus time when a high temperature range is applied. 52
2.4 Two-bar assembly in which only one bar is heated and a load is applied. 53
2.5 σ-ε curve in presence of ratcheting. 54
2.6 Elastic and plastic strain in a monotonic tensile test. 56
2.7 (a) Elastic-perfectly plastic model and (b) Elastic-linear work-hardening model. 57
2.8 (a) Elastic-exponential hardening model and (b) Chaboche model. 58
2.9 (a) Strain-controlled test with cyclically (b) softening and (c) hardening material response. 59
2.10 Examples of yield surfaces in principal stress space. 60
2.11 Schematic evolution of isotropic hardening model. 61
2.12 Schematic evolution of kinematic hardening model. 62
2.13 Evolution of yield surface in a combined model. 63
2.14 Loading conditions investigated: (s) stress-controlled, (b) strain-controlled, (c) thermal and (d) thermo-mechanical load. 64
2.15 Numerical models adopted in simulations. 64
2.16 Stress-strain cycle in a stress-controlled test. (a) Scheme of the simulation, (b) isotropic hardening model, (c) kinematic hardening model and (d) combined model. 68
2.17 Stress-strain cycle in a strain-controlled test. (a) Scheme of the simulation, (b) Isotropic hardening model, (c) kinematic hardening model and (d) combined model. 69

2.18 Stress-strain cycle in a thermal stressed component. (a) Scheme of the simulation, (b) Isotropic hardening model, (c) kinematic hardening model and (d) combined model. 70
2.19 Stress-strain cycle in a thermo-mechanical stressed component. (a) Scheme of the simulation, (b) Isotropic hardening model, (c) kinematic hardening model and (d) combined model. 71
2.20 Cyclic stress-strain curve. 72
2.21 Numerically evaluated cyclic stress-strain curve for copper. . . 74
2.22 (a) Fatigue in a railcar axle and (b) example of S-N curve. . . 76
2.23 Scheme of a ε-N curve. 77
2.24 Schematic of S-N to ε-N conversion. 78
2.25 Example of conversion of S-N curve into ε-N curve. 80
2.26 Example of conversion of S-N curve into ε-N curve. 81
2.27 (a) Isothermal, (b) thermal and (c) thermo-mechanical fatigue. 83
2.28 Schematic of fatigue-creep test. 84
2.29 Simplified approach to obtain a S-N curve from static tensile properties. 85
2.30 Universal Slopes method. 87

3.1 Geometry of the component. 91
3.2 Finite element model of the component. 92
3.3 Temperature contour map after a single heating with close view of molten region. 93
3.4 Techniques to simulate melting: (a) removed elements , (b) room temperature imposed and (c) melting temperature imposed. 94
3.5 Von Mises stress contours after heating with $\dot{q}_{min}$: (a) removed elements , (b) room temperature imposed and (c) melting temperature imposed. 95
3.6 Cyclic stress-strain curves for materials under investigation. . 97
3.7 Equivalent strain range versus cycles to failure. 97
3.8 Load cycles. 98
3.9 Von Mises stress contours (a) after heating up to $\dot{q}_{max}$, (b) after cooling to room temperature. 99
3.10 Interpretative models referring to temperature distribution. . . 100
3.11 Stress-strain hysteresis loops: (a) annealed and (b) cold worked copper. 101
3.12 Geometry of the component. 103
3.13 Inner mold surface with closed view of the meniscus region with cracks. 104
3.14 Top view of 3-D FE mechanical model. 104

3.15 (a) Temperature and (b) stress distribution during operative condition. 105
3.16 Interpretative models referring to temperature distribution. . . 106
3.17 Stress variation through the thickness at the corner. 106
3.18 Stress variation through the thickness in the hottest part. . . . 107
3.19 Principal stresses on the mold surface along the axial direction. 108
3.20 Hollow cylinder constituted by a "hot" and a "cold" part. . . . 109
3.21 Stress distribution according to the proposed structural model. 110
3.22 Scheme of the macro-cycle. 111
3.23 Scheme of the micro-cycle. 111
3.24 Stress-strain macro-cycles and micro-cycles. 112
3.25 Manufacturing operation to obtain the tensile-test specimens. 113
3.26 Equivalent strain range versus cycles to failure 114
3.27 Sensitivity analysis related to width variation of cold area. . . 115
3.28 Top view of (a) reference and (b, c) enhanced mold configurations. 116
3.29 Hoop stress distribution in an hollow cylinder with a modified upper portion. 117
3.30 Axial stress distribution in an hollow cylinder with a modified upper portion. 117
3.31 Example of enhanced mold design. 118
3.32 Schematic of (a) strain range, (b) cycles to failure and (c) sequences to failure against meniscus fluctuation frequency. . . 119

4.1 Naval fire door assembly, with a closed view of the insulating material. 122
4.2 Experimental set up: thermocouples, thermographic camera, laser sensor and real-time controller. 123
4.3 Average temperature inside the furnace. 125
4.4 Images from thermographic camera during the test. 126
4.5 Temperature trends at different locations. 126
4.6 Typical deformed shape of fire doors during the test. 127
4.7 Measured gap between leaf and frame during the test. 127
4.8 (a) Finite element model of the leaf and (b) numerical temperature distribution. 129
4.9 Temperatures of (a) the exposed side and (b, c) of the unexposed side. 130
4.10 Strategies of thermal analysis implemented: (a) transient (b) steady state. 131
4.11 Finite element model of leaf, frame and bulkhead structure. . . 132
4.12 Simulated temperature distribution of the structure. 133

4.13 Out of plane displacements of the structure. 134

Introduction

Stress is not a consequence of mechanical loads only: when a body, or a part of it, is not free to expand or contract in response to changes in temperature, stress may arise. Thermal expansion or contraction can be totally or partially restrained because of body geometry, external constraints or presence of temperature gradients. Such stress caused by a temperature distribution is known as *thermal stress*. Many engineering situations, from aerospace structures to steel-making plants, involve failures related to thermal stress, which effects are often costly and catastrophic. For this reasons, it is crucial to recognize the importance of reduction of thermal stresses in mechanical parts, which often can not be achieved by simply over sizing the component. Furthermore, the behavior of structures in presence of heating sources is fundamental in the design of fire-resistive environments.

This research work focuses on the structural analysis of mechanical components under thermal loads.

The first part of the thesis provides an overview of the theoretical framework about thermal stress that has been developed over years, in order to assess some basic problem solving techniques. Particular attention has been devoted to achieve analytical and numerical strategies that can be of practical use in an industry-oriented approach: interpretative analytical models are developed to gain insights into mechanisms which give rise to thermal stresses and to quickly assess the relevant parameters suitable for design optimization; plasticity models, as well as mechanical behavior under cyclic loads, are investigated in order to evaluate the progressive damage of the component and to perform accurate life predictions; numerical methods are also treated as an useful tool, especially dealing with coupled problems involving complex geometries and loading conditions. Numerical calculations and simulations are performed adopting ANSYS®and MATLAB®commercial software. Some examples of developed lines of code are provided across the work to further help the reader to become familiar about the implementation of a particular concept or loading condition. Although commands are specific for the adopted one, similar procedures can be used also for different software.

Examples concerning metallurgical plants and naval engineering are deeply investigated in the second part of the thesis, where the interpretative models previously developed are shown to be capable of well describe the behavior of the components during operational conditions. Analytical and numerical models adopted to define stress and strain levels are developed in order to guarantee a computational effort compatible for the daily industrial practice.

The thesis is organized in four chapters, as described in the following:

In Chapter 1 heat transfer mechanisms and the rise of thermal stress from temperature distribution are briefly revised. Usually the structural designer is not used to perform thermal calculations, but a correct evaluation of the temperature field is a crucial aspect in order to obtain accurate results in terms of stress and strain. Chapter 1 provides also some fundamentals about numerical methods with some useful guidelines for increasing the efficiency of the analysis and reducing the computational time. Temperature effects on metals, which should be taken into account dealing with stresses arising from temperature distribution, are also analyzed.

In Chapter 2 damage induced by repeated thermal loads, which are often present in engineering applications, is evaluated. Cyclic behavior of materials is considered, with particular focus about modeling of cyclic plasticity in relation to thermal stress problems. Fatigue-life relations are then treated, with a special focus on predictive models that can be of practical use in industrial design, when experimental data at high temperatures are often not available.

The remaining chapters are completely dedicated to application examples. In particular, Chapter 3 deals with the thermo-mechanical analysis of two elements of steel industry: an anode adopted in electric arc furnaces and a mold used in continuous casting processes. The behavior of these mechanical components under operative conditions is investigated in order to compare the performances of different materials and to find optimization strategies that can reduce stress levels and increase their life.

In Chapter 4 fire doors for naval applications are analyzed, comparing numerical results with measurements obtained from extensive campaign of experimental tests. Fires doors are subjected to standard fire tests to evaluate their fire resistance. If the model response under a simulated standard fire fits well with experimental measurements, different loading conditions, such as longer or real fire exposure, can be simulated. Furthermore, the behavior of doors with different size and shape can be achieved reducing the number of tests needed for extended applications.

Chapter 1

Thermal Loads: Theoretical Framework

In this chapter an overview of the remarkable mechanisms of thermal loads is given. Thermal stresses in a mechanical component arise from a particular temperature field of the element itself, combined with external constraints that restrain its free expansion. Usually the structural designer is not used to perform thermal calculations, but a correct evaluation of the temperature distribution is a crucial aspect in order to obtain accurate results in terms of stress and strain. For this reason an extended review of heat transfer mechanisms is here proposed, in order to assess some fundamental laws that will be adopted also in the following.

After these preliminary considerations, mechanisms which give rise to thermal stresses are treated, and some interpretative models are developed to gain insights into the structural behavior of simple structures. In practical application, further aspects need to be considered: complex geometries and loading conditions, as well as temperature effect on material properties and phase changes should be taken into account. Numerical methods represent a powerful tool to perform such calculations, but some simplifications are compulsory in order to obtain fast simulations, suitable for mechanical industry where timing is always restricted. However, the accuracy of results need to be preserved and simplified models need to maintain high levels of reliability, as proposed in the last section of the chapter.

1.1 Overview of Heat Transfer

Heat transfer mechanisms are deeply investigated in literature, and many heat transfer textbooks propose detailed dissertation about basic principles of heat transfer [1, 2, 3, 4, 5]. Usually structural designer are mainly concerned in evaluating the effects of mechanical loads, without a deep investigation on the causes that give rise to temperature fields that may lead to critical stress and strain into the component. Heat transfer mechanisms are then briefly revised, with the aim of asses some fundamental laws that will be adopted also when treating examples concerning metallurgical plants and naval engineering, proposed in Chapter 3 and 4.

Heat is defined as energy that can be transferred from one system to another as a consequence of temperature difference. It flows always from regions of higher temperature to regions of lower temperature. The basic modes in which the heat can be transferred are conduction, convection and radiation. In the following some key aspects of these mechanisms are presented. More detailed discussions can be found in many heat transfer textbooks [1, 4]. According to current practice, in the following the *amount* of heat transferred during the transfer of thermal energy is denoted by Q, while the *rate* of heat transfer per unit time is denoted by $\dot{Q}$. For a given time interval Δt these quantities can be related by the following expression.

$$Q = \int_0^{\Delta t} \dot{Q}\, \mathrm{d}x \tag{1.1}$$

The rate of heat transfer per unit area normal to the direction of heat transfer is named *heat flux* and it can be expressed as:

$$\dot{q} = \frac{\dot{Q}}{A} \tag{1.2}$$

being $\dot{q}$ is the heat flux and A the heat transfer area.

1.1.1 Heat Transfer Mechanisms

Conduction is the transfer of heat from one part of a body at a higher temperature to another part of the same body at a lower temperature, or from one body at a higher temperature to another body in physical contact with it at a lower temperature. The conduction process takes place at the molecular level and involves the transfer of energy from the more energetic molecules to those with a lower energy level [2]. In solids, energy exchange process is due to vibration of atoms in their sites that causes lattice waves. In solids that are good conductors of electricity (metals), this lattice vibration mechanism is only a small contribution to the energy transfer process and an additional mechanism of conductive heat transfer is present due to the motion of free electrons, which move in a similar way to molecules in a gas [6].

That's why good electrical conductors tend to be good thermal conductors. At the macroscopic level the rate of heat transfer $\dot{Q}$ is proportional to the temperature gradient, accordingly to the one-dimensional form of Fourier's law of heat conduction

$$\dot{Q} = -\lambda A \frac{\partial T}{\partial x} \tag{1.3}$$

and actually represents a current of heat (thermal energy) that flows in the direction of the steepest temperature gradient. Since the temperature gradient is negative, the minus sign is inserted to get positive value for the rate of heat transfer in the direction of decreasing temperature. λ is the thermal conductivity and it is a measure of the ability of the material to conduct heat. The behavior of thermal conductivity with increasing temperature is highly material dependent: at the absolute zero the conductivity is zero since there is no mechanism for heat transfer because atoms are not vibrating. Metals usually show maximum values at room temperature, and then the thermal conductivity decreases with increasing temperature. Insulating materials, on the contrary, are characterized by a thermal conductivity that increases with temperature. Example values of thermal conductivity at room temperature for various materials are given in [6], while in the last part of this chapter some considerations about the variation of conductivity against temperature are provided. An effective example of conduction mechanism is given in Figure 1.1 where heat transfer in a plane wall of thickness L, but of very large extent in both other directions, is considered. The wall has temperature T_1 on one side and T_2 on the other. If the thermal conductivity is considered to

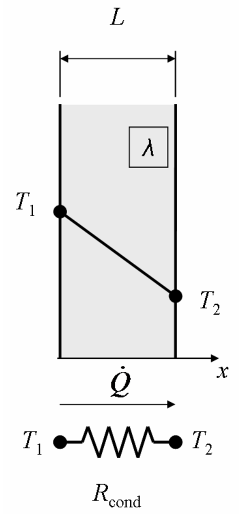

Figure 1.1: Conduction in a plane wall.

be constant, then Equation (1.3) can be directly integrated, thus obtaining:

$$\dot{Q} = \frac{\lambda A}{L}(T_2 - T_1) \tag{1.4}$$

Conduction heat transfer can be modeled adopting an electrical analogy, where current is represented by $\dot{Q}$ and the analogue of voltage difference is temperature difference $T_1 - T_2$. From this perspective the slab is a pure resistance to heat transfer and the conductive thermal resistance can be thus defined as:

$$R_{cond} = \frac{L}{\lambda A} \tag{1.5}$$

The electrical analogy may be used to solve more complex problems involving both series and parallel resistances, as for example in a composite planar heat transfer surface. As an example, the method can be adopted to solve the problem sketched in Figure 1.2a, in which the heat is transferred through several layers in a composite wall. The heat quantity in each phase is the same, and it can be modeled in the same way as current flowing in a series of electric resistances. Then from this analogy it is possible to express the amount of heat transferred as:

$$\dot{Q} = \frac{T_1 - T_2}{R_{tot}} = \frac{T_1 - T_2}{R_1 + R_2 + R_3} \tag{1.6}$$

where R_1, R_2, R_3 are the thermal resistances of each layer and can be evaluated from Equation (1.5). Figure 1.2b refers instead to a parallel thermal circuit, in which heat is transferred in parallel through several heat transfer conduits. In this case the amount of heat transferred is

$$\dot{Q} = \frac{T_1 - T_2}{R_{tot}} = \frac{T_1 - T_2}{\frac{1}{R_1 + R_2 + R_3}} \tag{1.7}$$

Convection is a mechanism of heat transfer between a flowing fluid, liquid or gas, and an adjacent solid object. The convective heat transfer increases if the fluid moves faster. For this reason the fluid motion is often induced by external means such as a pump or a fan. In this case the process is called forced convection. On the other hand, if the fluid motion occurs as a result of the density difference produced by the temperature difference, the process is called free or natural convection [1]. In convective processes the rate of heat transfer is observed to be proportional to the temperature difference, as expressed in Equation (1.8), which is known as Newton's law of cooling:

$$\dot{Q} = hA(T_\infty - T_1) \tag{1.8}$$

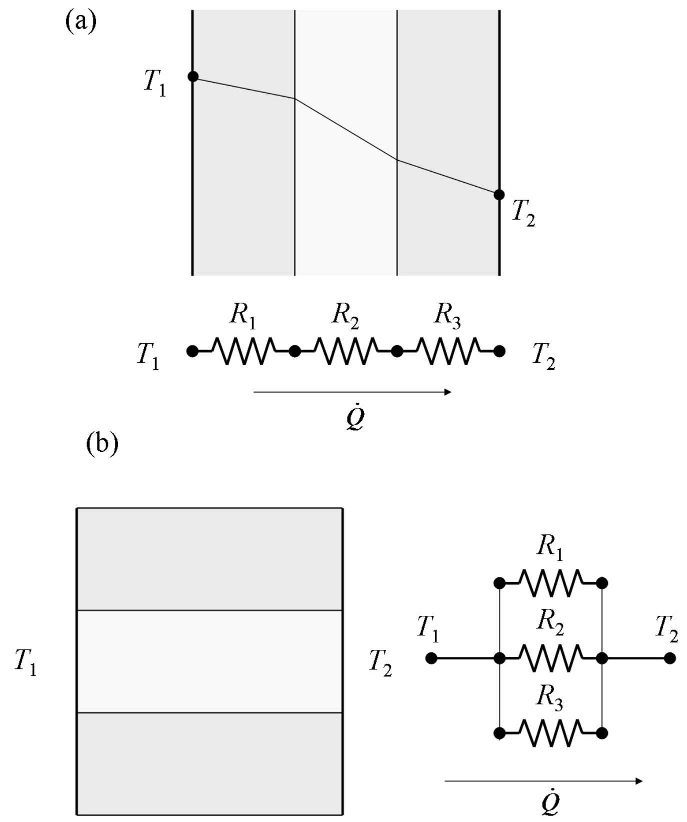

Figure 1.2: Schematic representation of thermal-electrical analogy: (a) series connection, (b) parallel connection.

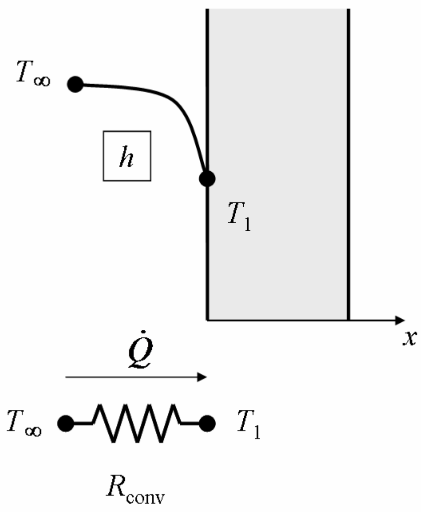

Figure 1.3: Convection in a plane wall.

Here T_1 is the surface temperature and T_∞ is the temperature of the fluid sufficiently far from the surface (also named *bulk* temperature). It has to be noted that at the surface the fluid assumes the same temperature of the solid, as sketched in Figure 1.3. The heat transfer coefficient h is related to the physical properties of the fluid, but it is also sensitive to variables influencing convection such as surface geometry and fluid velocity. There are also some special situations in which h can depend on the temperature difference [2]. Also for convective heat transfer it is useful for calculations to define a thermal resistance, given by:

$$R_{conv} = \frac{1}{hA} \tag{1.9}$$

Thermal *radiation* is electromagnetic radiation emitted by a body because of its temperature, at the expense of its internal energy. Unlike conduction and convection, radiation requires no medium for its propagation and it can travel in vacuum (this is how the energy of the sun reaches the earth). Thermal radiation is similar to other forms of electromagnetic radiation such as visible light, x-rays, and radio waves, differing in wavelengths and source of generation. Although radiative heat transfer is apparent when a hot body becomes self-luminous, all solids and liquids, as well as some gases, at a temperature above absolute zero emit thermal radiation [1]. On the macroscopic level, the calculation of thermal radiation is based on the Stefan-Boltzmann law, which relates the energy flux emitted by an ideal radiator (or blackbody)

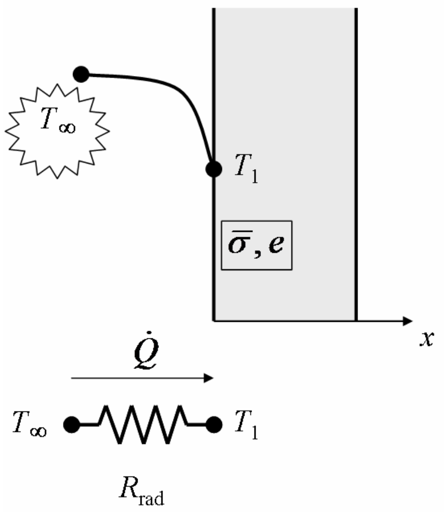

Figure 1.4: Radiation in a plane wall.

to the temperature, with the well known law:

$$\dot{Q} = \overline{\sigma} T^4 \tag{1.10}$$

in which $\overline{\sigma}$ is the Stefan-Boltzmann constant, with a value of $5.669 \cdot 10^{-8}$ W/(m^{2}K^4). It has to be noted that heat transfer from a radiating body increases much more rapidly with increasing temperature than conductive heat transfer (the heat exchange is proportional to the difference in T^4). Engineering surfaces in general do not perform as perfect emitters of radiant energy, and for real surfaces Equation (1.10) need to be modified:

$$\dot{Q} = e\overline{\sigma} T^4 \tag{1.11}$$

The term e is called the emissivity of the surface and has a value between 0 and 1. If a surface of emissivity e and surface area A at a temperature of T_1 is completely enclosed by a much larger surface (surroundings) at temperature T_∞, the net rate of radiation heat transfer between these two surfaces is:

$$\dot{Q} = \overline{\sigma} e A (T_\infty^4 - T_1^4) \tag{1.12}$$

When, because of the geometric arrangement, only a fraction of the energy leaving one surface is intercepted by the other surface, a further coefficient, usually called a shape factor or a view factor F_{12}, is needed in the right term of Equation (1.12). It is sometimes useful to express the radiation heat transfer as a linear function in the temperature difference between the surface temperature and the fluid temperature. As well as for conduction and convection, this procedure leads to obtain an equivalent thermal resistance:

$$R_{rad} = \frac{1}{\overline{\sigma} e A (T_\infty - T_1)(T_\infty^2 - T_1^2)} \tag{1.13}$$

It has to be noted that in this case the thermal resistance strongly depends on temperature. Equation (1.12) can then be expressed in analogous manner to conduction and convection, where the heat flow rate is function of a temperature difference:

$$\dot{Q} = \frac{(T_\infty - T_1)}{R_{rad}} \tag{1.14}$$

1.1.2 Simultaneous Heat Transfer Mechanisms

The aforementioned heat transfer mechanisms can act simultaneously in the same body: as an example, the outer surfaces of a hot steel bar will cool down as a result of heat lost by convection and radiation, while in the inner parts of the slab heat is transferred by conduction. The starting point in treating heat transfer planar problems with no internal heat generation and constant material properties is the general Fourier's Law:

$$\frac{\partial^2 T}{\partial x^2} = \frac{1}{\kappa}\frac{\partial T}{\partial t} \tag{1.15}$$

where κ is the thermal diffusivity, defined as:

$$\kappa = \frac{\lambda}{\rho c} \tag{1.16}$$

where λ is conductivity , c represents the specific heat and ρ the density. Equation (1.15) is a partial derivative equation (PDE) that requires adequate initial and boundary condition to be solved. A simple example involving one-dimensional heat transfer in the x-direction in a plate of thickness L, shown in Figure 1.5 is adopted to discuss the problem solving technique. If the plane wall is initially at temperature T_0, the initial condition can be expressed as:

$$T(x,0) = T_0 \tag{1.17}$$

being T_0 the initial temperature. Boundary conditions are related to the surfaces of the plate. Focusing only the left side of the plate ($x = 0$) several boundary conditions can be imposed, considering $T_{\infty,1}$ the bulk temperature related to this side. For example, a given, fixed temperature can be considered:

$$T(0,t) = T_{\infty,1} \tag{1.18}$$

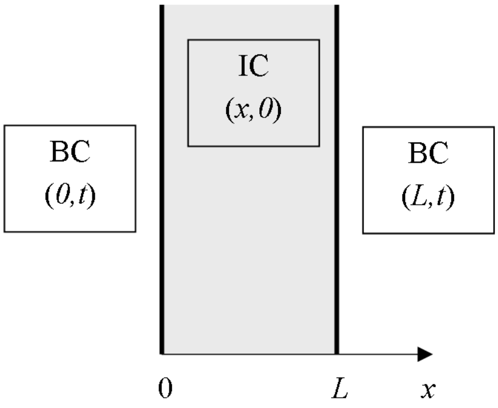

Figure 1.5: Plane wall subjected to initial (IC) and boundary (BC) conditions.

while a convective heat transfer can be imposed as:

$$-\lambda\frac{\partial T}{\partial x}=h(T_{\infty,1}-T(0,t)) \tag{1.19}$$

A radiative heat exchange is obtained with:

$$-\lambda\frac{\partial T}{\partial x}=\overline{\sigma}(T_{\infty,1}-T(0,t)^4) \tag{1.20}$$

This strategy can be applied also for the right side of the plate ($x = L$), where a bulk temperature $T_{\infty,2}$ is considered, and also when different mechanisms act on the same side, by simply superimposing the related boundary conditions. As an example, the plate is now considered to undergo a convective and radiative heating on the left side, while convective cooling acts on the right side. This situation is representative of thermal loading condition for a fire door subjected to standard fire test, whose thermo-mechanical behavior will be investigated in Chapter 4. The boundary conditions are then:

$$\begin{cases} -\lambda\dfrac{\partial T}{\partial x}=h(T_{\infty,1}-T(0,t))+\overline{\sigma}(T_{\infty,1}-T(0,t)^4) \\ -\lambda\dfrac{\partial T}{\partial x}=h(T_{\infty,2}-T(0,t)) \end{cases} \tag{1.21}$$

It is not possible to obtain analytic solutions of Equation (1.15) with all the proposed boundary conditions and, especially when radiative heat transfer mechanism is present, a PDE solver is required to achieve the solution. As an example, combining Equation (1.17) with Equation (1.21), Equation (1.15) can be numerically solved and the temperature distribution into the plate for any given time can be evaluated, as represented in Figure 1.6. The following MATLAB®command lines can be adopted to numerically solve the problem:

```
function CondConvIrr
global alfa Ti TA TB hA hB k sigma

TA=945+273;
Ti=20+273;
TB=Ti;
hA=25;
hB=10;
k=40;
ro=7800;
cp=500;
L=0.5;
sigma=5.6696*10e-8;
tf=60000;
alfa=k/ro/cp

m = 0;
x=linspace(0,L,50);
t = linspace(0,tf,200);
sol = pdepe(m,@pdeLap,@pdeLapic,@pdeLapbc,x,t);

function [c,f,s] = pdeLap(x,t,T,DTDx)
global alfa
c = 1/alfa;
f = DTDx;
s = 0;

function T0 = pdeLapic(x)
global Ti
T0 = Ti;

function [pl,ql,pr,qr] = pdeLapbc(xl,Tl,xr,Tr,t)
global hA hB k TA Ti sigma
pl = hA*(Tl-TA)+sigma*(Tl^4-TA^4)
ql = -k;
pr = Tr-Ti;
qr = k/hB;
```

On the other hand, if the set of boundary conditions is easy to handle and the geometry is simple, analytic solution can be achieved for both steady state and transient heat transfer adopting Equation (1.15) as a starting point. The following examples are described to clarify this aspect.

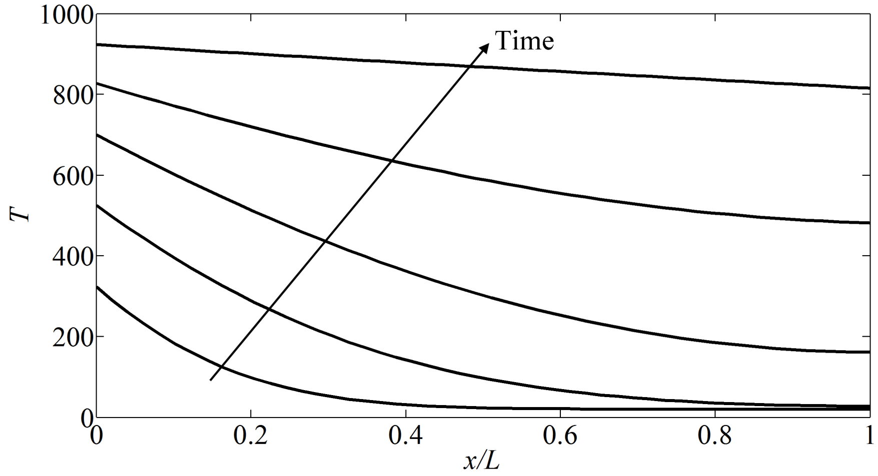

Figure 1.6: Temperature distribution into the plate.

1.1.3 Closed-Form Solutions

Heat transfer problems are often classified as being steady or transient. The term steady implies no change with time at any point within the medium, while transient implies variation with time or time dependence. Therefore, the temperature or heat flux is constant in time during steady heat transfer through a medium at any location. Most practical heat transfer problems are transient in nature, but they are usually analyzed under some presumed steady conditions since steady processes are easier to analyze. Transient analysis, in fact, usually requires more sophisticated techniques to obtain analytical solutions. In the following some simple problems involving transient and steady state heat transfer are analytically solved.

Transient heat transfer: analytic method

A slab of metal, initially at a temperature T_0 and then placed on a hot-plate is considered. Two hot-plates with different temperatures ($T_1 > T_2 > T_0$) are suddenly placed on the opposite faces. It is evident that the heat flowing into the metal would initially contribute to a temperature rise in the material, until ultimately a linear temperature gradient forms between the hot and cold faces, thus establishing a steady state heat transfer. Figure 1.5 can be adopted as an effective scheme of the problem, the boundary conditions being:

$$\begin{cases} T(0,t) = T_1 \\ T(L,t) = T_2 \end{cases} \tag{1.22}$$

The determination of the transient temperature distribution $T(x,t)$ can be obtained solving Equation (1.15). Introducing two new functions, $I(x)$ and $J(x,t)$, the temperature field can be written as:

$$T(x,t) = I(x) + J(x,t) \tag{1.23}$$

Equation (1.15) then leads to:

$$\frac{\mathrm{d}^2 I}{\mathrm{d}x^2} = 0 \tag{1.24}$$

and

$$\frac{\partial^2 J}{\partial J^2} = \frac{1}{\kappa}\frac{\partial J}{\partial t} \tag{1.25}$$

while the boundary conditions become:

$$\begin{cases} J(0,t) = T_1 - I(0) \\ J(L,t) = T_2 - I(L) \end{cases} \tag{1.26}$$

and the initial condition is represented by:

$$J(x,0) = T_0 - I(x) \tag{1.27}$$

In order to obtain an homogeneous boundary condition for J, the function I can be chosen as:

$$I(x) = T_1 + \frac{x}{L}(T_2 - T_1) \tag{1.28}$$

Equation (1.25) can be solved by separation of variables (it has to be noted that this would be the starting point if a symmetric temperature distribution, $T_1 = T_2$, occurred). Assuming that $J(x,t)$ can be re-written as:

$$J(x,t) = W(x)N(t) \tag{1.29}$$

and rearranging Equation (1.25), it is possible to obtain:

$$\frac{1}{L}\frac{\mathrm{d}^2 W}{\mathrm{d}x^2} = \frac{1}{\kappa N}\frac{\mathrm{d}N}{\mathrm{d}t} \tag{1.30}$$

Since W and N can be varied independently, the equality in Equation (1.30) can hold only if both sides are equal to a constant. For physical reasons (to avoid that the function N increases indefinitely with time), the required constant must be negative, and it is indicated by $-\mu^2$. Equation (1.30) can be transformed into the following equivalent system of ordinary differential equations:

$$\begin{cases} \dfrac{\mathrm{d}^2W}{\mathrm{d}x^2} + \mu^2 W = 0 \\ \dfrac{\mathrm{d}N}{\mathrm{d}t} + \mu^2 N = 0 \end{cases} \tag{1.31}$$

whose general solutions are:

$$\begin{cases} W = C_1 \cos(\mu x) + C_2 \sin(\mu x) \\ N = C_3 e^{-\kappa \mu t} \end{cases} \tag{1.32}$$

Substituting back into Equation (1.29) and combining C_1,C_2 and C_3 into only two constants (C_1' and C_2'), it is possible to obtain

$$J(x,t) = [C_1' \cos(\mu x) + C_2' \sin(\mu x)] e^{-\kappa \mu t} \tag{1.33}$$

The two boundary conditions of Equation(1.26) can now be applied in order to determine C_1' and C_2'. The first leads to $C_1' = 0$, while with the second gives $\sin(\mu x) = 0$. An infinite number of values of μ can satisfy this condition:

$$\mu_n = \frac{n\pi}{L}, n = 1, 2, 3... \tag{1.34}$$

Each value of μ_n yields an independent solution satisfying the Equation (1.34) as well as the two boundary conditions. Therefore an infinite number of independent solutions can be written, and the principle of superposition allows the creation of a more general solution by simple linear combination, obtaining

$$J(x,t) = \sum_{n=1}^{\infty} C_{2,n}' \sin(\mu_n x) e^{-\kappa \mu_n t} \tag{1.35}$$

The initial condition in Equation (1.27) is finally adopted to find the values of the constants $C_{2,n}'$:

$$J(x,0) = T_0 - I(x) = \sum_{n=1}^{\infty} C_{2,n}' \sin(\mu_n x) \tag{1.36}$$

This is the Fourier sine series representation of the function $T_0 - I(x)$, and, using the orthonormality property, it is possible to write:

$$C_{2,n}' = \frac{2}{L} \int_0^L (T_0 - I(x)) \sin(\mu_n x) \, \mathrm{d}x \tag{1.37}$$

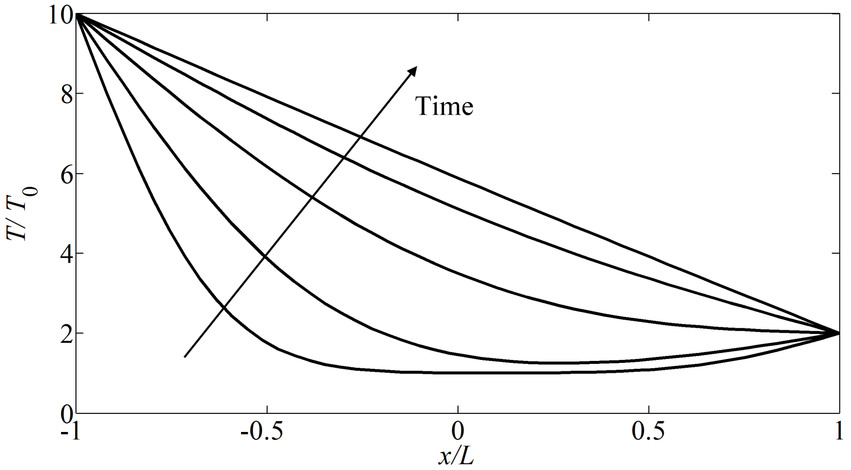

Figure 1.7: Temperature distribution in a plane wall subjected to given temperatures on the surfaces.

Equation (1.37) can be then solved, obtaining:

$$C'_{2,n} = -\frac{2T_0}{n\pi}[(-1)^n - 1] + \frac{2}{n\pi}[(-1)^n T_2 - T_1], n = 1, 2, 3... \tag{1.38}$$

Finally, combining Equation (1.38) with Equation (1.35), and considering Equation (1.28), the temperature field can be evaluated with Equation (1.23), thus obtaining:

$$T(x,t) = T_1 + \frac{x}{L}(T_2 - T_1) + \sum_{n=1}^{\infty} C'_{2,n} \sin(\mu_n x) e^{-\kappa \mu_n t}, n = 1, 2, 3 \tag{1.39}$$

Where $C'_{2,n}$ is expressed in Equation (1.38). Figure 1.7 shows the trend of temperature through the plane wall in different instants for the particular case in which $T_1 = 2T_2 = 10T_0$. As expected, starting from a sharp variation between the surfaces and the inner material, the temperature of the slab tends to rise, until ultimately a linear temperature gradient is reached establishing a steady state condition. The proposed methodology, based on the method of separation of variables, can be used also to evaluate the temperature distribution in case of convective boundary conditions on the sides of the walls, and also for other simply geometries involving cylindrical or spherical coordinates.

Transient heat transfer: lumped formulation

A simplified method of solving transient heat transfer problems is the lumped formulation method. It is useful in evaluating the temperature response of objects to changes in the environmental temperature. The term lumped implies that the entire object is represented by only one temperature, so no knowledge about temperature distribution in the object can be obtained [7]. In this section a simple problem of exchange of radiant energy is analyzed, in which a steel billet is initially at high temperature, T_{hot} and it loses heat by radiation from all of its surfaces to surroundings (at temperature T_∞), neglecting convective heat losses [8]. With a lumped transient analysis it is possible to find a relation between the temperature assumed from the billet and the time. Considering the internal energy of the billet as a function of its temperature only:

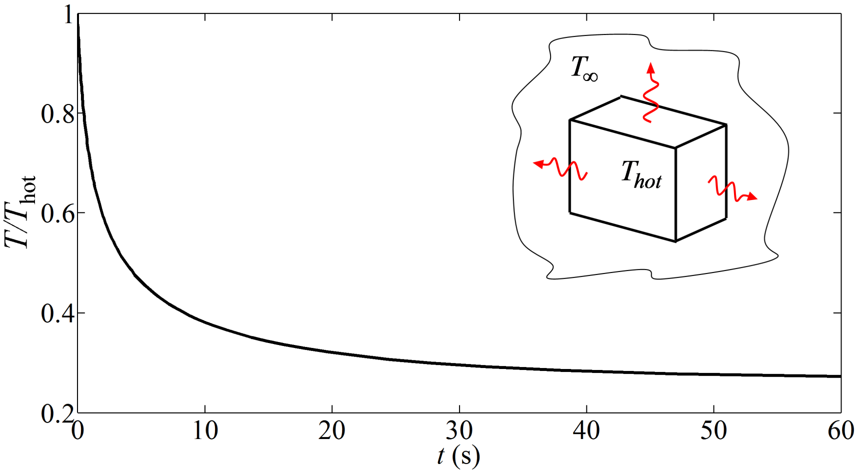

Figure 1.8: Temperature evolution in radiative cooling of a billet.

$$\mathrm{d}U = \rho V c \,\mathrm{d}T \tag{1.40}$$

If only radiative heat is present, combining Equation (1.40) with Equation (1.12) and integrating, it is possible to obtain:

$$t = \frac{\rho V c}{e\overline{\sigma}A} \int_{T_{hot}}^{T} \left(\frac{1}{T^4 - {T_\infty}^4} \right) \mathrm{d}T \tag{1.41}$$

where t is an arbitrary instant of time in which the billet assumes a temperature of T. The integral in equation (1.41) can be solved considering that:

$$\frac{1}{T^4 - {T_\infty}^4} = \frac{C_1}{T + T_\infty} + \frac{C_2}{T - T_\infty} + \frac{C_3 T + C_4}{T^2 - {T_\infty}^2} \tag{1.42}$$

where C_1, C_2, C_3 and C_4 are constant to be determined, and their values are:

$$C_1 = -\frac{1}{4{T_0}^3}, \quad C_2 = \frac{1}{4{T_0}^3}, \quad C_3 = 0, \quad C_4 = \frac{1}{2T_0} \tag{1.43}$$

The explicit form of equation (1.41) is then:

$$t = \frac{\rho V c}{e\overline{\sigma} A}\left[\frac{1}{4{T_\infty}^3}\ln\left(T - T_\infty\right) - \frac{1}{4{T_\infty}^3}\ln\left(T + T_\infty\right) - \frac{1}{2{T_\infty}^3}\tan^{-1}\left(\frac{T}{T_\infty}\right)\right]\Bigg|_{T_{hot}}^{T} \tag{1.44}$$

and the relation between time t and temperature T is plotted in Figure 1.8.

Steady state heat transfer

As previously mentioned, a state steady analysis, in which the temperature distribution reaches a stable condition without changes over time, does not usually require complex mathematical techniques. For example, considering the block studied in the previous paragraph, a steady state analysis will provide a solution in which the steel billet reaches the temperatures of the surroundings. Moreover, the final linear temperature distribution for the plane wall analyzed in Par.(1.1.3) can be quickly determined from Equation (1.3):

$$\frac{\partial T}{\partial x} = \text{const} \tag{1.45}$$

Integrating and considering that $T(0) = T_1$ and $T(L) = T_2$ the temperature distribution is then:

$$T(x) = T_1 - \frac{T_1 - T_2}{L}x \tag{1.46}$$

A steady state heat transfer in a hollow cylinder can be also considered. The inner surface (at $r = r_i$) is heated by a heat flux $\dot{q}$, while a convective cooling is applied on the external surface (at $r = r_e$). This problem is then characterized by the presence of two mechanisms, acting simultaneously: conduction and convection. The conduction across the thickness can be evaluated according to Equation (1.4) taking into account a cylindrical coordinate system:

$$\dot{q} = -\lambda\frac{dT}{dr} \tag{1.47}$$

Considering that $A = 2\pi r L$ and solving the integral, it is possible to find the value of the thermal resistance of the cylinder, according to Equation (1.5)

$$R_{cond} = \frac{r_i}{\lambda} \log \frac{r_e}{r_i} \tag{1.48}$$

Equation (1.9) can be instead adopted to evaluate the thermal resistance of the cooling fluid.

$$R_{conv} = \frac{r_i}{h r_e} \tag{1.49}$$

A series connection between the two thermal resistances can be considered, thus obtaining the temperature values on the inner and on the external surfaces of the cylinder.

$$\begin{cases} T_i = \dot{q}(R_{conv} + R_{cond}) + T_\infty \\ T_e = T_i - \dot{q} R_1 \end{cases} \tag{1.50}$$

In order to obtain the temperature distribution at any radial coordinate r, the equilibrium equation can be written as:

$$r \frac{\partial^2 T}{\partial r^2} + \frac{\partial T}{\partial r} = 0 \tag{1.51}$$

That can be re-written as

$$\frac{\partial}{\partial r} \left(\frac{\partial T}{\partial r} \right) = 0 \tag{1.52}$$

Obtaining

$$\frac{r \partial T}{\partial r} = \text{const} \tag{1.53}$$

And finally

$$T(r) = C_1 + \log r + C_2 \tag{1.54}$$

The value of constants C_1 and C_2 can be determined considering that the temperatures at $r = r_i$ and $r = r_e$ are given by Equation (1.50), obtaining:

$$T(r) = \frac{T_i - T_e}{\log \frac{r_i}{r_e}} \log \frac{r}{r_e} + T_e \tag{1.55}$$

1.2 Thermal Stress

Thermal stress is stress arising from temperature effects. Stress may arise from temperature distribution in several ways. As an example, non-uniform heating is one of the causes of thermal stress in mechanical components: when

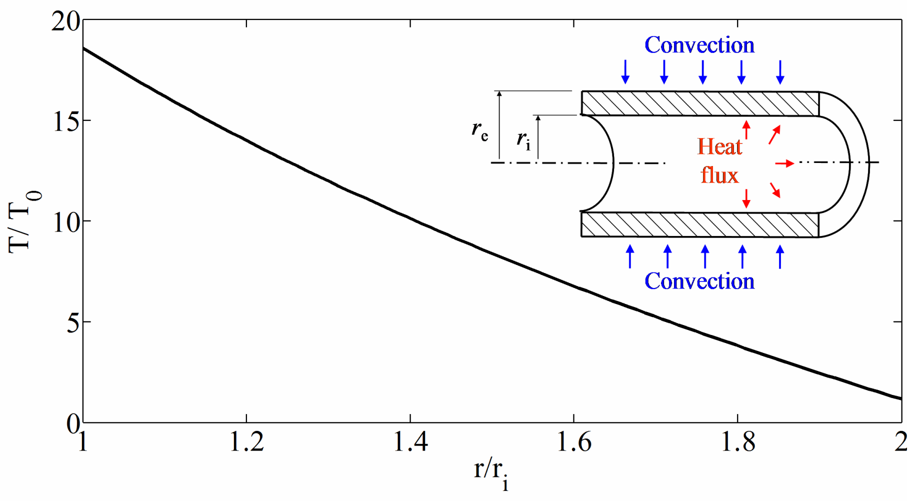

Figure 1.9: Hollow cylinder subjected to heat flow and convective cooling.

a material is subjected to a temperature gradient, the various fibers tend to expand proportionally to their temperature with different amounts. Since the body needs to remain continuous, thermal strains and associated thermal stress arises accordingly to the shape of the body and the temperature distribution. Thermal stress may also occur in cases with no temperature gradient, when the free expansion of the body is somewhat restrained by external constraints. Another cause is the simultaneous presence of materials having different coefficients of expansion in the heated component. In any case, it is not thermal expansion itself that causes stresses, but rather its constraint, as pointed out in [9, 10].

The mechanisms responsible to the rise of thermal stresses are presented in the following paragraphs, taking advantage of simple geometries and loading conditions. A monodimensional problem is adopted to firstly describe a favorable condition, where the component is completely free to expand. As it will be shown, no stresses develop in this situation. A complete conversion of thermal to mechanical strain is then discussed, while a partial conversion is treated as representative of real situations. The technique to be adopted when solving thermal stress problems is then briefly reviewed, and some examples of closed form solution are proposed. These simple problems allows to assess the basic theoretical frame that is necessary to treat more complicated situations, such those proposed in Chapter 3 and 4.

1.2.1 Free Expansion

A simple monodimensional problem, depicted in Figure 1.10, is adopted to describe a free expansion of a component. A metal bar is considered heated from the reference temperature T_0, at which the material does not show thermal expansion, to a final temperature T_1, being $\Delta T = T_1 - T_0$. The bar is isostatically loaded, so its free expansion is allowed on the right side, and the final elongation Δl can be calculated as:

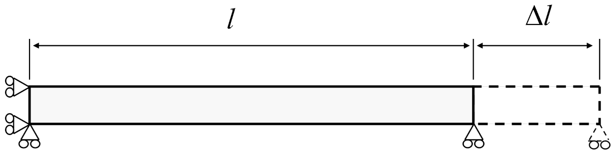

Figure 1.10: Free expansion after heating.

$$\Delta l = \alpha l \Delta T \tag{1.56}$$

where l is the initial length and α is the coefficient of thermal expansion. For a one-dimensional example, the total strain (ε_{tot}) can be related to the mechanical (ε_{mec}) and thermal (ε_{th}) strain with the following relation.

$$\varepsilon_{tot} = \varepsilon_{th} + \varepsilon_{mec} \tag{1.57}$$

Being the structure free to expand, no mechanical strain arise after heating, and total strain equals the thermal term, that can be expressed as:

$$\varepsilon_{tot} = \frac{\Delta l}{l} = \alpha \Delta T = \varepsilon_{th} \tag{1.58}$$

Free expansion obviously represents the most favorable condition dealing with thermal stress problems, because no stress arise. In practical situations, however, the component is partially or totally constrained (high dilatations could be unacceptable if tolerances are limited) and thermal strain can be converted into mechanical strain. The following examples are proposed to clarify these concepts.

1.2.2 Conversion of Thermal to Mechanical Strain

To investigate how the thermal strain can be converted into mechanical strain a simple problem is here discussed. The bar restrained at its ends of Figure 1.11 is here considered. No displacements are allowed in x-direction, and its length must remain constant. Maintaining this constraint, the bar is gradually heated from the reference temperature, T_0, at which the material does not show thermal expansion. The final condition is represented by the temperature T_1, being $\Delta T = T_1 - T_0$. Also in this example Equation (1.57) remains valid. As previously stated , the thermal strain is not responsible of any damage into the material, while its conversion into mechanical strain could lead to static or fatigue failure. During the heating process, a tensile stress develops in the bar because of the constraint. Since the total strain (ε_{tot}) must be zero, from Equation (1.57) the mechanical strain equals (in absolute value) the thermal expansion:

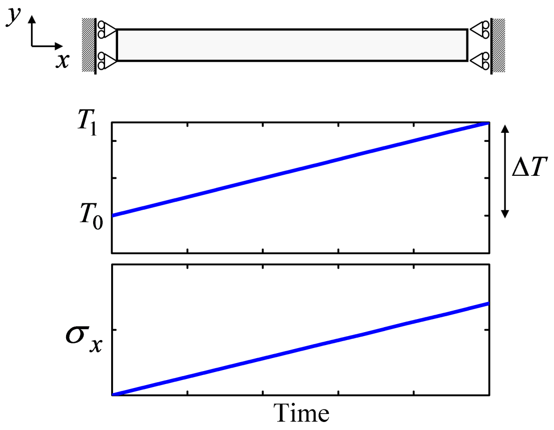

Figure 1.11: Complete conversion of thermal to mechanical strain.

$$\varepsilon_{mec} = -\varepsilon_{th} = -\alpha \Delta T \tag{1.59}$$

where α is the coefficient of thermal expansion. A complete conversion from thermal to mechanical strain is then reached, and the related stress can be calculated as:

$$\sigma_x = E\varepsilon_{mec} = -\alpha E \Delta T \tag{1.60}$$

where σ_x represents the stress in x-direction, and E the Young's modulus of the material.

1.2.3 Partial Constraint

Thermal strain is not always completely conversed in mechanical strain. In practical applications, in fact, the thermal expansion is not completely constrained. The following example, whose original idea is proposed in [9] and here it is developed, can be adopted to clarify this concept. Let consider a two-bar assembly in which the ends of the bars are attached to two rigid plates respectively and no rotations are allowed, see Figure 1.12. The two plates have area A_1 and A_2, respectively, while their elastic moduli are E_1 and E_2, respectively. One end of the plates is fixed, the other is capable of displacements only along y-direction. Bar 2 is heated, and for this reason it tends to expand. Its expansion, however, is partially restrained by bar 1 through attachments, that are rigid enough so that the net lengths of bar 1 and 2 are always equal. Considering that the bars have the same initial length, and recalling Equation (1.57) it is possible to write:

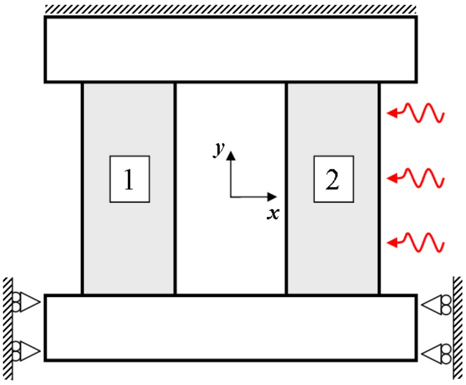

Figure 1.12: Two-bar assembly in which only one bar is heated.

$$\varepsilon_{mec,1} = \varepsilon_{mec,2} + \varepsilon_{th,2} \tag{1.61}$$

since $\varepsilon_{th,1}$ is zero, due to the fact that only bar 2 is heated. The equilibrium of forces implies that:

$$\sigma_1 A_1 = -\sigma_2 A_2 \tag{1.62}$$

Considering a linear elastic behavior of the material, the stress is related to the mechanical strain with the Hooke's law, as described in Equation (1.60). Combining Equation (1.61) and (1.62) the axial stress in the bar 2 can be finally related to the axial stiffness ratio:

$$\sigma_2 = \frac{-\alpha \Delta T E_2}{1 + \left(\frac{E_2 A_2}{E_1 A_1}\right)} \tag{1.63}$$

And the axial stress for the bar 1 is:

$$\sigma_1 = \frac{\alpha \Delta T E_1}{1 + \left(\frac{E_1 A_1}{E_2 A_2}\right)} \tag{1.64}$$

Assuming the bars constituted by the same material (i.e. $E_1 = E_2$), it is evident from Equations (1.62, 1.63) that the stress is directly related to the bar's areas ratio. As an example, if A_1/A_2 increases σ_2 reaches higher compressive values (while bar 1 is characterized by lower values of tensile stress). Figure 1.13 show the stress variation against the areas ratio. The two asymptotic conditions are reached when $A_1 = 0$ and $A_1 = \infty$. In the first condition bar 2 is free to expand (hence $\sigma_2 = 0$), while the second represents the complete constraint discussed in the previous paragraph, where the thermal strain is completely conversed in mechanical strain, and for this reason σ_2 reaches its maximum value and $\sigma_1 = 0$.

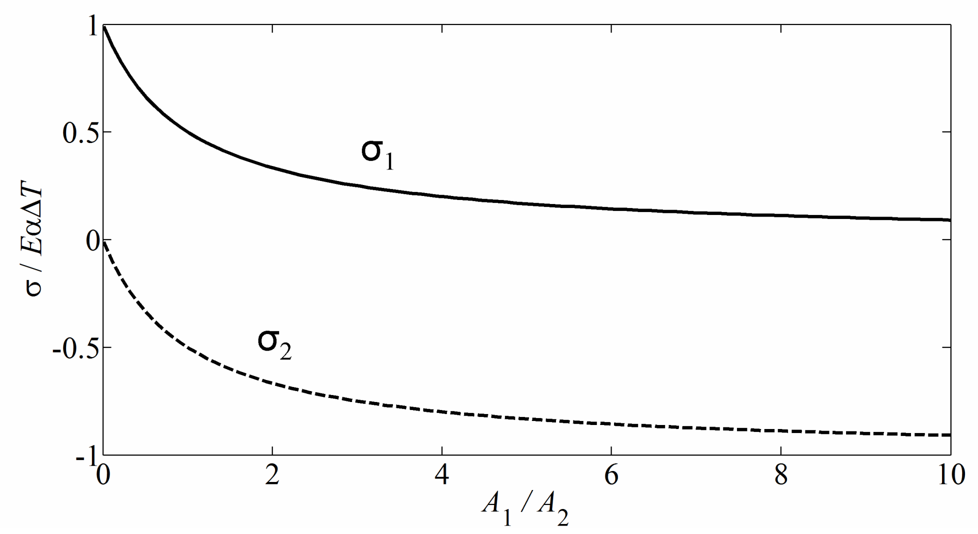

Figure 1.13: Stress trends in two-bar assembly related to areas ratio.

1.2.4 Simple Three- and Two-Dimensional Problems

Many engineering applications involve thermal stresses in three and two dimensions. Some simple problems, representative of situations that can be encountered in many industrial problems, are depicted in Figure 1.14. Figure 1.14a represents a limited volume of hot material, heated an amount of ΔT from the reference temperature, surrounded by a volume of cold material. The thermal expansion of the heated region is completely restrained by the presence of cold surroundings ($\varepsilon_x = \varepsilon_y = \varepsilon_z = 0$), and an hydrostatic stress state develops.

$$\sigma_x = \sigma_y = \sigma_z = -\frac{\alpha E \Delta T}{1 - 2\nu} \tag{1.65}$$

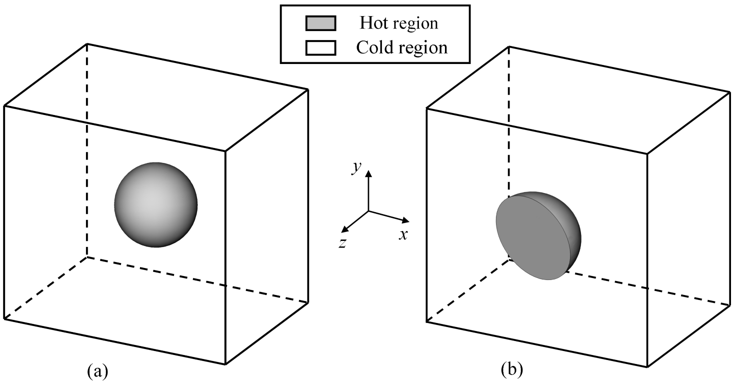

Figure 1.14: (a) Confined hot region into a cold volume. (b) Confined hot area.

In Figure 1.14b a restricted area located on the surface is heated, while the surrounding material is maintained at room temperature. For this particular condition, $\sigma_z = 0$ (no stresses develop in z-direction), while $\varepsilon_x = \varepsilon_y = 0$, because the small heated part would freely expand but it is "laterally" constrained by the surrounding large cold portion. A plane hydrostatic stress state then occurs.

$$\sigma_x = \sigma_y = -\frac{\alpha E \Delta T}{1 - \nu} \tag{1.66}$$

This situation is representative of many practical situations, where only some regions of a mechanical component are heated, while the remaining part is maintained at room temperature. As an example, this simplified model permits to explain the mechanical behavior of a copper mold. As it will be explained in Chapter 3, during continuous casting, molten steel heats the inner surface of the mold, while the external part is maintained at constant temperature with cooling water. The resultant stress status is consistent with the model proposed in Figure 1.14b.

1.2.5 Problem Solving Technique

The equation for thermal stresses can be derived in exactly the same manner as those for the general elasticity problem. In fact, *equilibrium equation*, which establish that each element in the body is equilibrium under the action of the forces imposed on it, and *compatibility equations*, which state the physical fact that strains cannot vary in a random manner, remain unchanged. That is due to the fact that the first set of equations is concerned not with how these stresses arise but rather with relations that must exist among the stresses that are present, while the second set is not concerned with the cause for the displacements but rather with the relation that must exist among them if they are present [9]. Such equations can be found in standard texts on elasticity, as [11]. The only ones in the thermal-stress problem which differ from those in the general elasticity problem are *stress-strain relations*: in fact, strains due to thermal expansions must be included in problems involving temperature changes. The general formulation of the total strains in rectangular coordinates is:

$$\begin{cases} \varepsilon_{tot,x} = \dfrac{1}{E}[\sigma_x - \nu(\sigma_y + \sigma_z)] + \alpha\Delta T \\ \varepsilon_{tot,y} = \dfrac{1}{E}[\sigma_y - \nu(\sigma_x + \sigma_z)] + \alpha\Delta T \\ \varepsilon_{tot,z} = \dfrac{1}{E}[\sigma_z - \nu(\sigma_x + \sigma_y)] + \alpha\Delta T \end{cases} \tag{1.67}$$

where $\alpha\Delta T$ is the thermal expansion that would be present if the element were permitted to expand freely as the temperature is raised an amount ΔT above the reference condition of uniform temperature (at which no stresses are present). It has to be noticed that Equation (1.57), as well as (1.59), can directly be obtained from the system of Equations (1.67) considering a one-dimensional problem and neglecting σ_y and σ_z. Also Equation (1.65) and (1.66) can be directly achieved from the system of Equations (1.67), considering the related simplifications.

A well-established strategy to be used when treating thermal stresses in more general situation is briefly described in the following. A one-dimensional problem, in which a body is subjected to a temperature distribution $T(x)$ is adopted. The difference between this temperature and the reference temperature (T_0) is responsible for the rise of thermal stress.

$$\Delta T = (T(x) - T_0) \tag{1.68}$$

The problem is sketched in Figure 1.15, in which a mechanical component is assumed to be heated. The starting point of the strategy, named as *Duhamel's analogy*, is to consider the body to be divided into a series of slits by cuts along the entire length [9]. Each fiber is considered to be at uniform temperature; hence it will expand freely in the axial direction an amount of $\alpha\Delta T$. If a compressive stress $\sigma^* = -E\alpha\Delta T$ is applied, each of the slits will be brought back to its initial dimension. Since the body now has its original dimensions, it can be imagined as re-connected along the initial cuts, so the present system is different from the original one only because of the presence of an edge stress. A tensile stress σ^{**} need to be applied along the edge in order to make it exactly the same. In the re-jointed body, however, the elemental slits are not free to strain independently, but they must

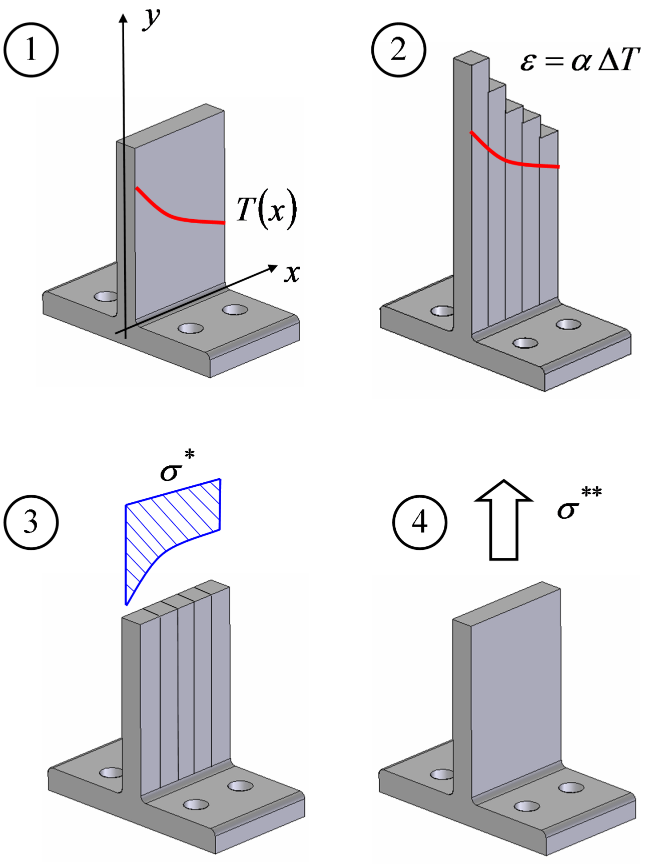

Figure 1.15: Steps to follow in solving problems involving thermal stresses.

strain as a continuous elastic system. Furthermore, the stress distribution due to the external-force system must be obtained according to elastic theory. If the body's length is significantly greater than its other dimensions, the stresses σ^{**} remote from the edge may be determined applying St. Venant's principle, by replacing the external stress system with its static equivalent (its resultant force and moment). The stress on the component can be finally evaluated adding together σ^{*} and σ^{**}. A more detailed discussion, also for three-dimensional geometries, can be found in [9]. In the following this approach will be applied to obtain closed form solutions of some examples of thermal stresses problems.

1.2.6 Closed Form Solutions

In this section some analytical expression of thermal stresses are proposed. Closed-form solutions can be achieved for particular geometries, in which the aforementioned strategy allows to obtain the stress pattern starting from the temperature field. Temperature distribution can be evaluated referring to the techniques previously described.

In particular two simple geometries will be considered: a plate and an hollow cylinder. The analytical evaluation of stress field caused by temperature distributions allows to assess some general rules: it will be proved, in fact, that a linear temperature variation in a *rectangular* coordinate system can not give rise to thermal stresses in absence of external restrains. On the other hand, even in absence of mechanical restraints, in a *cylindrical* coordinate system a linear temperature gradient give rise to thermal stresses.

The sets of equations obtained for the plate and the hollow cylinder are also used as starting point to develop interpretative models of the behavior of more complex industry applications proposed in chapter 3 and 4. These models, based on simplified geometries that can be analytically solved, are adopted in order to gain insights into the physic of the problem and to quickly assess the relevant parameters. As an example, as it will explained Chapter 3, the stress field along the thickness of a copper mold can be analytically evaluated employing a simplified model of an hollow cylinder in which a significant part of the external portion is maintained at constant temperature.

Thermal stresses in plates

As a first example, a rectangular plate of uniform thickness ($2L$), in which the temperature is a function of x, is considered. The problem is sketched in Figure 1.16. As previously pointed out, the difference between this temperature ($T(x)$) and the reference temperature (T_0), at which no

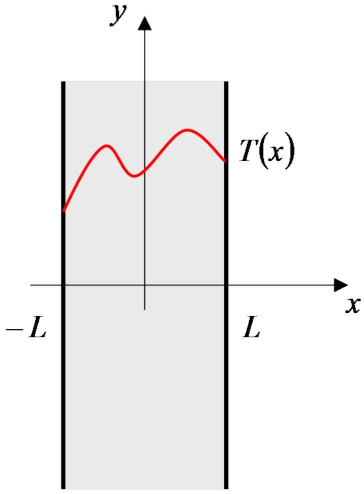

Figure 1.16: Scheme of thermal stresses problem in a plate.

stresses are present, is responsible for the rise of thermal stress. If considered separately one from the other, each fiber will expand freely in the axial direction an amount of $\alpha \Delta T$. This thermal expansion can be suppressed by applying to each element of the plate the longitudinal compressive stress.

$$\sigma_y{}^{*} = -\alpha E \Delta T \tag{1.69}$$

The plate is free from external forces, because it is free to expand, so it is necessary to superpose on the stress of Equation (1.69) the stresses produced in the plate by tensile forces distributed at the ends. At a sufficient distance from the ends these forces produce a approximately uniformly distributed tensile stress of magnitude:

$$\sigma_y{}^{**} = \frac{1}{2L} \int_{-L}^{L} \alpha E \Delta T \, \mathrm{d}x \tag{1.70}$$

If the temperature distribution is not symmetric with respect to x-axis, also bending stresses need to be taken into account. This further contribution can be determined from the condition that the moment of the forces distributed over a cross section must be zero, thus obtaining:

$$\sigma_y{}^{***} = \frac{3}{2L^3} x \int_{-L}^{L} \alpha E \Delta T \, \mathrm{d}x \tag{1.71}$$

The total stress σ_y can be finally evaluated adding together $\sigma_y{}^{*}$, $\sigma_y{}^{**}$, $\sigma_y{}^{***}$ and the final expression of thermal stresses in the plate with free ends at a considerable distance from the ends is then:

$$\sigma_y = -\alpha E \Delta T + \frac{1}{2L} \int_{-L}^{L} \alpha E \Delta T \, \mathrm{d}x + \frac{3}{2L^3} x \int_{-L}^{L} \alpha E \Delta T \, \mathrm{d}x \tag{1.72}$$

Equation (1.72) allows to calculate thermal stresses in plates for any given temperature distribution (and hence ΔT). As an example, it is possible to evaluate the thermal stresses during the heating of the plate previously described. In that case, starting from the reference temperature (T_0), the surfaces of the plate ($x = \pm L$) were assumed to be suddenly heated at two different temperatures ($T_1 = 2T_2 = 10T_0$). The temperature field that develops during the transient phase, described by Equation (1.39), can be adopted in combination with Equation (1.72) in order to obtain the thermal stresses distribution. If a steady-state heat flows develops, a linear temperature variation develops along x-direction, as already depicted in Figure 1.7. By substituting

$$\Delta T = \frac{T_2 - T_1}{2L} x + \frac{T_2 + T_1}{2} - T_0 \tag{1.73}$$

in Equation (1.72), it is possible to obtain the resultant stress distribution of the plate, $\sigma_y = 0$. This result has a general validity: in absence of mechanical restraints, in a *rectangular* coordinate system a linear temperature gradient is not responsible of thermal stresses. If, instead, the plate is restrained at its ends, thermal expansion is not allowed and a compressive stress given by Equation (1.69) arise.

Thermal stresses in a hollow cylinder

The proposed strategy can be adopted to solve also problems in non-rectangular coordinate systems. An hollow cylinder is here considered, in which the inner surface is considered heated by a heat flow, while a convective cooling is applied on the external surface. The thermal problem has been previously treated to evaluate the temperature distribution in steady-state condition. That temperature field will be used as input to establish the stress at any radial coordinate. The followed strategy, described in [11] is valid in the case with ends free to expand. A solution for restrained ends is also proposed. As it will be shown, an imposed linear temperature field in this case causes the development of stresses even if the cylinder is free to expand. In a cylindrical coordinate system the stress-strain relations in

Equation (1.67) become:

$$\begin{cases} \varepsilon_r = \dfrac{1}{E}[\sigma_r - \nu(\sigma_\vartheta + \sigma_z)] + \alpha\Delta T \\ \varepsilon_\vartheta = \dfrac{1}{E}[\sigma_\vartheta - \nu(\sigma_r + \sigma_z)] + \alpha\Delta T \\ \varepsilon_z = \dfrac{1}{E}[\sigma_z - \nu(\sigma_r + \sigma_\vartheta)] + \alpha\Delta T \end{cases} \tag{1.74}$$

where ε_r, ε_ϑ and ε_z are the *total* strains for radial, hoop and axial direction respectively. As previously illustrated in the general procedure, the axial displacement induced by thermal expansion is assumed to be completely restrained. Since $\varepsilon_z = 0$, the last of Equation (1.74) becomes:

$$\sigma_z^* = \nu(\sigma_r + \sigma_\vartheta) - \alpha\Delta T \tag{1.75}$$

then substituting Equation (1.75) in Equation (1.74), it is possible to obtain:

$$\begin{cases} \varepsilon_\vartheta = \dfrac{1-\nu^2}{E}\left(\sigma_\vartheta - \dfrac{\nu}{1-\nu}\sigma_r\right) - (1+\nu)\alpha\Delta T \\ \varepsilon_r = \dfrac{1-\nu^2}{E}\left(\sigma_r - \dfrac{\nu}{1-\nu}\sigma_\vartheta\right) - (1+\nu)\alpha\Delta T \end{cases} \tag{1.76}$$

Solving Equation (1.76) for σ_r and σ_ϑ allow to write:

$$\begin{cases} \sigma_r = \dfrac{\nu E}{(1+\nu)(1-2\nu)}\left(\dfrac{1-\nu}{\nu}\varepsilon_r + \varepsilon_\vartheta - \dfrac{1+\nu}{\nu}\alpha\Delta T\right) \\ \sigma_\vartheta = \dfrac{\nu E}{(1+\nu)(1-2\nu)}\left(\dfrac{1-\nu}{\nu}\varepsilon_\vartheta + \varepsilon_r - \dfrac{1+\nu}{\nu}\alpha\Delta T\right) \end{cases} \tag{1.77}$$

Recalling that the *equilibrium equations* in polar coordinates with no body forces can be written as:

$$\frac{\mathrm{d}\sigma_r}{\mathrm{d}r} + \frac{\sigma_r - \sigma_\vartheta}{r} = 0 \tag{1.78}$$

equation (1.77) leads to

$$\frac{r\nu}{(1+\nu)(1-2\nu)}\frac{\mathrm{d}}{\mathrm{d}r}\left(\frac{1-\nu}{\nu}\varepsilon_r + \varepsilon_\vartheta\right) + \frac{\varepsilon_r - \varepsilon_\vartheta}{\nu(1+\nu)} = \frac{\alpha r}{1-2\nu}\frac{\mathrm{d}\Delta T}{\mathrm{d}r} \tag{1.79}$$

If u indicates the radial displacement, *compatibility equations* are:

$$\begin{cases} \varepsilon_r = \dfrac{\mathrm{d}u}{\mathrm{d}r} \\ \varepsilon_\vartheta = \dfrac{u}{r} \end{cases} \tag{1.80}$$

These equations can be substituted in Equation (1.79):

$$\frac{\mathrm{d}^2 u}{\mathrm{d}r^2} + \frac{1}{r}\frac{\mathrm{d}u}{\mathrm{d}r} - \frac{u}{r^2} = (1+\nu)\alpha\frac{\mathrm{d}\Delta T}{\mathrm{d}r} \tag{1.81}$$

Equation (1.81) can be integrated, obtaining a general expression for u with two constants (C_1 and C_2) to be determined. The stress components can be found using this solution in Equation (1.80) and substituting the results in Equations (1.77, 1.75). However, it has to be taken into account that if no mechanical constraints are present, the resultant force on the free ends will be zero. For this reason, a uniform axial stress (σ^{**}) need to be superimposed, accordingly to the general procedure. This axial stress affects also radial displacements, by an amount of $-\nu\sigma^{**}/E$. The general expression for u, σ_r,σ_ϑ, σ_z are then:

$$\begin{cases} u = \dfrac{1+\nu}{1-\nu}\alpha\dfrac{1}{r}\displaystyle\int_{r_i}^{r}\Delta T r\,\mathrm{d}r + C_1 r + \dfrac{C_2}{r} - \dfrac{\nu\sigma^{**}}{E} \\ \sigma_r = -\dfrac{\alpha E}{1-\nu}\dfrac{1}{r^2}\displaystyle\int_{r_i}^{r}\Delta T r\,\mathrm{d}r + \dfrac{E}{1+\nu}\left(\dfrac{C_1}{1-2\nu} - \dfrac{C_2}{r^2}\right) \\ \sigma_\vartheta = \dfrac{\alpha E}{1-\nu}\dfrac{1}{r^2}\displaystyle\int_{r_i}^{r}\Delta T r\,\mathrm{d}r - \dfrac{\alpha E\Delta T}{1-\nu} + \dfrac{E}{1+\nu}\left(\dfrac{C_1}{1-2\nu} + \dfrac{C_2}{r^2}\right) \\ \sigma_z = \sigma^* + \sigma^{**} = -\dfrac{\alpha E\Delta T}{1-\nu} + \dfrac{2\nu E C_1}{(1+\nu)(1-2\nu)} + \sigma^{**} \end{cases} \tag{1.82}$$

The constants C_1 and C_2 can be determined from the condition that the inner and the outer surface must be free from radial stresses, hence $\sigma_r(r_i) = 0$ and $\sigma_r(r_e) = 0$.

$$\begin{cases} C_1 = \dfrac{\alpha E}{r_e^2 - r_i^2}\dfrac{(1+\nu)(1-2\nu)}{1-\nu}\displaystyle\int_{r_i}^{r_e}\Delta T r\,\mathrm{d}r \\ C_2 = \dfrac{\alpha E r_i^2}{r_e^2 - r_i^2}\dfrac{1+\nu}{1-\nu}\displaystyle\int_{r_i}^{r_e}\Delta T r\,\mathrm{d}r \end{cases} \tag{1.83}$$

Considering that the resultant of the uniform axial stress σ^{**} must be equal to the resultant of axial stress σ_z^* it is possible to write:

$$\sigma^{**}\pi(r_e^2 - r_i^2) = \int_{r_i}^{r_e} 2\pi r\sigma_z^*\,\mathrm{d}r \tag{1.84}$$

Substituting the last of Equations (1.82) in this relation the value of σ^{**} can be determined as:

$$\sigma^{**} = \frac{2\alpha E}{r_e^2 - r_i^2}\int_{r_i}^{r_e}\Delta T r\,\mathrm{d}r \tag{1.85}$$

The final expressions for u, σ_r,σ_ϑ, σ_z are then:

$$\begin{cases} u = \dfrac{1+\nu}{1-\nu}\alpha\dfrac{1}{r}\displaystyle\int_{r_i}^{r}\Delta T r\,\mathrm{d}r + \dfrac{\alpha}{r_e^2-r_i^2}\dfrac{r^2(1-r\nu)+r_i^2(1+\nu)}{r(1-\nu)}\displaystyle\int_{r_i}^{r_e}\Delta T r\,\mathrm{d}r \\ \sigma_r = \dfrac{\alpha E}{1-\nu}\dfrac{1}{r^2}\left[\dfrac{r^2-r_i^2}{r_e^2-r_i^2}\displaystyle\int_{r_i}^{r_e}\Delta T r\,\mathrm{d}r - \displaystyle\int_{r_i}^{r}\Delta T r\,\mathrm{d}r\right] \\ \sigma_\vartheta = \dfrac{\alpha E}{1-\nu}\dfrac{1}{r^2}\left[\dfrac{r^2+r_i^2}{r_e^2-r_i^2}\displaystyle\int_{r_i}^{r_e}\Delta T r\,\mathrm{d}r + \displaystyle\int_{r_i}^{r}\Delta T r\,\mathrm{d}r - \Delta T r^2\right] \\ \sigma_z = \dfrac{\alpha E}{1-\nu}\left[\dfrac{2}{r_e^2-r_i^2}\displaystyle\int_{r_i}^{r_e}\Delta T r\,\mathrm{d}r - \Delta T\right] \end{cases} \tag{1.86}$$

The temperature field previously evaluated can be now used to explicitly calculate the stress distribution in radial direction. If the inner surface is heated by a heat flux and a convective cooling is applied on the external surface, the non-linear temperature distribution of Equation (1.55) arise in steady-state conditions. Considering T_0 as the reference temperature, for which no stresses are present, it is possible to calculate the effective temperature range.

$$\Delta T(r) = \frac{T_i - T_e}{\log\frac{r_i}{r_e}}\log\frac{r}{r_e} + T_e - T_0 \tag{1.87}$$

Equations (1.86) can be then analytically solved, obtaining the following set of expressions:

$$\begin{cases} \sigma_r = \dfrac{\alpha E(T_i-T_e)}{2(1-\nu)\log\frac{r_e}{r_i}}\left[-\log\dfrac{r_e}{r} - \dfrac{r_i^2}{r_e^2-r_i^2}\left(1-\dfrac{r_e^2}{r^2}\right)\log\dfrac{r_e}{r_i}\right] \\ \sigma_\vartheta = \dfrac{\alpha E(T_i-T_e)}{2(1-\nu)\log\frac{r_e}{r_i}}\left[1-\log\dfrac{r_e}{r} - \dfrac{r_i^2}{r_e^2-r_i^2}\left(1+\dfrac{r_e^2}{r^2}\right)\log\dfrac{r_e}{r_i}\right] \\ \sigma_z = \dfrac{\alpha E(T_i-T_e)}{2(1-\nu)\log\frac{r_e}{r_i}}\left[1-2\log\dfrac{r_e}{r} - \dfrac{2r_i^2}{r_e^2-r_i^2}\log\dfrac{r_e}{r_i}\right] \end{cases} \tag{1.88}$$

This set of equation is valid if the ends of the cylinder are free to expand, and the stress field is represented in Figure 1.17 for an hollow cylinder ($r_e = 2r_i$ is considered) heated in the inner part by a thermal flux and cooled in the outer surface. The temperature field previously evaluated is also plotted for clarity. As can be seen, the inner portion is characterized by compressive values of hoop and axial stresses, while a tensile stress condition develops in the cold region. Radial stress assumes negligible values in the domain. If the ends are not free to expand, the expressions for σ_r and σ_ϑ remain valid, while σ_z need to be modified because there is no necessity of superimpose

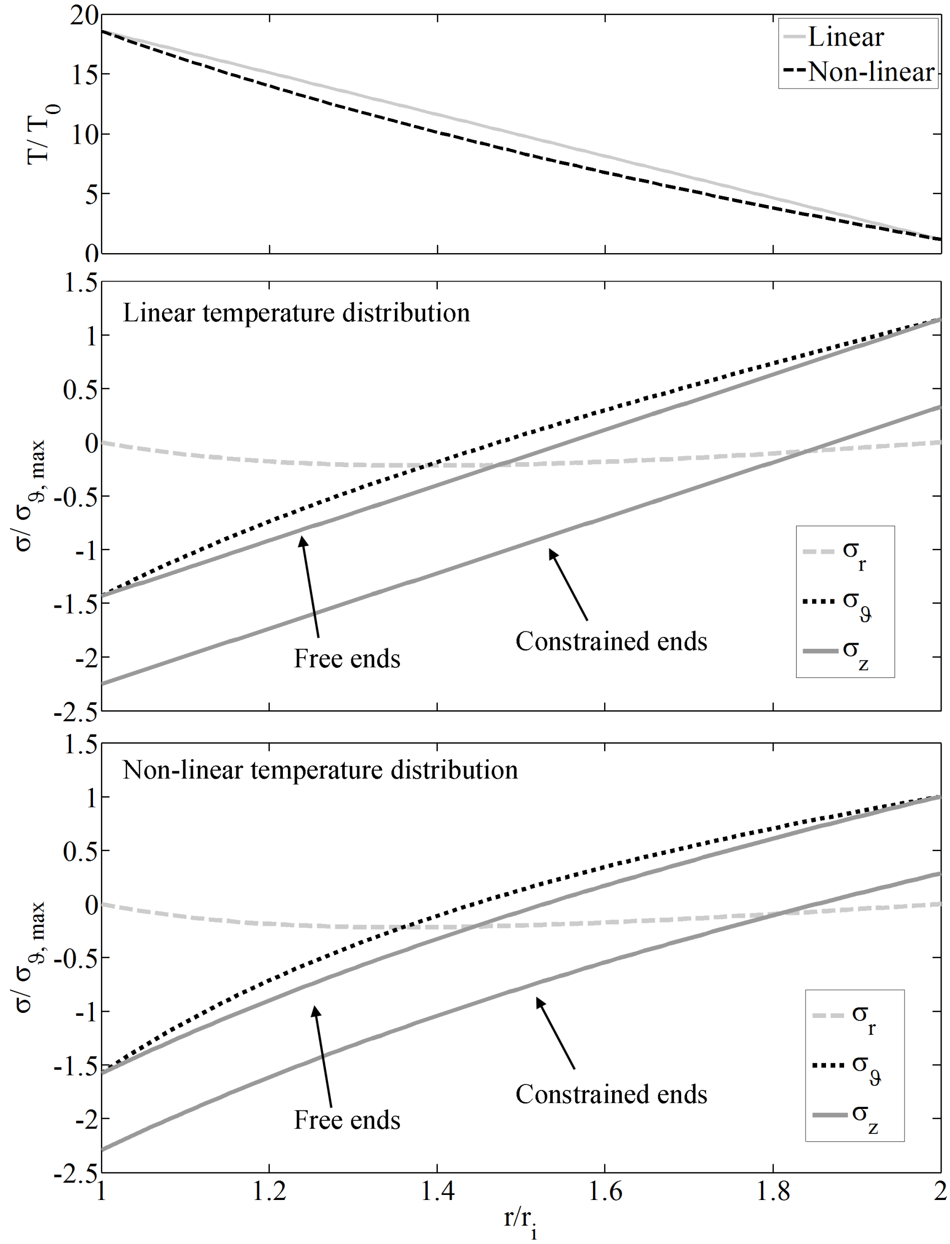

Figure 1.17: Thermal stresses in an hollow cylinder for different constraints and temperature distributions.

the axial stress σ^{**} in the fourth of Equation (1.82). The analytic expression of axial stress in this case becomes:

$$\sigma_z = \frac{\alpha E}{1-\nu}\left[\frac{2\nu}{r_e^2 - r_i^2}\int_{r_i}^{r_e}\Delta T r\,\mathrm{d}r - \Delta T\right] \tag{1.89}$$

and substituting the temperature field of Equation (1.87) the final expression is:

$$\begin{aligned}\sigma_z =& \frac{\alpha E}{(1-\nu)}\Bigg\{\frac{T_i - T_e}{\log\frac{r_e}{r_i}}\left[\frac{2\nu}{r_e^2 - r_i^2}\left(-\frac{r_e^2}{4} + \frac{r_i^2}{4} + \frac{r_i^2}{2}(\log r_e - \log r_i)\right) - \log\frac{r}{r_e}\right]\\ &+ (\nu - 1)(T_e - T_0)\Bigg\}\end{aligned} \tag{1.90}$$

As it can be seen in Figure 1.17, due to the fact that the free expansion of the fibers is not allowed, the constrain of the ends give rise to a higher compressive strain in axial direction. System of Equations (1.86) can be adopted to evaluate stresses for any given temperature distribution. As already pointed out, Equation (1.55) describe the temperature field that spontaneously arise in steady-state conditions if the inner surface is heated by a heat flux, while a convective cooling is applied on the external surface. Assuming that a *linear* temperature variation occurs in the hollow cylinder, it is possible to evaluate the related stress field simply by substituting in Equations (1.86) the appropriate temperature range $\Delta T_{lin}(r)$:

$$\Delta T_{lin}(r) = -\frac{T_i - T_e}{r_e - r_i}r + \frac{T_i r_e - T_e r_i}{r_e - r_i} - T_0 \tag{1.91}$$

As shown in Figure 1.17, the resulting stress distribution is very similar to that obtained from a non-linear temperature variation, and also this result has a more general validity: even in absence of mechanical restraints, in a *cylindrical* coordinate system a linear temperature gradient give rise to thermal stresses.

1.3 Numerical Methods and Temperature Effects on Metals

Problems involving simple geometries with simple boundary conditions can be solved analytically, as shown in previous paragraphs. Temperature distribution, as well as related stresses, can then be found with closed-form expressions which are defined at *every* point of the domain. But many problems encountered in engineering practice involve complicated geometries with complex boundary conditions and variable material properties, and cannot be analytically solved. Numerical methods allow to obtain sufficiently accurate approximate solutions when dealing with such problems. Basically, they are based on replacing the governing differential equation of the problem by a set of algebraic equations for the unknowns (temperature, displacements) at some selected points (nodes) of the domain. The simultaneous solution of these equations, leads to then to an answer valid at *discrete* points. Among all numerical methods available, the finite element method (FEM) is an efficient technique used in practice. In simple terms, it allows to divide a complex problem into small elements that can be solved in relation to each other.

The mathematical and theoretical framework of finite element technique is fully investigated in many standard handbooks, such as [12, 13], while this paragraph focuses on some practical hints and techniques to be adopted dealing with thermal stresses problems. All the numerical simulations are performed using ANSYS$^{®}$, a commercial software dedicated to finite element analysis. In the following, some examples of *parametric design language* (*APDL*) codes will also be given, to further help the reader to become familiar about the implementation of the model. Although commands are specific for the adopted one, similar procedures can be used also for different softwares.

Dealing with thermal stresses problems, two different analysis need to be performed: a thermal analysis, where heat loads give rise to the temperature field, and a structural one, in which stresses arising from the given temperature distribution are evaluated (with or without superimposition of mechanical loads). A careful evaluation of the entity of deformations could

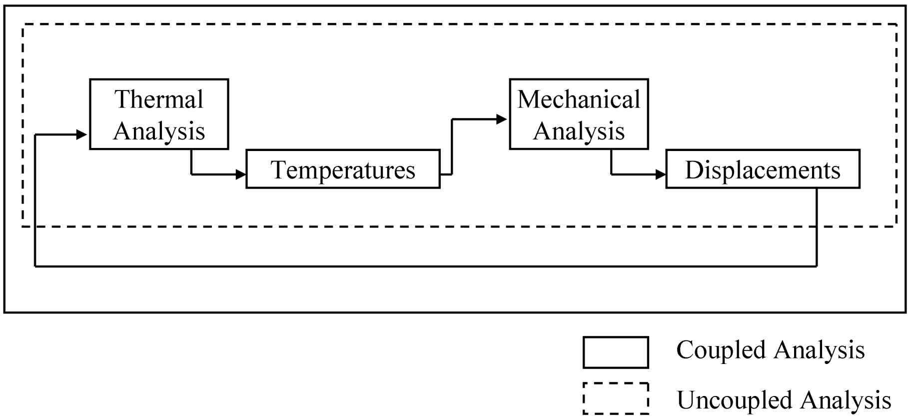

Figure 1.18: Coupled and uncoupled thermo-mechanical analysis.

lead to treat the two analysis as *uncoupled*: if the structural deformations do not alter the absorbed heating and temperature distributions, the thermal analysis can be firstly performed, and then the resulting temperature distribution can be adopted as input for a subsequent structural analysis. In ANSYS®it is possible to run an *uncoupled* analysis without re-modeling the structure, by simply switching from thermal elements to structural element:

```
!Commands for Thermal Analysis
...
ETCHG,TTS ! Switch Thermal To Structural
!Commands for Structural Analysis
...
```

This strategy permits to reduce computational time, without affecting results in a significant way. In a *coupled* analysis, in fact, the thermal solution need to be recalculated at each substep as the mechanical solution is partially updated. Figure 1.18 sketches these concepts.

Dealing with stresses arising from temperature distribution, the temperature effect on material properties should be taken into account. Thermal conductivity and specific heat of metals are greatly affected by temperature, as well as other mechanical properties such as tensile strength, yield strength, thermal expansion. As already pointed out, thermal conductivity in metals decreases with increasing temperature. The same behavior can be usually observed for tensile and yield strength (although tensile strength changes only a small amount until a certain temperature is reached, and then it falls off rapidly [14]). Specific heat exhibits a more complex response, with a peak around 750 °C, due to a phase change in the steel. A complete review of thermal and mechanical properties of steels and other materials related to temperature variation are available in [15, 16, 17]. Figure 1.19 shows the temperature variation of conductivity and specific heat, while Figure 1.20 represents the reduction factors to be applied at Young's modulus and yield stress measured at room temperature (E_{20}, $\sigma_{y,20}$) in order to evaluate the corresponding value at an higher temperature. In practice, the temperature effect on mechanical properties can be suitably modeled in commercial softwares by defining a table that includes the temperatures and the related mechanical properties. In ANSYS®the variation of thermal conductivity and specific heat for the steel proposed in Figure 1.19 can be implemented as:

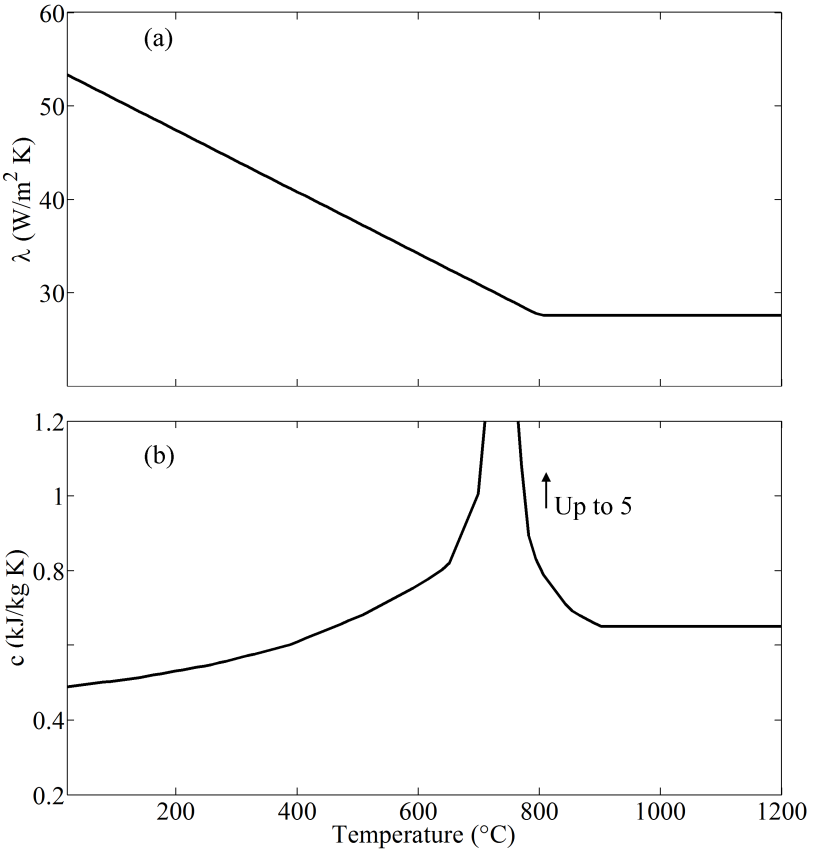

Figure 1.19: Variation of (a) thermal conductivity and (b) specific heat of steel against temperature.

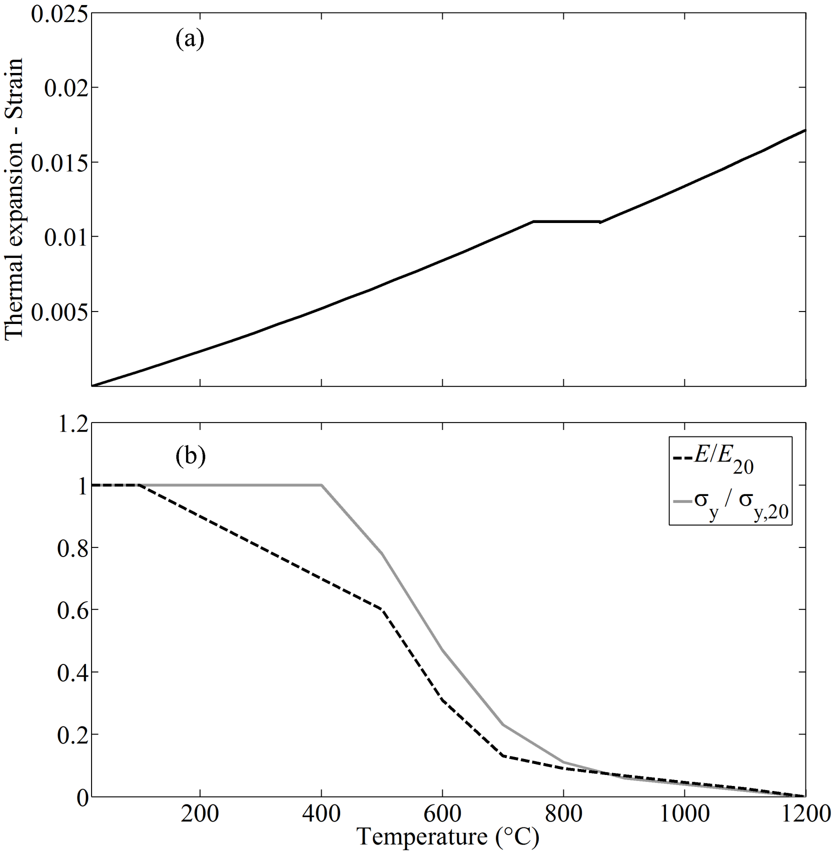

Figure 1.20: Variation against temperature of (a) thermal expansion and (b) reduction factors for Young's modulus and yield stress.

```
MPTEMP,,,,,,,,
MPTEMP,1, 20 , 135, 260, 385, 510, 600
MPTEMP,7, 650 , 700, 720, 730, 735, 740
MPTEMP,13, 750 , 780, 800, 850, 900, 1000

MPDATA,KXX,1,1, 53.34, 49.545 , 45.42 , 41.295, 37.17, 34.20
MPDATA,KXX,1,7, 32.55, 30.90, 30.24, 29.91, 29.745, 29.58
MPDATA,KXX,1,13, 29.25, 28.26, 27.60, 27.60, 27.60, 27.60

MPDATA,C,1,1, 489, 512, 548, 599, 682, 760
MPDATA,C,1,7, 813, 1008, 1388, 2291, 5000, 2525
MPDATA,C,1,13, 1483, 908, 803, 695, 650, 650
```

While the parametric reduction of elastic modulus depicted in Figure 1.20 can be implemented as:

```
E20=205000*1e6
MPTEMP,,,,,,,,
MPTEMP,1, 20, 200, 400, 600, 800, 1000
MPDATA,EX,1,1, E20, 0.9*E20, 0.7*E20, 0.21*E20, 0.09*E20, 0.045*E20
```

A noteworthy effect on metals subjected to constant loads for long periods of time at elevated temperatures need to be briefly discussed. The specimens are found to be permanently deformed during the tests, even though the actual stresses are less than the yield strength of the material obtained from short-time tests made at the same temperature. This continuous deformation under load is called *creep* [14]. One of the most useful tests to have been devised is the long-time creep test under constant load, where a standard cylindrical tension specimen is heated up to the temperature $T = (0.3 \div 0.5)T_m$ (T_m is the melting temperature of the material) and loaded by a tensile force. The value of the normal stress in the specimen is usually much less than the yield limit of the material. The instantaneous material response is therefore elastic. The load and the temperature are kept constant during the test and a typical material response is shown in Figure 1.21, where the rate of deformation is plotted against time. It is possible to observe three characteristic periods of time during which the creep rate with time is sequentially decreasing, remaining constant, and increasing [18, 19]. These are often called the periods of primary, secondary, and tertiary creep. The primary stage of creep, which begins immediately after application of the load, is usually very short in duration but the rate of creep is high. The amount of strain developed during the secondary creep period is large compared with that in the primary creep period. At this stage the creep curves are usually approximated by a straight line. The tertiary stage of creep follows the secondary period and is

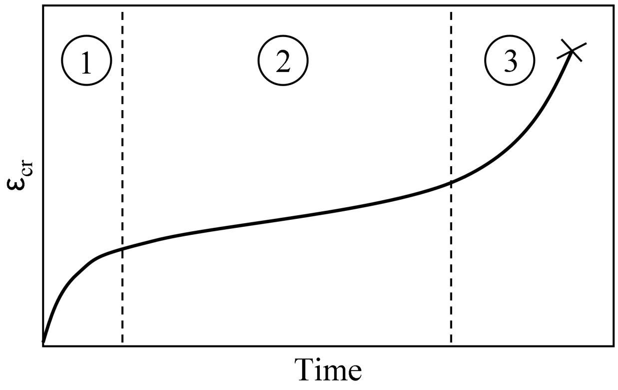

Figure 1.21: Strain vs. time curve under constant load and temperature. 1) primary creep, 2) secondary creep, 3) tertiary creep.

characterized by a rather rapid increase in the creep rate which eventually causes rupture in the material [20]. All of these stages of creep can be mathematically described by the constitutive equation of creep. The purpose of the constitutive equation is to provide a suitable means for calculating stresses and strains in a structure subjected to creep, where the intended lifetime of the structure is of particular importance. According to [21], the deformation depends on three main parameters: stress, time and temperature. Therefore the most general creep equation can be written as:

$$\varepsilon_{cr} = f(\sigma, t, T) \tag{1.92}$$

A mathematical dissertation of creep can be found in [22], while in [21] a review of fundamental laws is provided. An useful way of summarizing information about the range of dominance of each creep mechanisms, and the rates of flow they produce is given by Deformation-Mechanisms maps, provided in [23]. It was experimentally evidenced that the data fit reasonably well with various mathematical relations, depending on the material and test conditions, as mentioned in [24, 25]. This is the reason why creep parameters are usually available only for a well specified temperature or stress range, and it is difficult to perform prediction for creep behavior for temperatures or stresses away from this range. Due to the high non linear relations with stress or temperatures, the adoption of a non adequate set of creep parameters could lead to erroneous results, even of some orders of magnitude in terms of strains. Calculations involving creep should be then performed carefully. In Chapter 2 the effect of creep in the evaluation of fatigue-life relations will be discussed.

As a result of temperature variation, an important effect to consider is *phase transition.* Phase transition is the conversion of a thermodynamic system from one phase or state of matter to another. Three states of matter are known in everyday experience: *solid*, *liquid*, *gas*. *Melting* is the conversion of a solid to a liquid, *vaporization* is the transformation of a liquid to a gas, while the conversion of a solid directly to a gas without going through the liquid state is called *sublimation.* These processes are endothermic, since energy must be supplied to overcome the intermolecular forces that hold molecules together in the starting state.

The difference in enthalpy per mole of molecules between the liquid and solid states of a substance is called the enthalpy of fusion, ΔH_m. The enthalpy of vaporization, ΔH_v, and of sublimation, ΔH_s, can be defined in a similar way (obviously referring to different states of the matter). Some texts refer to ΔH_m as a heat of transformation, heat of fusion, or latent heat of fusion. The specific names for the phase transitions are shown in Figure 1.22.

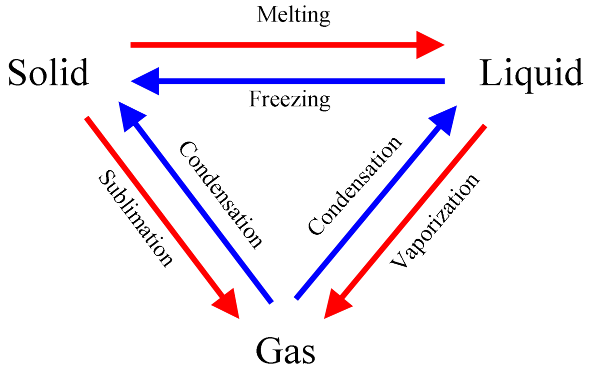

Figure 1.22: Phase changes from one state to another.

Melting, vaporization and sublimation are reversible and the enthalpy of the reverse phase change will have the same value but opposite sign. As already pointed out, the three phase changes described require energy input, while freezing and condensation release energy. During phase change, temperature of matters stay constant. Figure 1.23a shows the temperature variation against time when phase changes occur, while the enthalpy variation against temperature is plotted in Figure 1.23b. It is possible to notice that in intervals 1 (solid phase), 3 (liquid phase) and 5 (gas phase) the temperature of matter increases. The heat gained in these intervals can be expressed as:

$$Q = mc\Delta T \tag{1.93}$$

where; m is mass, c is specific heat capacity and ΔT is change in the temperature between the final and initial instant considered. In intervals 2

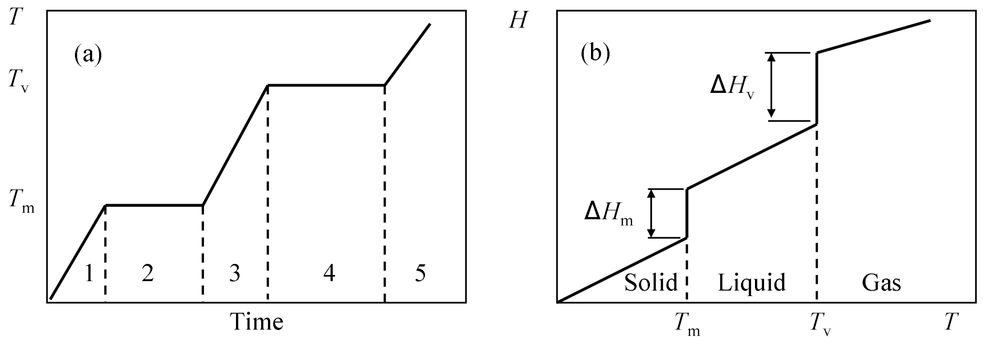

Figure 1.23: Temperature variation against time and enthalpy variation against temperature during phase changes.

and 4 temperature of matter stays constant because matter is changing phase. On the contrary, during phase change, distances between molecules increase, thus potential energy of matter also increases. In these intervals there is an heterogeneous mixture: as an example, in interval 2 there is the presence of both solid and liquid. Heat required in this interval can be expressed as:

$$Q = m\Delta H_m \tag{1.94}$$

As pointed out for creep, also phase changes are time dependent phenomena. Problems involving phase changes, as well as creep, require then transient analysis, in which the time needed for the conversion into the new phase of matter (or for the fulfillment of a new state of stress after creep-relaxation) has to be considered. This, in turn, lead to more sophisticated analysis with complex mathematical techniques, that usually induces a huge amount of time in performing numerical analysis.

As will be clarified in Chapter 3, an industrial oriented approach should adopt simplified strategies in order to obtain reliable solutions avoiding onerous (in terms of calculation time) models.

A simplified, but accurate procedure is here developed to deal with melting adopting a numerical model. This situation is representative of a practical case study described in Chapter (3), where the thermo-mechanical analysis of an anode adopted in electric arc furnaces is performed. The problem, sketched in Figure 1.24, involves a cylindrical steel bar heated by means of a thermal flux on the upper part, and cooled into the lower part, where a convective condition is present. The usual approach [26, 27] to simulate a phase change is to consider a thermal analysis with a linear enthalpy variation for both solid and liquid phases.

Taking advantage of axial symmetry, a two-dimensional model is adequate to describe the problem. Material properties considered for the problem

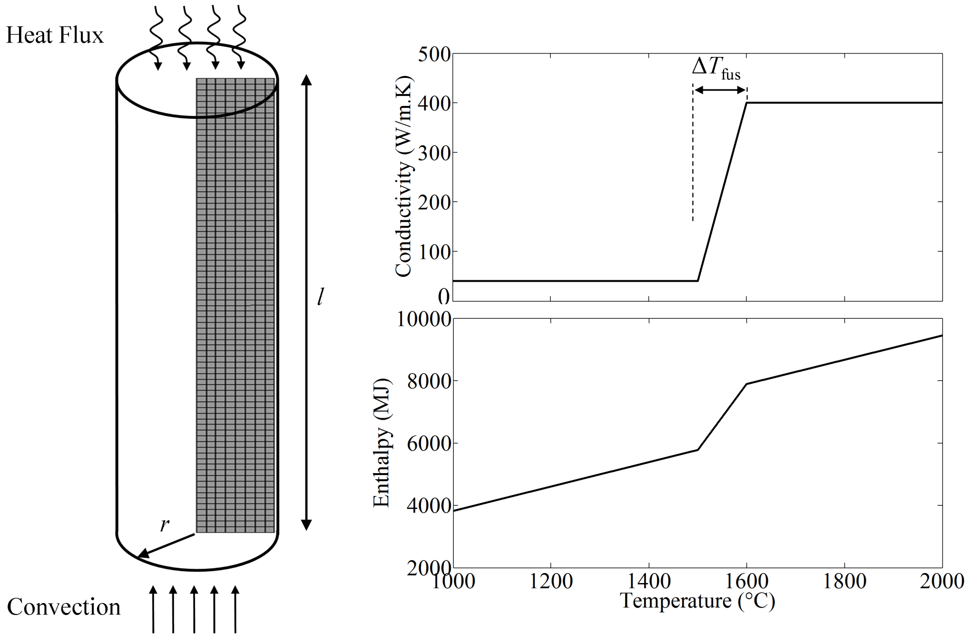

Figure 1.24: Simple problem involving phase change.

are collected in Table (1.1), where two different values of conductivity are considered: λ_{sol} for solid material and λ_{liq} for molten material. As well as thermal expansion, elastic modulus is considered to vary against temperature with reduction factors, as proposed in Figure 1.20, starting from a value at room temperature of $E_{20} = 205$ GPa.

The enthalpy variation between two temperatures, $T_{i,j}$, can be computed as:

$$H = \rho c \int_{T_i}^{T_j} \mathrm{d}T \tag{1.95}$$

During melting a transition range (ΔT_{fus}) need to be considered, to avoid convergence problems. In this region the slope of enthalpy curve can be calculated as $\rho \Delta H_m / \Delta T_{fus}$.

In ANSYS®the instructions for implement the variation of enthalpy proposed in Figure 1.24 are:

Table 1.1: Parameters adopted in simulations.

Parameter	**Value**
l, m	1
r, m	0.1
λ_{sol}, W/(mK)	40
λ_{liq}, W/(mK)	400
c, J/(kgK)	500
ΔH_m, J/(kg)	272000
ρ, kg/m^3	7800
T_m, °C	1500
ΔT_{fus}	100
$\dot{q}$, W/m^2	100000
T_b, °C	20

```
Tb = 20
deltat=100
Tm = 1500
rho= 7800
Cp= 500
CL= 272000

y1=rho*Cp*0
y2=rho*Cp*(Tm-Tb)
y3=rho*CL+y2
y4=rho*Cp*(Tm)+y3

MPTEMP,,,,,,,,
MPTEMP, 1, 20, Tm, Tm+deltat, Tm+deltat+Tm
MPDATA,ENTH, 1, 1, y1, y2, y3, y4
MPPLOT,ENTH,1,
```

A transient thermal analysis is required to achieve the temperature distribution along the bar. As it can be seen in Figure 1.25, at the beginning of the analysis the temperature of the upper portion of the bar constantly increases. After that period, the temperature stabilizes around the melting temperature, T_m, because the thermal flux is high enough to cause melting of the upper portion of the bar. Temperatures on the lower part require greater time to stabilize.

A subsequent structural analysis, where the cylindrical bar is considered simply supported on the lower part, can be used to evaluate displacements and stress field. As depicted in Figure 1.26 the lower, cold portion exhibits the highest values of Von Mises stress.

As previously mentioned, at melting point the enthalpy shows a sharp

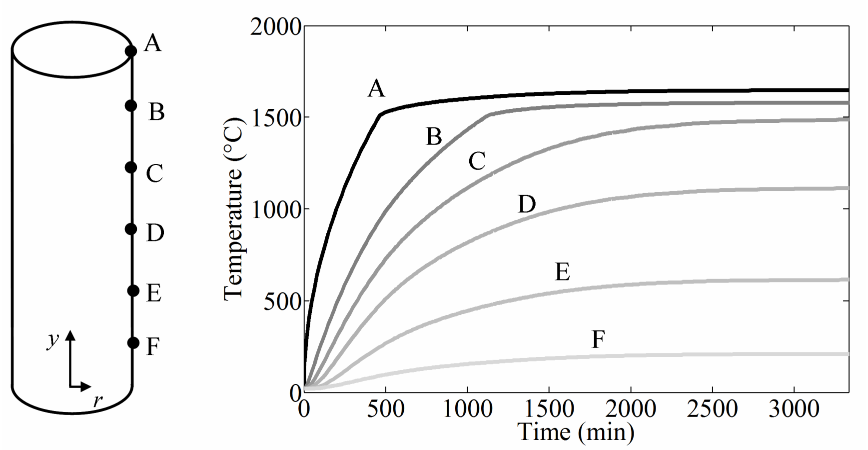

Figure 1.25: Temperature distribution during transient heating.

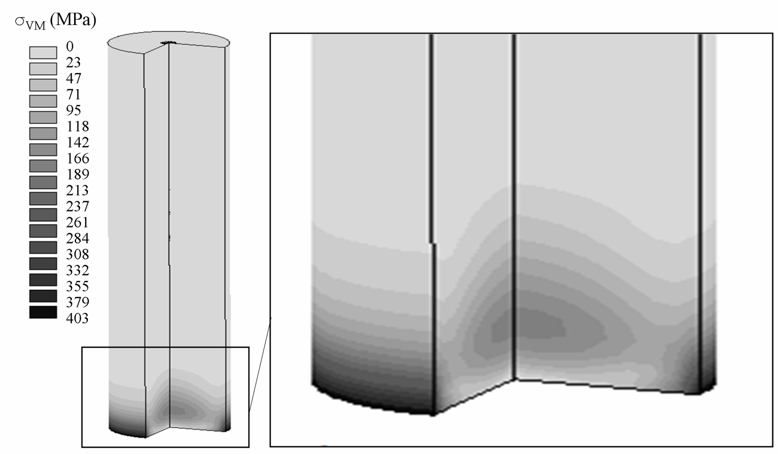

Figure 1.26: Stress distribution after heating.

variation, corresponding to the latent heat of the given material, which may give rise to numerical problems. Furthermore, this approach requires a transient analysis to be performed, thus strongly increasing the computational time, exponentially if the number of elements become higer. As it will be shown, an alternative simplified approach, reducing the computational time without introducing significant errors in results, can be followed.

The crucial point to avoid a more sophisticated transient analysis with enthalpy variation is related to a possible interpretation of the effect of the molten region on the mechanical behavior of the structure. The upper temperature of the slab in steady state conditions can be analytically achieved, considering absence of melting, with Equation (1.4) and (1.8).

$$T_2 = \dot{Q}\left(\frac{L}{\lambda_{sol}} + \frac{1}{h}\right) + T_b = 2522\ ^\circ\text{C} \tag{1.96}$$

This temperature is clearly unrealistic from a physical point of view, and the area that exceeds the melting point is identified with white color in the close view of Figure 1.27a, where the temperature scale is limited to material melting temperature.

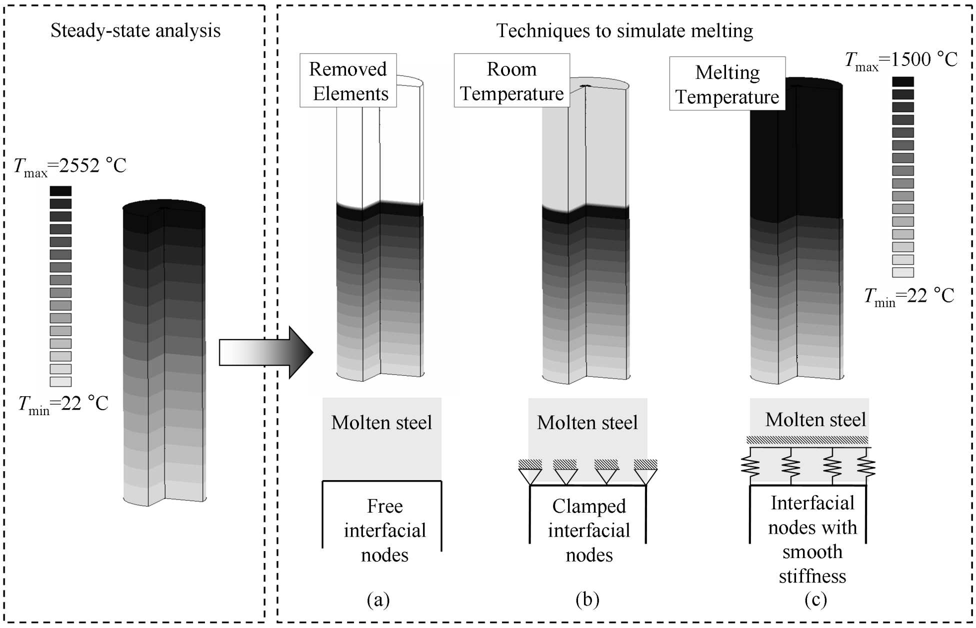

Figure 1.27: Techniques to simulate melting: (a) removed elements , (b) room temperature imposed and (c) melting temperature imposed.

Obviously this region (that is assumed to be liquid) does not affect the mechanical behavior of the underlying structure (still solid) and therefore it could be simply removed. In practice, at the beginning of mechanical simulation, those elements corresponding to the molten part are substituted with "soft" elements, characterized by a very low thermal expansion and modulus of elasticity, as schematically represented in Figure 1.27. It should be noted that the described strategy is somewhat approximate, as "soft" elements should be removed incrementally (when actual element temperature exceeds melting point) and not from the first load step. In fact, the analysis is non-linear and in the numerical solution algorithm (Newton-Rapshon), the applied thermal load is divided in load increments and increased step by step, thus the solution is "load path dependent".

On the other hand, in structural analysis the molten portion of the bar simply represents a mechanical constrain at interface between solid and molten material. From this standpoint, the adopted strategy represents a sort of "lower bound", in which all nodes at interface are completely free. An "upper bound" would be obtained by over-constraining displacements at the boundary nodes, which corresponds to impose a fixed fictitious room temperature to the portion of bar that melts (Figure 1.27b). If a portion of the cylindrical bar far from the molten region is considered, a similar stress status has been found to develop. The solution can then be considered as "path independent" and therefore, the modeling strategy characterized by the lowest computational time can be adopted.

As shown in Figure 1.27c, the temperature of all elements exceeding melting point is modified by simply imposing the melting temperature. In this way an "intermediate" boundary condition is found, where the interfacial nodes are constituted by a very smooth stiffness. This strategy permits to improve convergence and it also accounts for the leveling of temperatures that occurs during phase changes, as depicted in Figure 1.25. A similar approach is followed in Chapter (3), where the thermo-mechanical behavior of an anode adopted in electric arc furnaces is investigated.

Chapter 2

Damage Induced by Repeated Thermal Loads

Cyclic temperature oscillations could lead to severe damage in mechanical components, inducing irreversible strains and fatigue failures. In the following some typical material response under these loads are briefly investigated.

Some considerations about modeling of cyclic plasticity are then proposed: several models are available in literature to describe the actual behavior of material subjected to repeated loads involving plasticity, and their accuracy usually increases with complexity. However, for thermal stresses problems, it will be shown that simplified models can be adopted with a tolerable accuracy.

A correct evaluation of stress and strain levels can be useful to perform life predictions. In the last part of the Chapter an overview of fatigue-life relations is given, with particular emphasis to techniques that can be adopted in absence of cyclic data in treating thermal stresses problems.

2.1 Cyclic Thermal Stress

Periodical heating and cooling of mechanical parts component can give rise to cyclic stress-strain response pattern, which in turn cause damage and failure. In this section the effect of this alternate loading on thermal stresses is investigated, and a particular condition resulting from cyclic thermal loads acting together with a static mechanical load is then analyzed.

2.1.1 Effect of Repeated Heating and Cooling

A simple problem involving a bar cyclically heated and cooled, originally proposed in [9], is adopted to investigate the effect of repeated heating and cooling. The stress-strain curve for the material is assumed to follow an elastic-perfectly plastic model, with a straight line up to the yield stress (σ_y) and after the yielding point the stress is constant. The yield stress in compression is here assumed to be equal to the yield stress in tension. Further details about modeling of cyclic plasticity are given in the following. As previously stated, the thermal strain is not responsible of any damage into the material, while its conversion into mechanical strain could lead to static or fatigue failure. At the beginning of the process, the bar is assumed to be heated, so it is unstressed because its free expansion is allowed. As schematically represented in Figure 2.1, the bar is then constrained at its ends such no displacements are allowed in x-direction, and its length must remain constant. Maintaining this constraint, it is gradually cooled and heated between two temperature limits. The lower limit is assumed to be the reference temperature, T_0, at which the material does not show thermal expansion, while the upper limit is represented by the temperature T_1, being $\Delta T = T_1 - T_0$. As discussed in Chapter 1, during the first cooling process, a tensile stress develops in the bar because of the constraint. A stress due to thermal effects then arise, the amount of which, as well as the behavior of the material under subsequent heating and cooling phases, is related to the cyclic temperature range. Three different conditions are analyzed in the following, referring to increasing values of temperature range. The resulting mechanical stress-strain curves are plotted in Figure 2.2.

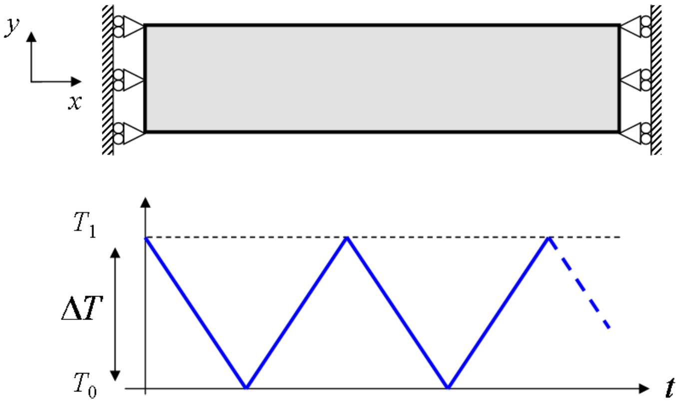

Figure 2.1: Bar constrained at its ends and cyclically heated.

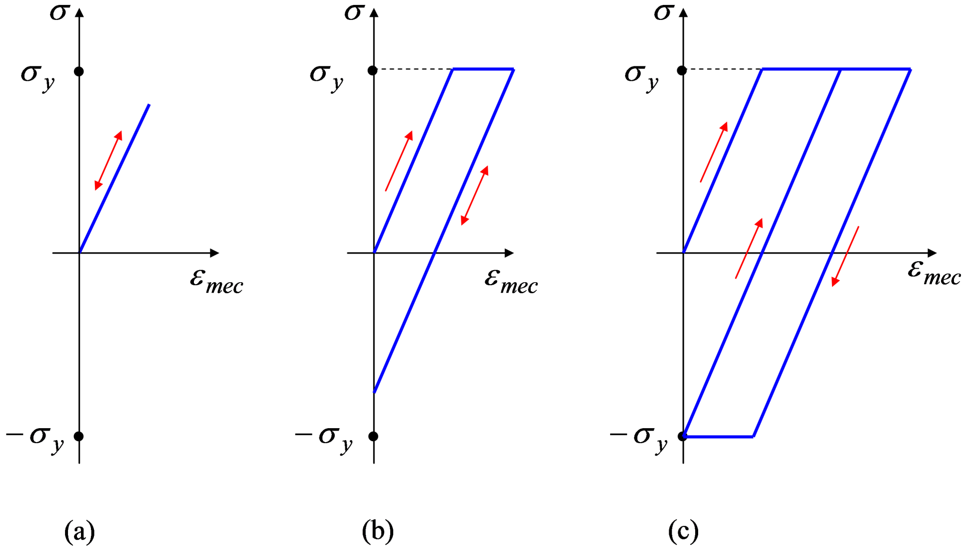

Figure 2.2: σ-ε curves for increasing values of temperature range: a) ΔT_1 not inducing plastic flow, b)$\Delta T_2 > \Delta T_1$ inducing plastic flow in tension, c) $\Delta T_3 > \Delta T_2$ inducing plastic flow in both tension and compression.

Considering a temperature range ΔT_1 that does not induce a thermal strain higher than the strain at the yielding point, σ_y, the resultant stress is directly proportional to the mechanical strain. In this case the following loading cycles lead the material to oscillate between a point beneath the yielding point and the no-stress condition. If the upper temperature is increased ($\Delta T_2 > \Delta T_1$), there is the possibility to induce into the material a strain that is greater than the strain at the yielding point under the first cycle of temperature reduction, so plastic flow occurs in tension. When the temperature is again raised to its initial value, the bar will reach a compressive state of stress, till the achievement of a zero strain condition when T_1 is finally reached. No further plastic flow is observed. This condition is achieved until the temperature difference of cycling is high enough to produce a thermal strain twice the elastic strain, but not greater. The following cycles will elastically occur between the yield stress in tension and the yield stress in compression. If the temperature difference induces a thermal strain greater than twice the elastic strain ($\Delta T_3 > \Delta T_2$), during the first cooling cycle the yielding point is reached and plastic flow occurs. As the bar is heated again, it unloads elastically but at the yielding point in compression it still has not achieved its initial length, and therefore, as the temperature is brought back to the initial value, plastic flow in compression also occurs.

During the subsequent cycles, an alternate tensile and compressive plastic flow can be observed. As it will be discussed in the following, the total mechanical strain ε_{mec} can be split into two parts: the elastic strain (ε_{el}) related to the stress through the elastic law, and the plastic strain (ε_{pl}).

$$\varepsilon_{mec} = \varepsilon_{el} + \varepsilon_{pl} \tag{2.1}$$

A plot of strains versus time can then be used to better clarify the relative amount of plastic, elastic and thermal strain in the bar for the case in which ΔT_3 is applied. As it can be seen, the sum of elastic and plastic strain equals (in absolute value) the thermal strain at any given time, as can be analytically obtained substituting Equation (2.1) in Equation (1.59). Such strain pattern can be responsible of low cycles fatigue failure of the material.

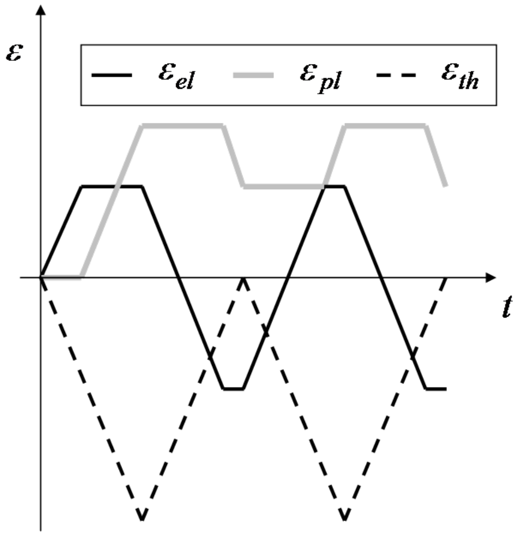

Figure 2.3: Elastic, plastic and thermal strain versus time when a high temperature range is applied.

2.1.2 Ratcheting

Thermal and mechanical loads can be cyclically applied in a combined way to a body. There is the possibility that the resulting condition that finally develops implies a progressive increase in stresses and strains even though the magnitude of the external loading does not increase in successive cycles. In such cases the failure of the structure may be due to excessive deformation or exceeding the static load-carrying capacity of the structure, rather than fatigue. For this reason thermal loads need to be accurately evaluated and considered during the design phase of mechanical components. The following example from [9] is used to better clarify the development of this dangerous situation, named *ratcheting*.

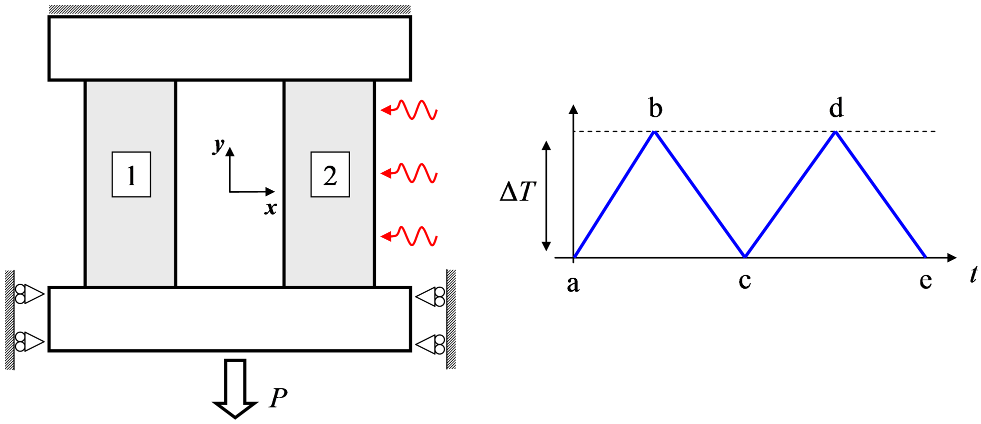

Figure 2.4: Two-bar assembly in which only one bar is heated and a load is applied.

Referring to the two-bar model analyzed in Chapter 1 to explain the partial constrain, an external load P is now applied to the attachment capable of displacements only along y-direction, as depicted in Figure 2.4. Also in this example, bar 2 is heated and cooled cyclically, while bar 1 is maintained at the reference temperature. The external load must be supported by the two bars together, but the fraction of the load carried by each bar is not constant during heating and cooling, as a result of progressive plastic flow. As in the previously analysis, ideal plasticity is here assumed, and the results are plotted in the σ-ε graph of Figure 2.5. At the starting point (a) the load P is uniformly distributed over the entire area $A_1 + A_2$, so that the average stress is:

$$\sigma^* = P/(A_1 + A_2) \tag{2.2}$$

The initial stress and strain relation of bar 1 and 2 are clearly identified by points (1_a, 2_a) in Figure 2.5, on the elastic portion of the stress-strain curve. If the temperature of bar 2 is uniformly increased, its expansion will transfer some of the load to the other bar that is kept at constant temperature; if $\alpha\Delta T$ is small, the action may be completely in the elastic range of the material, but if $\alpha\Delta T$ is large enough, the condition indicated by 1_b, 2_b may develop at the end of the first heating. Bar 1 experienced plastic flow, while bar 2 has unloaded elastically (points 1_b, 2_b). The stress at point 2_b can be determined considering that the total load sustained must still be P and σ_1 has become the yield stress:

$$\sigma_2 = \frac{A_1 + A_2}{A_2}\sigma^* - \sigma_y \tag{2.3}$$

The strain at 1_b is greater than the strain at 2_b by an amount $\alpha\Delta T$. When the temperature of bar 2 is returned to the reference value, bar 1, which has been permanently stretched, unloads elastically (line 1_b1_c), while bar 2 reaches the yielding point (line 2_b2_c). The stress at 1_c again is determined from the total load that must be supported:

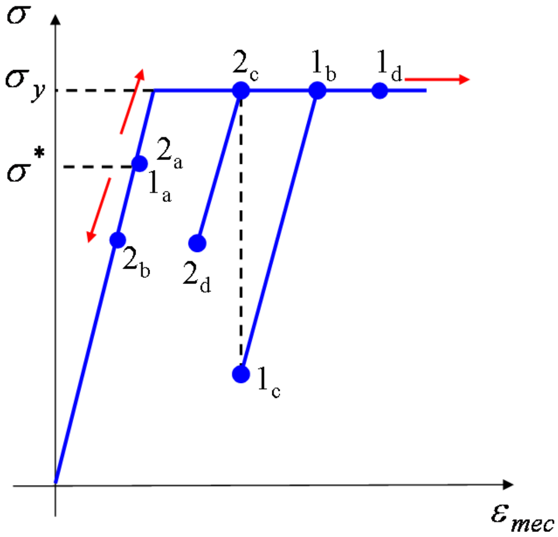

Figure 2.5: σ-ε curve in presence of ratcheting.

$$\sigma_1 = \frac{A_1 + A_2}{A_1}\sigma^* - \frac{A_2}{A_1}\sigma_y \tag{2.4}$$

The strain at 1_c is determined from the fact that since the two bars are now at the same temperature and their total lengths must be equal, their mechanical strains must be the same. It has to be noticed that, although bar 1 undergoes to tensile plastic flow during heating, no corresponding reverse plastic flow occurred during cooling. On the opposite, in bar 2, which was elastic during heating, tensile plastic flow occurs during cooling. The proposed strategy can be adopted to assess the stress-strain levels in the subsequent phases of heating and cooling (points d and e) in Figure 2.5.

It has to be noted that strains and plastic flow grow after each thermal cycle, and the overall length of the total assembly is permanently increased.

The increase in length per cycle, ε, is determined in [9] as:

$$\varepsilon = \alpha \Delta T - \frac{\sigma_y - \sigma_2}{E} - \frac{\sigma_y - \sigma_1}{E} \tag{2.5}$$

where σ_y, σ_1, $\sigma 2$ are the stresses at the extremes of the cycles as shown in Figure 2.5. Ratcheting occurs whenever $\varepsilon > 0$ or when the initial stress and the temperature range are sufficiently high to induce plastic flow in the non-heated bar during the first cycle. The relation among these quantities can be written as:

$$\sigma^* > \sigma_y - \frac{E \alpha T}{2 + A_1/A_2 + A_2/A_1} \tag{2.6}$$

As can be easily understood, ratcheting is a particularly serious form of thermal deterioration. In some cases the progressive distortion may reduce the functionality of the mechanical component. Even when increasing strains can be tolerated, however, the life can be drastically shortened.

2.2 Considerations About Modeling of Cyclic Plasticity

In this section, after some preliminary remarks about materials stress-strain response in monotonic loading, the behavior under cyclic loading involving plasticity is considered. Several models are available in literature to describe the mechanism of plastic strain. In a general situation related to mechanical loads, the choice of the material model is crucial in order to obtain accurate results; however, for thermal stresses problems, it will be shown that simplified models can be adopted with a tolerable accuracy.

2.2.1 Plastic Behavior in Monotonic Loading

Almost all materials have a range of loading below which the only mechanism of strain is reversible, giving rise to the phenomenon of elasticity. The limit above which permanent or irreversible strains exist is called yield stress (σ_y). Figure 2.6 schematically represents the behavior of a ductile material during a monotonic tensile test. At the beginning, the material exhibits linear elastic behavior, defined by a linear (E represents the elastic modulus) stress-strain relationship in which deformations are completely recoverable upon removal of the load. Beyond this linear region, deformations are plastic and can not be recovered during unloading. After the yield point, ductile metals will undergo a period of strain hardening, in which the stress increases again with increasing strain, and they begin to neck, as the cross-sectional area of the specimen decreases due to plastic flow. In a sufficiently ductile material, when necking becomes substantial, it causes a reversal of the engineering stress-strain curve; this is because the engineering stress is calculated assuming the original cross-sectional area before necking and the test is "strain-controlled". The reversal point is the maximum stress on the engineering stress-strain curve, that is usually defined as the tensile ultimate strength, σ_{UTS}.

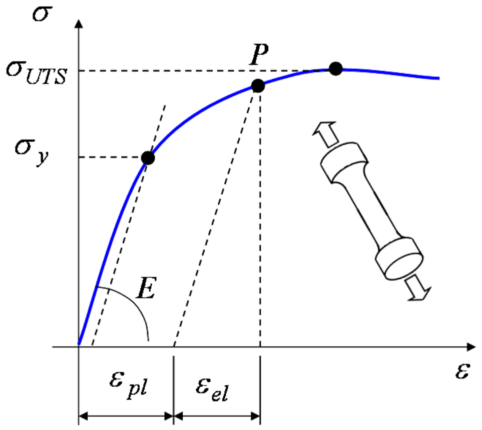

Figure 2.6: Elastic and plastic strain in a monotonic tensile test.

According to Equation (2.1), it is possible to split the mechanical strain, into two parts (elastic and plastic strain). The partial amount of these quantities can be easily understood referring to a general point P in Figure 2.6. The material behavior under monotonic tensile loads need to be modeled in a simplified way in order to obtain a solution to a deformation problem [28]. Several models are available in literature, with different levels of complexity.

An *Elastic-perfectly plastic* model, schematically represented in Figure 2.7a, neglect the effect of work hardening, assuming that the material is linear elastic and as the load on material increases to yield point it's stress state remains constant. The uniaxial tension stress-strain relation may be expressed as:

$$\begin{cases} \varepsilon = \dfrac{\sigma}{E} & \text{for } \sigma \leq \sigma_y \\ \varepsilon = \dfrac{\sigma}{E} + C & \text{for } \sigma > \sigma_y \end{cases} \tag{2.7}$$

where E is Young's modulus and C is a scalar greater than 0 to be determined.

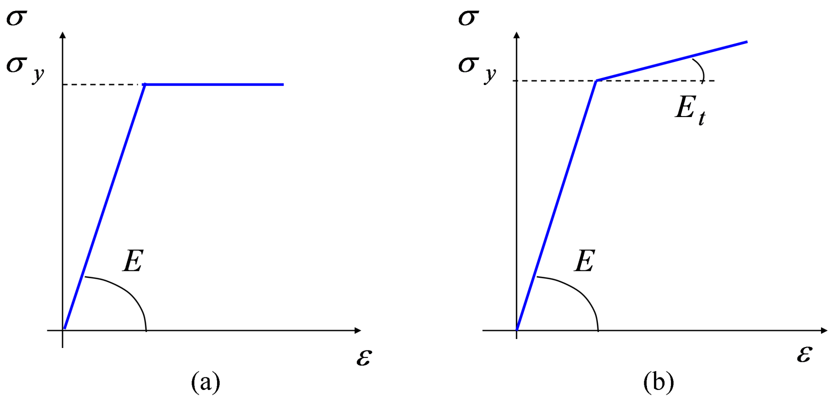

Figure 2.7: (a) Elastic-perfectly plastic model and (b) Elastic-linear work-hardening model.

In an *Elastic-linear hardening* model the material behavior is approximated by two straight lines, the first one representative for the elastic domain and the second one for the plastic domain, as depicted in Figure 2.7b. The first has a slope corresponding to Young modulus, while the slope of the second line is representative of the characteristic hardening of actual stress-strain curves and it is generally named tangent modulus, E_t.

$$\begin{cases} \varepsilon = \dfrac{\sigma}{E} & \text{for } \sigma \leq \sigma_y \\ \varepsilon = \dfrac{\sigma_y}{E} + \dfrac{1}{E_t}(\sigma - \sigma_y) & \text{for } \sigma > \sigma_y \end{cases} \tag{2.8}$$

In addition to the yield stress parameter, that identifies the transition point between the two lines, only the tangent modulus E_t is then needed to completely describe the plastic region. If $E_t = 0$ the model collapses into an elastic-perfectly plastic scheme.

In an *Elastic-exponential hardening* model the plastic portion of the stress-strain curve is represented adopting an exponential law, see Figure (2.8)a.

$$\begin{cases} \varepsilon = \dfrac{\sigma}{E} & \text{for } \sigma \leq \sigma_y \\ \varepsilon = \left(\dfrac{\sigma}{H_1}\right)^{\frac{1}{n_1}} & \text{for } \sigma > \sigma_y \end{cases} \tag{2.9}$$

The characteristic constants H_1 and n_1 can be determined in order to fit the experiments curve ($n_1 = 0.05 \div 0.4$ for metals). The starting point of the plastic curve is represented by the yielding stress and the corresponding strain. For this reasons H_1 and n_1 are strictly related to σ_y.

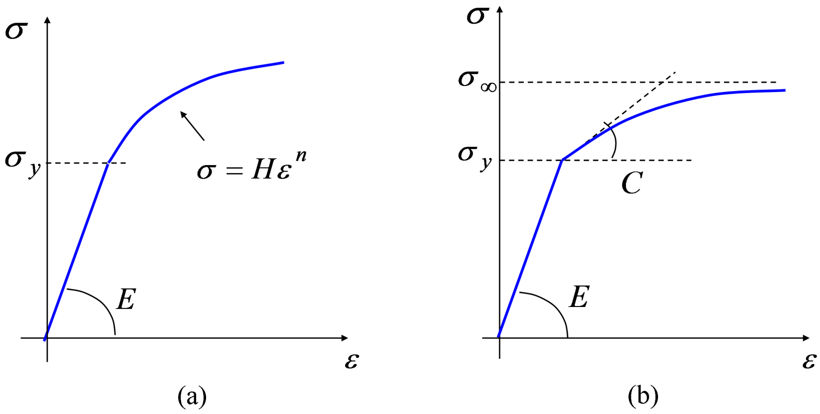

Figure 2.8: (a) Elastic-exponential hardening model and (b) Chaboche model.

Adopting a *Chaboche* model, according to [29, 30] , after the yielding point the stress can be related to the plastic strain with the following expression:

$$\sigma - \sigma_y = \frac{C}{\gamma} \tanh(\gamma \Delta \varepsilon_{pl}) \tag{2.10}$$

Where C represents the initial hardening modulus, as depicted in (2.8)b. It is evident that the hardening modulus decreases with the increase of plastic strain, the constant γ being responsible of the rate at which the hardening modulus changes. The asymptotic value of stress for large strains can be obtained as:

$$\sigma_\infty = \sigma_y + \frac{C}{\gamma} \tag{2.11}$$

2.2.2 Plastic Behavior in Cyclic Loading

Considering cyclic loading conditions, in which the material is periodically loaded in both tension and compression, the evolution of elastic and plastic strain needs to be taken into account. Referring to Figure 2.9, in which a sample is subjected to a sequence of *strain-controlled* cycles, according to a perfect plasticity scheme, a stabilized condition can be obtained after the first cycle. But some materials exhibit more complicated behavior under cyclic loading, such as *hardening* and *softening*, as schematically represented in Figure 2.9, and stabilized conditions are often reached only after a huge amount of periodical stress-strain cycles. For initially soft materials, such as annealed metals, the early cycles may show increasingly higher stresses developing as measured at the tip ends of the hysteresis loop. Materials that have been previously work hardened will soften from cycle to cycle as they are strained repeatedly. Successive cycles of plasticity reduce the stresses required to induce a specified strain. But, as with hardening, the softening diminishes with applied cycles, eventually reaching a stable hysteresis loop before the life of the specimen is exhausted [31]

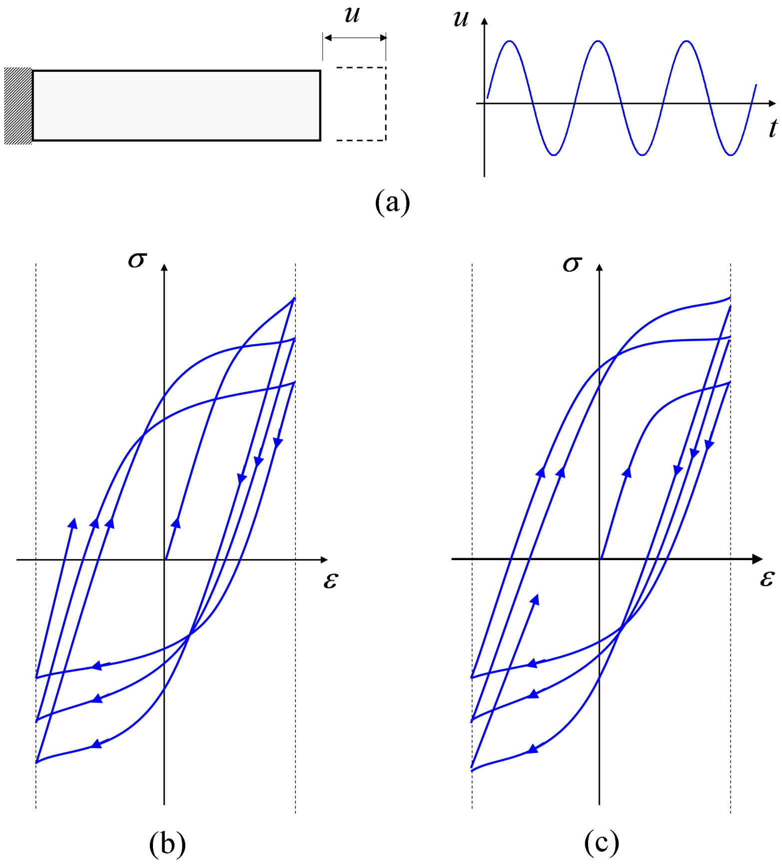

(a)

(b)

(c)

Figure 2.9: (a) Strain-controlled test with cyclically (b) softening and (c) hardening material response.

As stated before, materials have an elastic range within which they respond in a purely elastic manner. The boundary of this range, in either stress or strain space, is called the *yield surface*. The shape of the yield surface depends on the behavior of material and on the entire history of deformation. Inside of the yield surface is the elastic domain, while plasticity is described by the surface itself [32]. Several models can be found in literature to describe the yield surface [33, 34]. As proposed in [35] the yield surface is expressed in terms of three-dimensional principal stress space $(\sigma_1, \sigma_2, \sigma_3)$, as

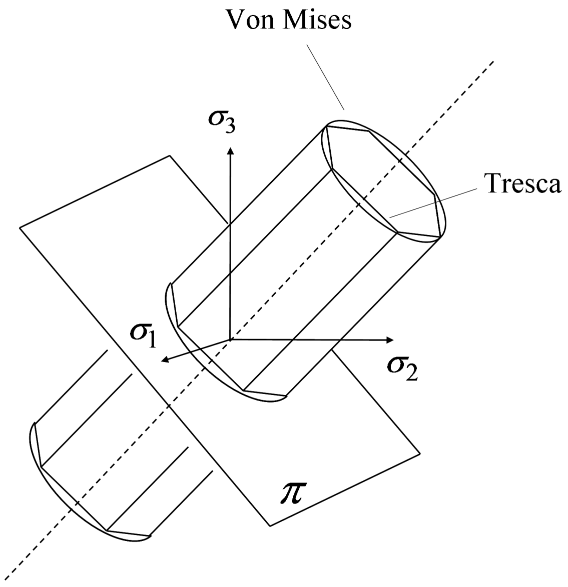

Figure 2.10: Examples of yield surfaces in principal stress space.

schematically represented in Figure 2.10, in which also the deviatoric plane π (perpendicular to the hydrostatic axis) is represented. According to the *Tresca criterion*, also known as the maximum shear stress theory, the yield surface is expressed as:

$$\frac{1}{2}\max(|\sigma_1 - \sigma_2|, |\sigma_2 - \sigma_3|, |\sigma_3 - \sigma_1|) = \frac{1}{2}\sigma_y \tag{2.12}$$

where σ_y is the tensile yield strength. As depicted in Figure 2.10, the yield surface is a prism of six sides with infinite length. This means that the material remains elastic when all three principal stresses are equivalent (hydrostatic pressure). However, when one of principal stresses becomes smaller (or larger) than the others the material is subject to shearing. In such situations, if the shear stress reaches the yield limit then the material enters the plastic domain.

The *von Mises criterion* seems to agree somewhat better, in general, with experimental data related to ductile materials, such as metals. It expresses the yield surface as:

$$(\sigma_1 - \sigma_2)^2 + (\sigma_2 - \sigma_3)^2 + (\sigma_3 - \sigma_1)^2 = 2{\sigma_y}^2 \tag{2.13}$$

The yield surface is then a cylinder of infinite length, the axis of which lies along the value $\sigma_1 = \sigma_2 = \sigma_3$ (hydrostatic axis), as represented in Figure 2.10.

To account for the behavior of materials with different limit in traction and compression, other criteria have been developed, such as the *Drucker-Prager*, the *Mohr-Coulomb*, the *Bresler-Pister* criterion. An exhaustive review of existing models can be found in [35, 34].

In order to correctly model the mechanism that give rise to hardening or softening behavior, a brief overlook about the evolution of yield surface and the so-called hardening rules is given.

The shape and size of the yield surface change as the plastic deformation evolves. Hardening rules describe how the yield surface changes as yielding occurs. A change of the yield surface size is connected to isotropic hardening and a change of location of the center to kinematic hardening. Referring to Figure 2.10, hardening rules will be presented in a plot where the yield surfaces are sketched in principal stress space. In particular the behavior on deviatoric plane π is considered adopting the Mises criterion, in comparison with the resulting effect on an elastic-linear hardening model. This is a schematic, but effective, procedure that can be used to evaluate the differences between the various rules.

The basic rule describing the behavior in the plastic domain is the *isotropic hardening*. Isotropic hardening describes a dilation or isotropic expansion of the yield surface. It implies that the position of the center of the yielding surface remains the same during plastic flow. This property leads to an increase of yield stress with no correlation to the loading direction, as can be seen in Figure 2.11. Since the elastic domain expands uniformly, if loading is reversed yielding occurs at a value of $2\sigma_{max}$.

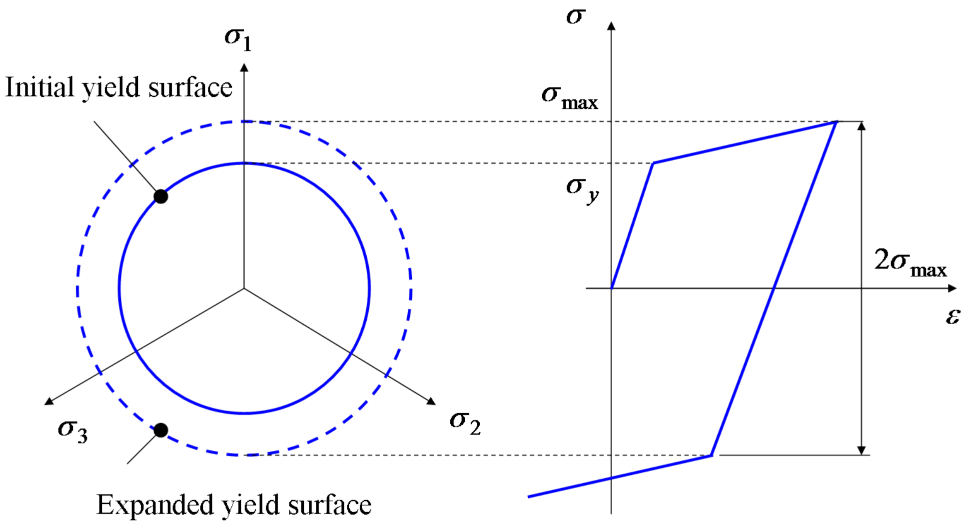

Figure 2.11: Schematic evolution of isotropic hardening model.

When the yield surface translates its center to a new position, as depicted in Figure 2.12, *kinematic hardening* takes place. This rule was developed to model the Bauschinger effect (named for the German scientist who first described it around 1860), according to which the yield stress is higher when the material is loaded under tension and gets smaller for a compressive loading case, a behavior seen by most metals. Hence, if loading is reversed, yielding occurs in compressing at a value of $2\sigma_y$ with respect to actual stress state. Obviously, during the first tractive loading, kinematic and isotropic hardening rules provide the same material response.

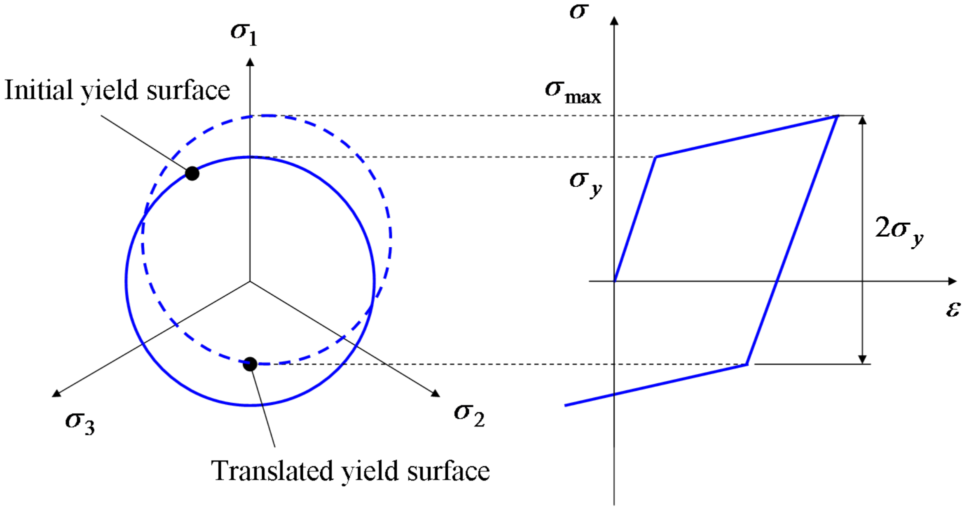

Figure 2.12: Schematic evolution of kinematic hardening model.

A more complex behavior can be described by a *combined* model, which causes a simultaneous expansion and translation of the yield surface as represented in Figure 2.13.

The evolution of yield surface can be expressed with a non-linear hardening law, such as in [36].

$$\sigma_y = \sigma_{y0} + Q[1 - e^{(-b\varepsilon_{pl})}] \tag{2.14}$$

where σ_{y0} denotes the initial size of the yield surface, Q the maximum change in the size of the yield surface and b defines the rate at which the size of the yield surface changes as plastic straining progresses.

2.2.3 Simulated Cyclic Behavior

In this section the cyclic behavior of a material modeled in different ways is considered. In particular an isotropic, a kinematic and a combined model

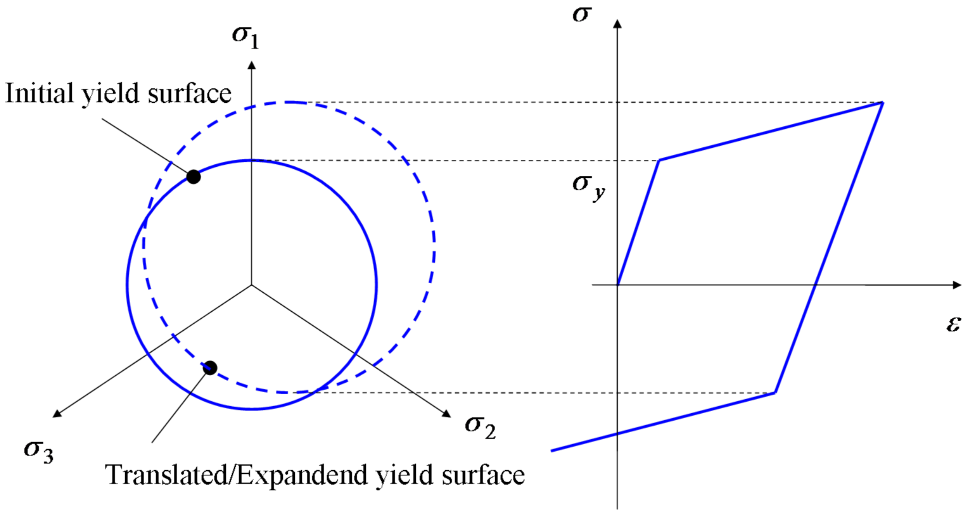

Figure 2.13: Evolution of yield surface in a combined model.

are taken into account, with the same value of initial yield stress. Cyclic tests under four different loading conditions are performed: stress-controlled, strain-controlled, thermal and thermo-mechanical cycles are considered, in order to evaluate the evolution of stress-strain curves and assess the most appropriate model to be adopted.

As sketched in Figure 2.14, simple geometries are adopted, to focus only on the material behavior. A bar and an hollow cylinder allow to investigate the whole set of aforementioned loading conditions. Simulations are performed with ANSYS®software, and in Figure 2.15 the geometrical parameters of the models are depicted, while their values, as well as the input loads, are summarized in Table 2.1.

In the following, the elastic-linear hardening model is adopted for the implementation of the isotropic and the kinematic rule, while, according to several works in literature [37, 38], a mixed model based on non-linear isotropic hardening, Equation (2.10), and the non-linear kinematic hardening law, Equation (2.14), is adopted to account for cyclic hardening (or softening).

An example of ANSYS®parametric syntax for the implementation of the isotropic, kinematic and combined model is here proposed.

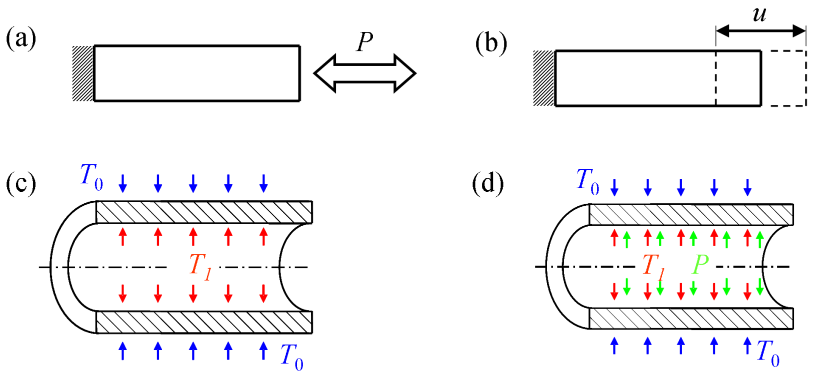

Figure 2.14: Loading conditions investigated: (s) stress-controlled, (b) strain-controlled, (c) thermal and (d) thermo-mechanical load.

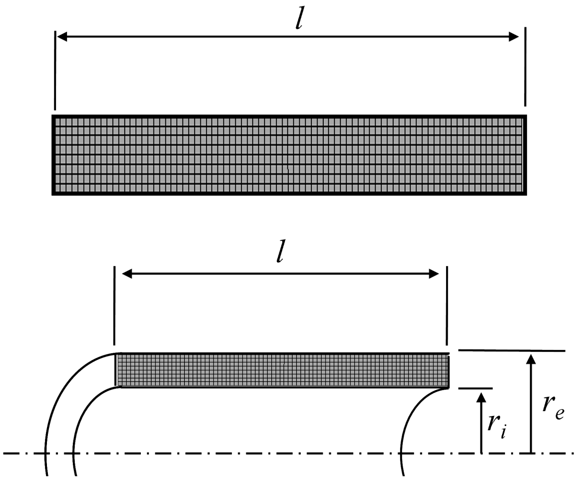

Figure 2.15: Numerical models adopted in simulations.

Table 2.1: Geometrical parameters and loads adopted in simulations.

	Parameter	**Value**
Bar	l, m	0.2
	u, m	0.001
	P, MPa	450
Cylinder	l, m	0.5
	r_i, m	0.05
	r_e, m	0.01
	T_0, °C	20
	T_1, °C	450
	P, MPa	180

```
TB,BISO,1,1
TBTEMP, 20
TBDATA,, Rs, Et

!----------------------

TB,BKIN,1,1
TBTEMP, 20
TBDATA,, Rs, Et

!-----------------------

TB,CHABOCHE,1,1
TBTEMP,20
TBDATA,,Rs,Et,gamma
TB,NLISO,1,1
TBTEMP,20
TBDATA,,Rs,0,Q,b
```

Table 2.2 summarizes the material parameters adopted in simulations. It has to be noticed that these values are not representative of a given material, but they are used in simulation with the methodological aim of understanding the model response under different loading conditions. The combined model is set up in order to obtain a softening response of the material under repeated loads. In practice, a huge amount of experimental data is required to assess an appropriate calibration for a given material, as pointed out in [37, 36].

As can be seen in Figure 2.16a, for a *stress-controlled* test, a sample clamped at an end is considered, while a periodic pressure P is imposed on the free end in the axial direction. The peak values of the applied pressure (both in tension and compression) are higher than the value of yield stress.

A similar approach is adopted to evaluate the effect of different material

Table 2.2: Material parameters adopted in simulations.

	Parameter	**Value**
Elastic line	E, GPa	210
	ν	0.3
Kin/Iso hardening	σ_y, MPa	400
	E_t, MPa	10000
Combined model	C, MPa	150000
	G, MPa	-150
	γ	500
	b	80

models in the case of *strain-controlled* test, where a strain sufficiently high to cause plasticity is imposed in tension and compression to the same specimen. The free end of the cantilever in this case is forced to follow a periodic displacement u, as sketched in Figure 2.17a. In order to obtain a pure *thermal* loading, a different model need to be considered: as already pointed out, thermal stresses in a bar results from external restrains on its ends, while other geometries can be considered as self-restrained towards thermal loads. In this simulation an hollow cylinder is considered: the cyclic stress is due to a sequence of heating and cooling at temperature T of the inner part, while the external surface is maintained at a constant temperature T_0, as sketched in Figure 2.18. It has to be noticed that the analytical evaluation of thermal stresses for the whole domain of this model has been treated in Chapter 1, while the focus is now on the stress-strain evolution in a single point on the inner hot surface. When performing a simulation in which the component undergoes temperature gradients, the variation of yield stress and elastic modulus with the increase of temperature should be considered, as already pointed out. In this case the aim is not to obtain the exact distribution of stresses, but to analyze the cyclic evolution of stress-strain curves for a given material model under different loading conditions. For this reason values in Table 2.2 are considered for the whole temperature range. Results are shown in Figures 2.16, 2.17, 2.18, 2.19 in terms of stress-strain cycles.

As can be seen, a model with isotropic hardening tends to stabilize into a purely elastic loop. In a stress-controlled simulation, the stabilization takes place after the first loading, while in the other tested condition the elastic shakedown occurs after some repeated loadings. For this reason it can be concluded that purely isotropic hardening is not the appropriate choice dealing with cyclic loads, and it is generally used for modeling under unidirectional monotonic loading.

Considering results from stress-controlled, strain-controlled, and thermal simulations, it can be noted that models based on kinematic hardening rules show a stabilization into an elastic-plastic hysteresis loop after the first cycle. On the opposite, simulations in which a combined model was implemented, correctly represent the softening behavior of the material. The use of an inadequate model may than affect life predictions and an incorrect stress distribution can be found. A calculation made with asymptotic conditions (i.e. with a low yield stress) leads to consider as plastically deformed some regions which actually remain elastic and are never softened [39]. However, sophisticated models require a calibration for a bigger number of material parameters, and a simulation for the total number of cycles should be implemented, which is often computationally unfeasible in the case of complex geometries.

Considering in a more detail the results obtained for the cylinder thermally loaded, it is possible to notice that, although the shapes of stabilized cycles in Figure 2.18b and Figure 2.18c are different, the resultant total strain range is the same, due to the fact that in this case the material undergoes a sort of strain-controlled cyclic loading. These results confirm that, for the particular case of mechanical components only thermally loaded, the choice of material model is not as relevant as for other loading conditions: the relative amount of elastic and plastic strains strongly depends on the adopted material model, but, as the problem is characterized by self-imposed constrained thermal expansion, the total amount of strain remains constant. This consideration leads to the adoption of a simple kinematic hardening model to perform preliminary life calculations.

This approach is not further valid in the case of thermo-mechanical loads. In fact, as shown in Figure 2.19, a superimposition of an external load, P, give rise to the previously treated ratcheting condition, for which no stabilized condition can be found. In that situation the correct choice of material model is crucial to correctly predict the behavior under cyclic loads.

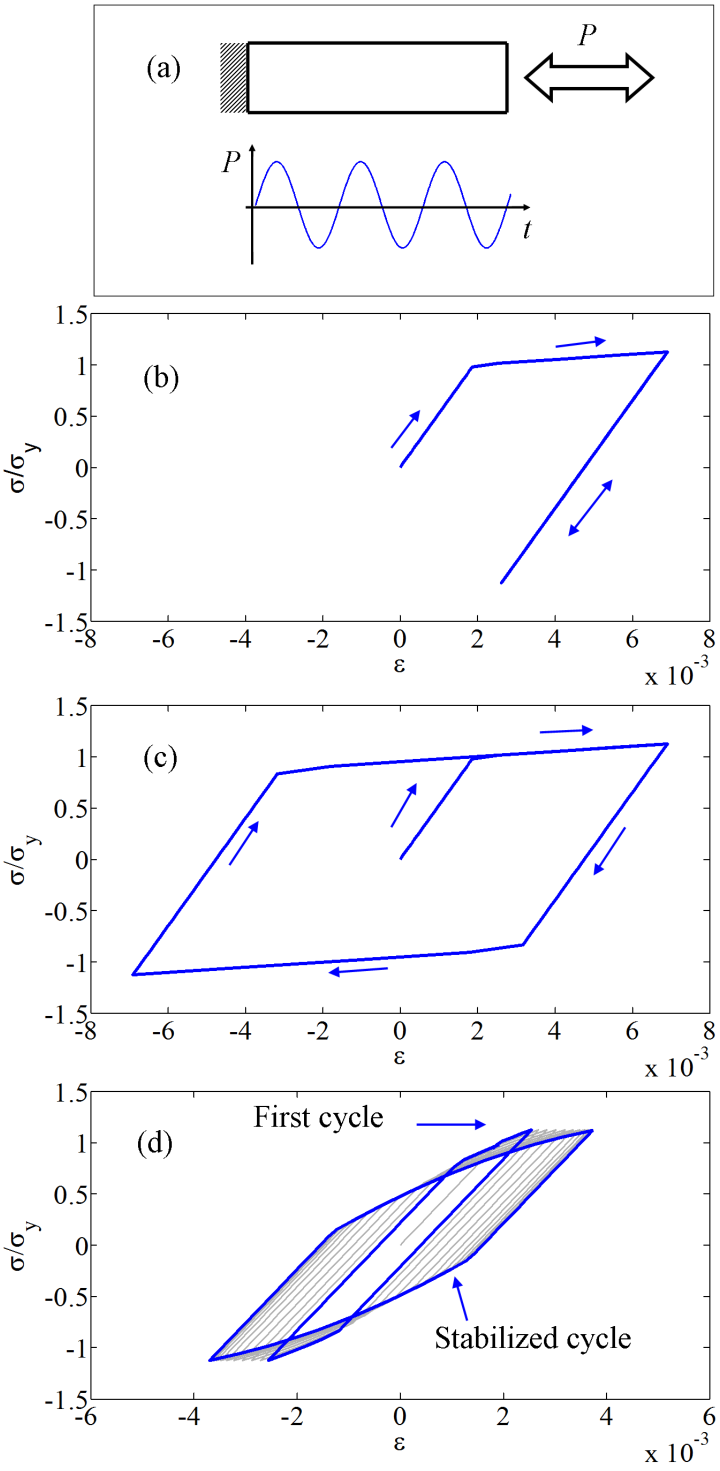

Figure 2.16: Stress-strain cycle in a stress-controlled test. (a) Scheme of the simulation, (b) isotropic hardening model, (c) kinematic hardening model and (d) combined model.

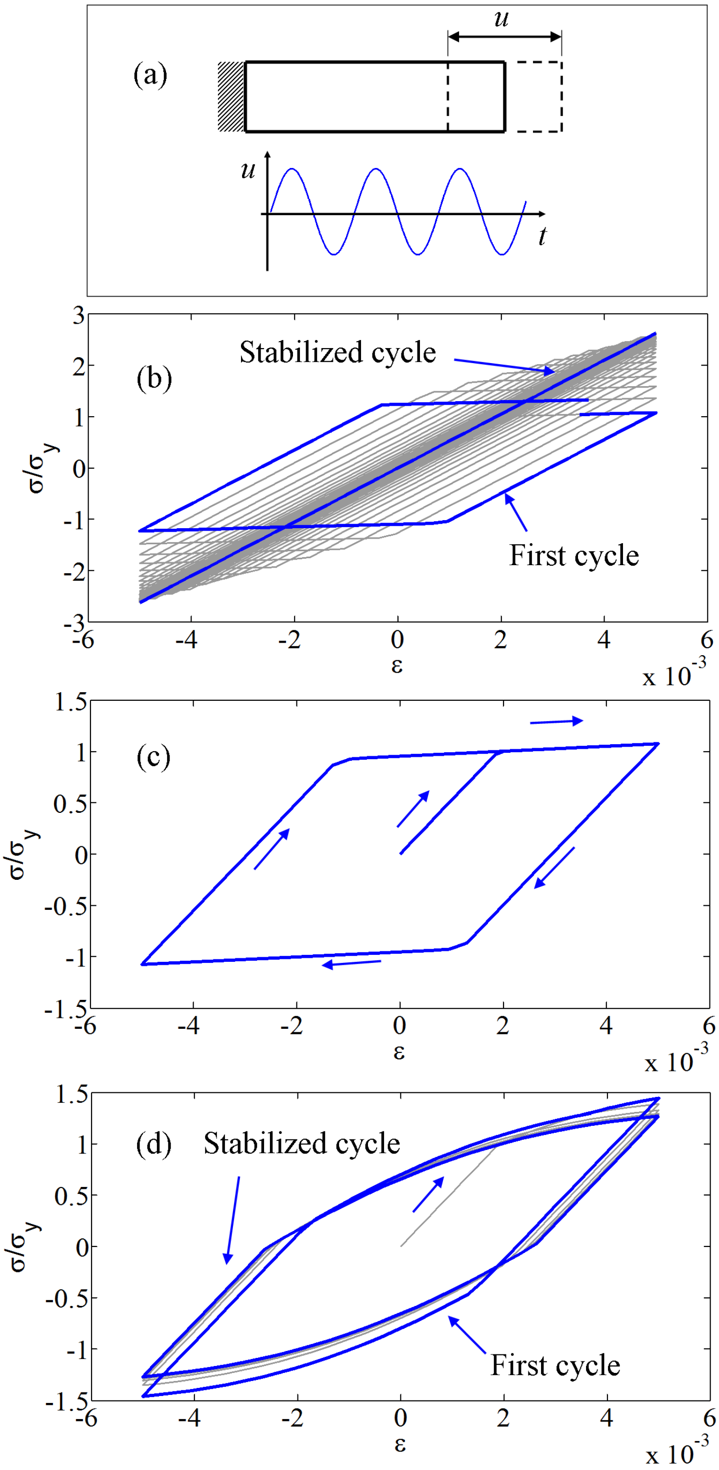

Figure 2.17: Stress-strain cycle in a strain-controlled test. (a) Scheme of the simulation, (b) Isotropic hardening model, (c) kinematic hardening model and (d) combined model.

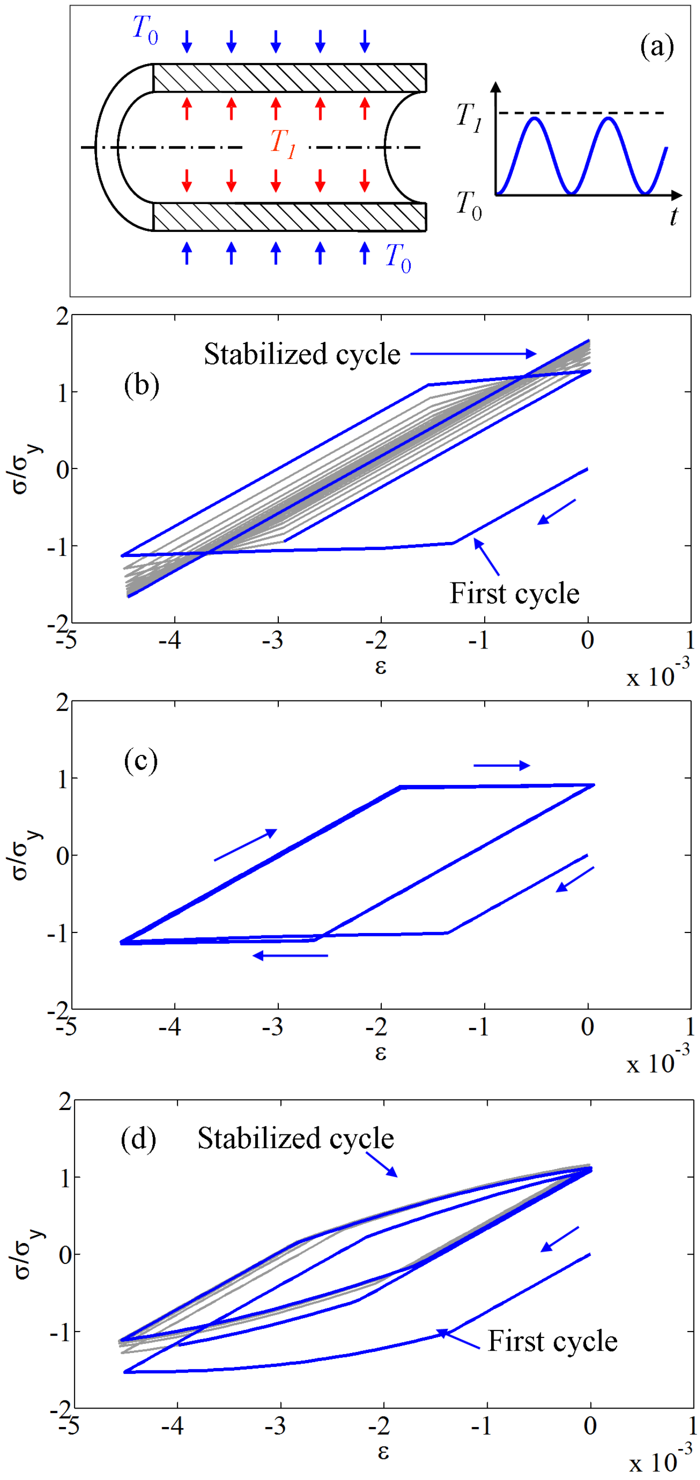

Figure 2.18: Stress-strain cycle in a thermal stressed component. (a) Scheme of the simulation, (b) Isotropic hardening model, (c) kinematic hardening model and (d) combined model.

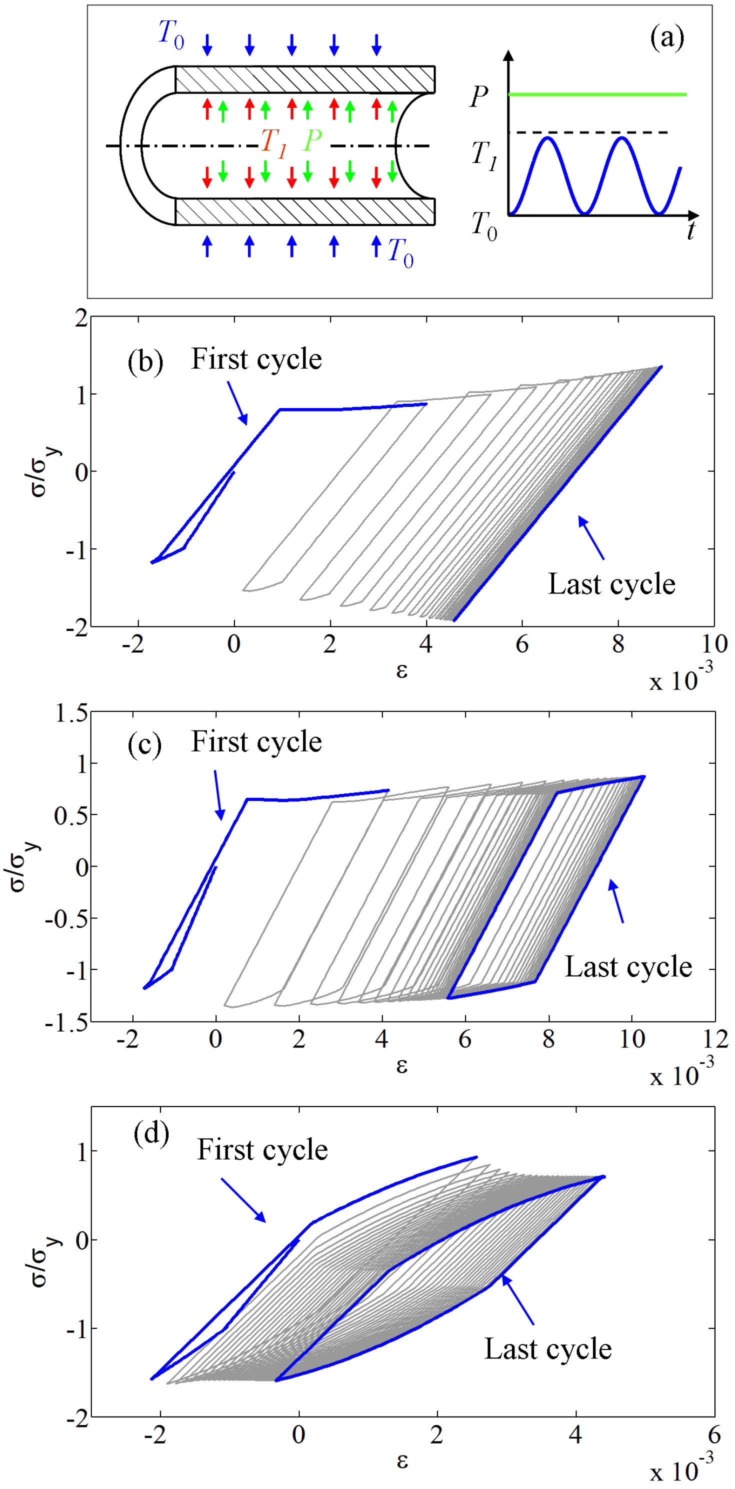

Figure 2.19: Stress-strain cycle in a thermo-mechanical stressed component. (a) Scheme of the simulation, (b) Isotropic hardening model, (c) kinematic hardening model and (d) combined model.

2.2.4 Cyclic Stress-Strain Curve

As evident from Figure 2.9, during cyclic loading the mechanical properties of a material can change. In particular, stress-strain response of cyclically loaded material can be different from the one when it is loaded monotonically. During cyclic loading, material may exhibit strain hardening, strain softening or its response can be stable. The ratio between the ultimate tensile strength and the yielding stress, σ_u/σ_y, in a monotonic tensile test is usually adopted [31] to provide a quantitative measure of whether a material is likely to harden or soften during cycling. If $\sigma_u/\sigma_y > 1.4$, the material will harden under cyclic loading; if $\sigma_u/\sigma_y < 1.2$, the material will soften. For values between 1.2 and 1.4 some materials exhibit hardening, other softening, and a few remain stable. After hardening/softening is completed, the cycled material exhibits a steady-state behavior. Stress and strain amplitudes have reached their saturated values, and there are no further changes in the hysteresis loop shape. If a series of strain-controlled tests is performed at different amplitudes (ε^* and ε^{**} in the example of Figure 2.20), a set of stable loops can be obtained for the characterization of the steady-state behavior for the whole range of the loading amplitudes. The curve connecting the tips of such stable loop gives the relation between the saturated stress and strain amplitudes and is called the cyclic stress-strain curve [40]. This curve can be analytically modeled with a law that allows the description of the stress-strain relation with a single equation (the so-called *Ramberg-Osgood*

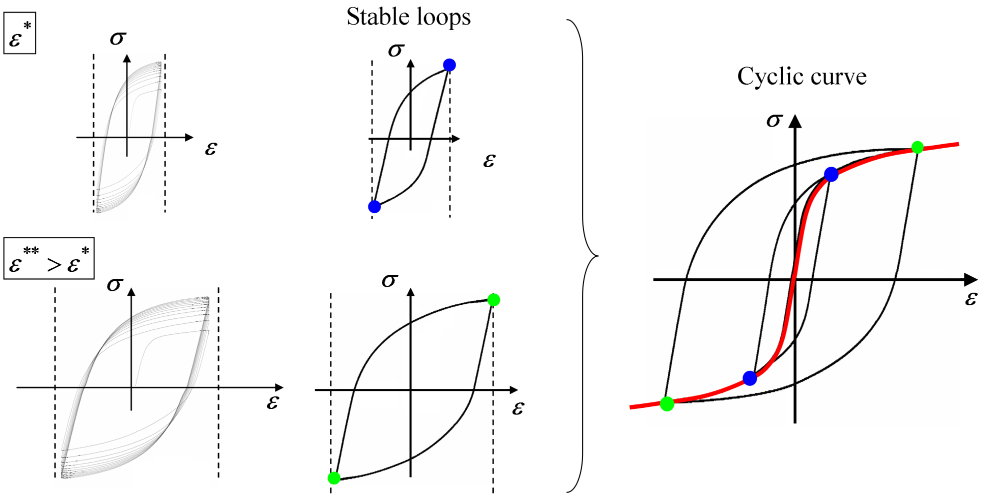

Figure 2.20: Cyclic stress-strain curve.

Table 2.3: Parameters adopted in simulations.

	Parameter	**Value**
Experimental curve[a]	H', MPa	326.6
	n'	0.147
Hardening parameters[b]	C, MPa	64257
	γ	888
	G, MPa	76
	b	8

[a] Data from [41]

[b] Data from [37]

model):

$$\varepsilon_a = \frac{\sigma_a}{E} + \left(\frac{\sigma_a}{H'}\right)^{1/n'} \tag{2.15}$$

where ε_a and σ_a are the amplitudes of stabilized strain and stress respectively, while H' and n' are material parameters (metals usually have $n' = 0.1 \div 0.2$). The cyclic stress-strain curve can greatly differ from the static tensile response for a given material, and a cyclic yield stress, σ'_y, can also be evaluated. Hence, the cyclic stress-strain curve is one of the most important characteristic of a material under cyclic loading conditions [40]. Even if the hardening (or softening) is more evident in the earlier cycles and tends to gradually reduce, a huge amount of repeated loads is required to reach the stable hysteresis loop. Nevertheless, recognizing that for many materials the stabilized value of stress is achieved before the specimen fails (a well-established rule is to consider as fully developed the condition at $N_f/2$), suggests that a single specimen can be used to study several strain levels. A review of the available techniques for the experimental determination of the cyclic stress-strain curve is given in [31].

In Chapter 3 the thermo-mechanical analysis of an anode adopted in arc furnaces is performed. As it will be shown, this component undergoes a cyclic thermal load, and the cyclic response of the material that constitutes the most critical area of the component (copper) need to be evaluated.

For this reason, a numerical simulation adopting a simplified geometry is here performed. A planar specimen is considered to be cyclically loaded in strain-controlled conditions, as depicted in Figure 2.17. Adopting values for C, γ, G and b parameters available in [37] for the pure copper at room temperature and summarized in Table 2.3, a combined model can be numerically implemented to account for cyclic hardening or softening behavior.

Strain-controlled simulations are then accomplished, until the asymptotic conditions are reached. This procedure is followed for several strain levels, and the tips from the family of multiple loops are connected to form the cyclic stress-strain curve. Results from numerical simulations are compared with experimentally evaluated trend available in [41], and the good agreement of the trends is shown in Figure 2.21.

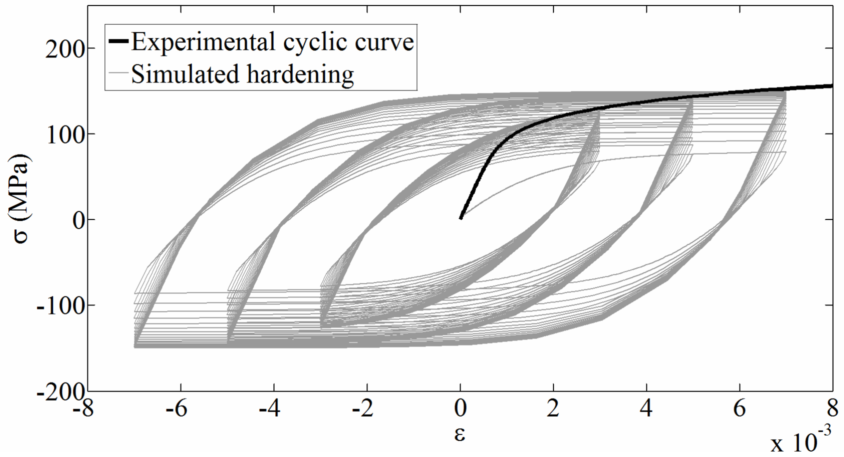

Figure 2.21: Numerically evaluated cyclic stress-strain curve for copper.

As already pointed out, a huge amount of cycles is required to reach a stable condition. Although more accurate, a combined model could be not appropriate to perform fast simulations, especially dealing with complex models with an high number of elements. For this reason, as it will proposed in Chapter 3, the current practice is to refer to an *Elastic-linear hardening* model calibrated on the basis of stabilized conditions, neglecting the initial hardening (or softening) behavior.

2.3 Fatigue-Life Relations

A metal subjected to repetitive or fluctuating stress is shown to fail at a stress lower than that required for failure with a static application of the same load. Literature accounts for failures occurring under cyclic loading as fatigue failures. Alternating loads on shafts and rods, stresses in turbine blades due to vibrations, as well as fluctuating thermal stresses during plant start-stop cycles are some examples of cyclic loading that may cause fatigue. In the earlier studies about this topic, researchers were focused into the characterization of the fatigue resistance of many materials.

In more recent years the interest in the study of high-strain, low-cycle fatigue, has grown, because economic design dictates that some plasticity can be tolerated, and finite life accepted, at least in the critical regions of many engineering components. In this chapter a brief review about these two approaches is described, with a concluding section concerning suitable predictive models to be adopted in treating thermal stresses problems. More detailed discussion on this topic can be found in specific literature, such as [42, 31].

2.3.1 Stress- and Strain-Based Approach

Although the first author who officially works on fatigue of mechanical components, establishing a correlation between applied loads and durability of mining chains, was W. Albert in 1839, the modern study of this subject is generally dated from the work of A. Wöhler, who started his research activity from 1852. Wöhler was concerned by the failure of axles at loads considerably less than expected, and he conceived a testing machine, simulating a railcar axle. A railcar axle is basically a round beam in four-point bending, which produces a compressive stress along the top surface and a tensile stress along the bottom. After the axle has rotated a half turn, the bottom becomes the top and vice versa, so the stresses on a particular region of material at the surface varies sinusoidally between tension and compression. This is now known as fully reversed fatigue loading.

Wöhler focus was to determine a stress level below which an indefinite number of reversals could be sustained without specimen fracture. Basically, for a constant cyclic stress amplitude, he noted the number of cycles that led to failure, and he repeated the procedure for various amplitudes of the applied load. Although he actually never plotted his data, the reports that he published led engineers later to construct the S-N (stress versus number of cycles to failure) curve that is attributed to him. Basically, the stress is plotted on the vertical axis and cycles to failure on the horizontal axis. The

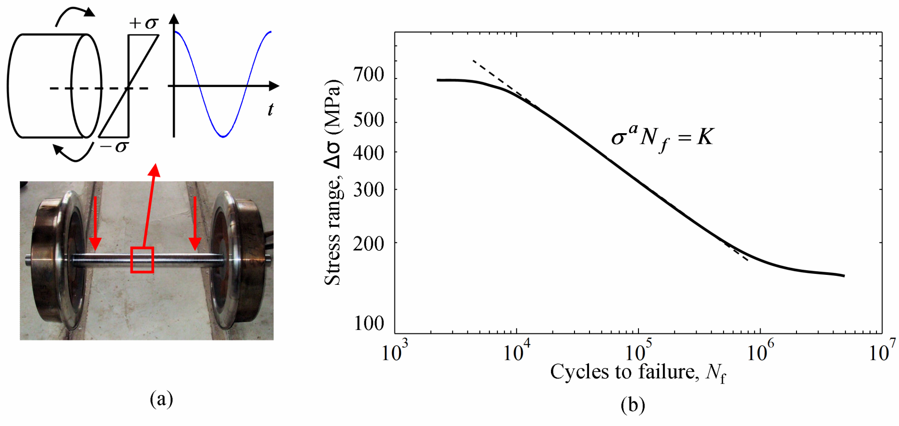

Figure 2.22: (a) Fatigue in a railcar axle and (b) example of *S*-*N* curve.

scale for cyclic life is usually logarithmic in order to plot conveniently the large variations of life at different stress levels. *S*-*N* curves for metals usually show a linear trend if $10^3 < N_f < 10^6$, that can be described by the following equation:

$$\sigma^a N_f = K \tag{2.16}$$

where a and K are parameters characteristic of each material, while N_f is the number of cycles to failure.

It has to be pointed out that the determination of a *S*-*N* diagram for a single material requires a huge amount of experimental data. In fact each point in the curve, relating a single value of stress to its corresponding number of cycles to failure, is the result of a statistical fitting of several test for that given stress amplitude.

Furthermore, some limitations of a stress-based approach are pointed out in [31]. Most of the critiques concern the fact that stress levels used in this procedure are in the elastic range of the materials, and for this reason a stress-based approach is not the ideal framework to be used when some plasticity occurs. This consideration, together with the ever increasing demand of design in the planned lifetime of mechanical components, led to the development of a strain-based fatigue approach, in which the amount of plastic and elastic strain is related to the number of cycles to failure.

The major contribution on the development of this theory is certain to be attributed to S.S. Manson, who firstly stated that the amount of cyclic plastic strain governs life. Several tests on different materials, in which the specimen was loaded in strain-controlled conditions, revealed that the plastic strain range can be related to the cyclic life with a power-law equation.

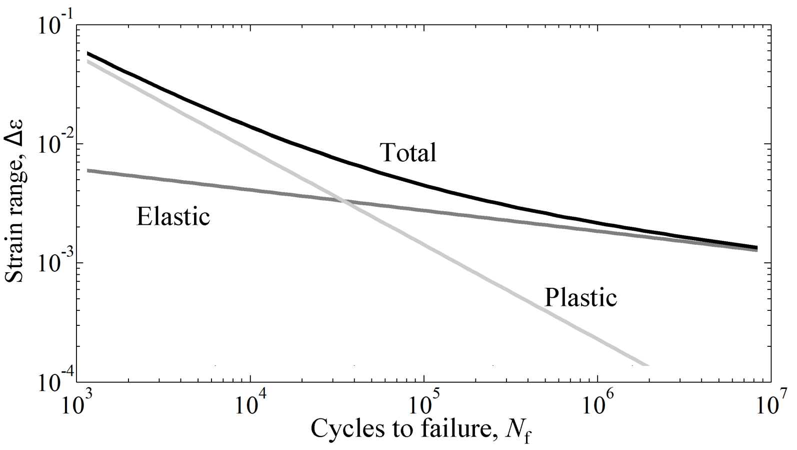

Figure 2.23: Scheme of a ε-N curve.

This rule has come to be known as the Manson-Coffin equation, because both researchers independently arrived at the same equation at about the same time. However, its direct use for engineering applications is difficult because it is difficult to measure plastic strain directly. Further extensions were then made in order to include the elastic strain range in the equations, and consequently the total strain range. The basic relation between total strain range ($\Delta\varepsilon_{tot}$) and cyclic life consists of two power-law terms: one for the plastic strain, and the other for elastic strain:

$$\Delta\varepsilon_{tot} = \Delta\varepsilon_{el} + \Delta\varepsilon_{pl} = X(N_f)^x + Y(N_f)^y \tag{2.17}$$

where X, x and Y, y are the coefficient and exponent terms related to elastic ($\Delta\varepsilon_{el}$) and plastic ($\Delta\varepsilon_{pl}$) strain range respectively, while N_f represents the number of cycles to failure. Also in this case, the coefficients and exponents should be experimentally determined with several test for each material of interest.

2.3.2 Critical Comparison

Although Wöhler and Manson proposed theories in completely different historical contests, and the representation of their results seems extremely different, a relation between the two theory exists, and it can be pointed out considering the cyclic stress-strain curve of a material. More precisely, the aim of this section is to show that an S-N curve can be converted into a strain-life pattern, obtaining the same results if Manson's approach were applied from the beginning.

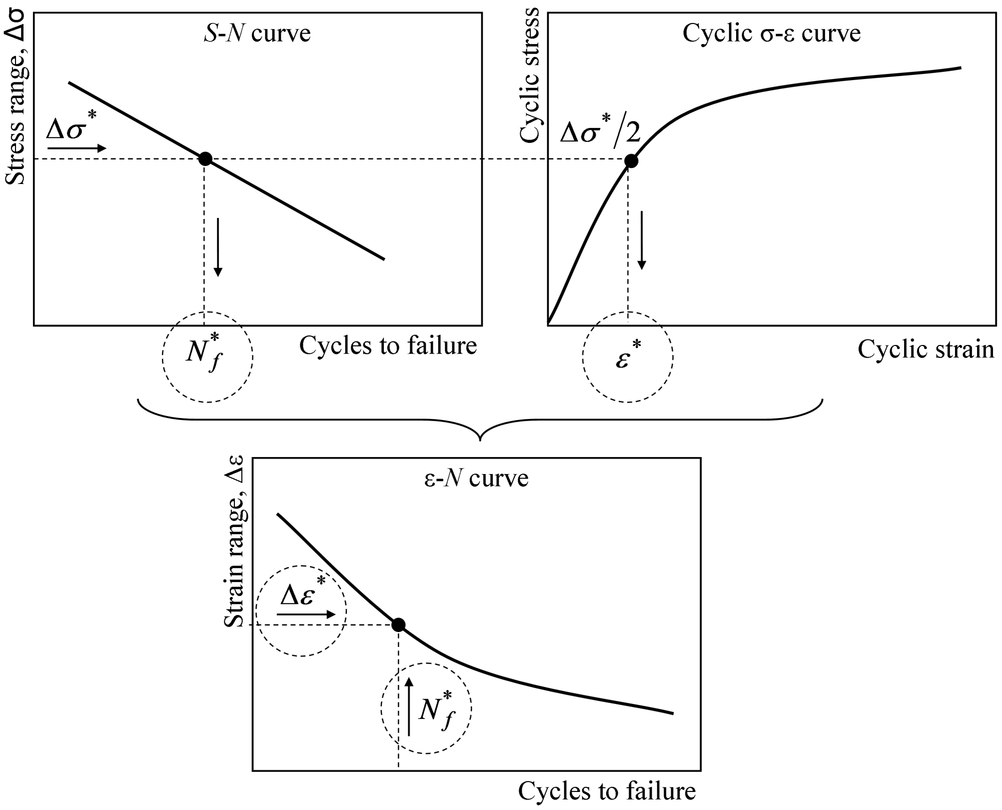

Figure 2.24: Schematic of S-N to ε-N conversion.

The basic idea is to adopt the cyclic stress-strain curve to implement the transition between the two data sets. As sketched in Figure 2.24, starting from an S-N diagram, for a given stress range ($\Delta\sigma^*$) a defined number of cycles to failure (${N_f}^*$) can be found. Adopting the corresponding stress amplitude ($\Delta\sigma^*/2$) as input for the cyclic stress-strain curve representative of the same material, a value of total strain (ε^*) can be determined . This strain level can be then related to the previously evaluated number of cycles, in a ε-N plot. The same approach can be repeated for all the data defining the S-N curve, thus obtaining a ε-N curve.

Clearly, this procedure can be followed also in the opposite direction, in order to obtain a S-N curve from a ε-N one.

In literature only few works are concerned of determining both stress and strain life relations, while the proposed strategy can be validated only with a complete set of experimental data, referring to both stress-life and strain-life curves and also to cyclic stress-strain relation for the material under investigation. Here the experimental results obtained in [43] and [44] are adopted to confirm the effectiveness of the method: an experimentally evaluated S-N is "converted" into a ε-N one, and the resulting trend is compared with measured ε-N relation for the same material.

In [43] analytic relations for S-N and ε-N curves, as well as for cyclic stress-strain relations are provided for $C45$ steel. The S-N curved is shown to be described by the following relation:

$$\log \sigma = -0.10201 \log N_f + 2.9611 \tag{2.18}$$

while the ε-N relation evaluated in the same test condition is found to be:

$$\frac{\Delta\varepsilon}{2} = \frac{1411}{E}(2N_f)^{-0.1246} + 0.4991(2N_f)^{-0.5699} \tag{2.19}$$

in which it is possible to identify the elastic and the plastic contribution according with Equation (2.17). Cyclic stress-strain curve determined in the range of controlled stress conditions is also experimentally determined:

$$\varepsilon = \frac{\sigma}{215000} + \left(\frac{\sigma}{1121}\right)^{5.5} \tag{2.20}$$

Following the procedure described in Figure 2.24 it is then easy to convert the S-N relation into a ε-N one. The first plot of Figure 2.25 clearly shows that the two curves are practically coincident.

The same approach has been followed for data available in [44], where analytic expression for ε-N and cyclic stress-strain curve are provided, while only a discrete set of values is reported in relation to stress range against the number of cycles to failure, and here summarized in Table 2.4. The ε-N curved is described by the following relation

$$\frac{\Delta\varepsilon}{2} = 0.00427(2N_f)^{-0.118} + 0.160(2N_f)^{-0.412} \tag{2.21}$$

while on the basis of values in [44], the cyclic stress-strain curve can be written as:

$$\varepsilon = \frac{\sigma}{206840} + \left(\frac{\sigma}{1441}\right)^{3.5336} \tag{2.22}$$

If converted by means of cyclic stress-strain curve, values of Table 2.4 lie on the analytical expression of ε-N curve of Equation (2.21), as clearly shown in Figure 2.26.

It is then possible to compare in a same graph a stress-based and a strain-based approach, and the agreement between the two methodologies

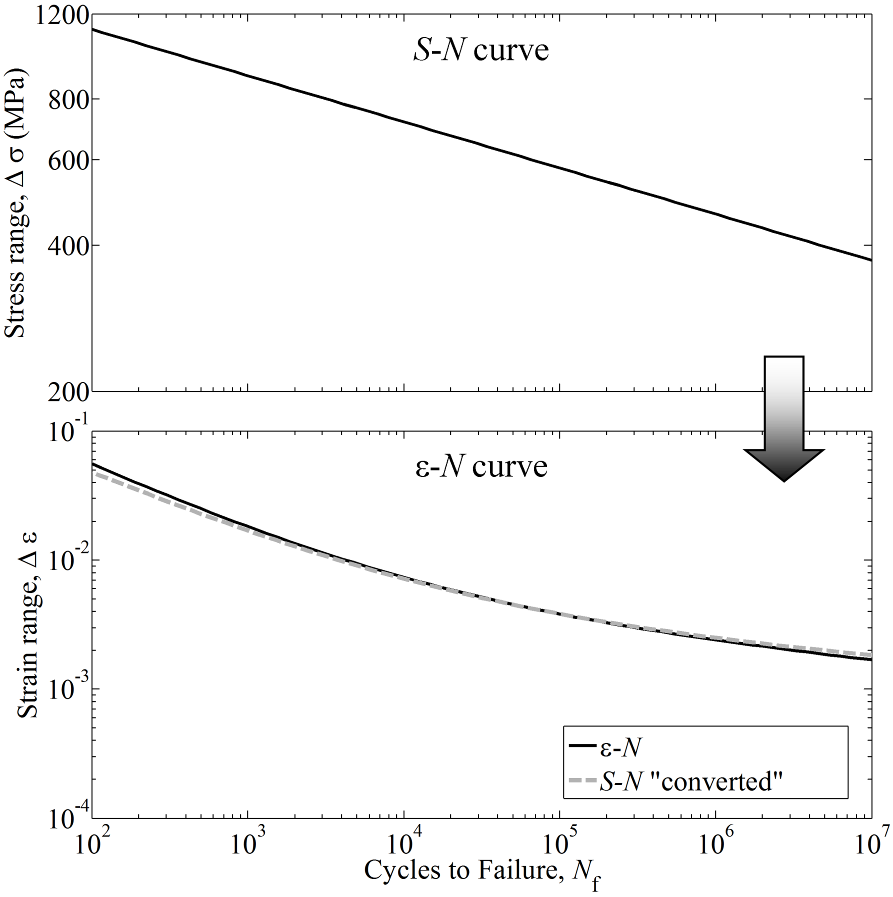

Figure 2.25: Example of conversion of S-N curve into ε-N curve. (Experimental data from [43])

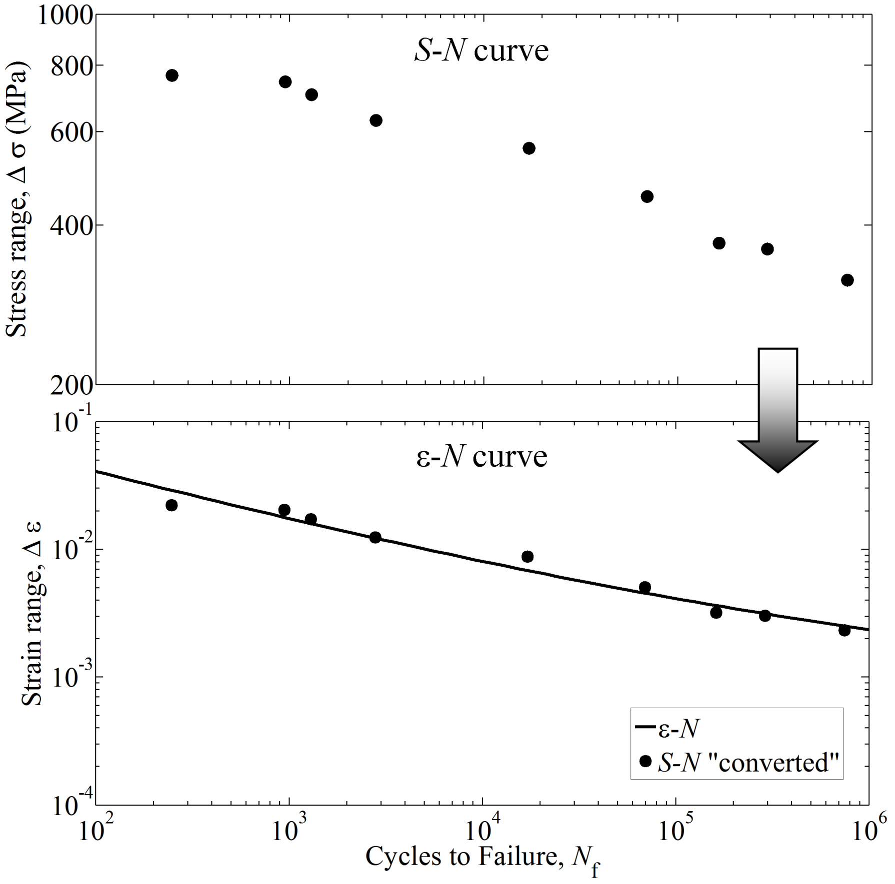

Figure 2.26: Example of conversion of S-N curve into ε-N curve. (Experimental data from [44])

Table 2.4: S-N values[a]

$\Delta\sigma$, MPa	N_f
765.2	248
744.6	950
704.6	1300
630.2	2795
558.4	17150
452.2	69500
369.6	163000
359.8	290000
314.4	750000

[a] Data from [44]

is evident: the total strain curve achieved with a ”Manson’s approach” is coincident with the total strain relation obtained from a S-N curve experimentally derived according with Wöhler philosophy and then ”converted” into a total strain relation by means of cyclic curve.

2.3.3 High Temperature and Fatigue

Fatigue is a complex phenomenon, and it can be affected by several factors. *Size* effects, as well as *surface* effects can strongly influence the performance of a given material, while the *statistical nature* of fatigue is a key-aspect to consider dealing with endurance data and evaluation of *cumulative* fatigue damage. Several works in literature, such as [45, 46, 47, 48, 49, 50, 51, 42, 9, 31] account for these aspects.

This work deals with components which are subject to thermally induced stresses, so the focus of this paragraph is on the possible interaction interaction between thermal and mechanical loads, and the role that temperature plays in affecting fatigue endurance of materials.

Thermal and mechanical loads could act individually or in a combined way on a mechanical component. *Thermal* fatigue (TF) failure is the result of temperature cycling (without external loading), as opposite to *isothermal* fatigue caused by stress-strain cycling at constant temperature [52]. It has to be noted that classic fatigue is a subset of fatigue at high temperatures, in which the temperature is kept constant at room temperature values. *Thermo-mechanical* fatigue (TMF) arise, instead, when changes in temperature and in mechanical strain act simultaneously. Figure 2.27 shows a schematic review of these fatigue mechanisms. The thermal load (T) is represented on the

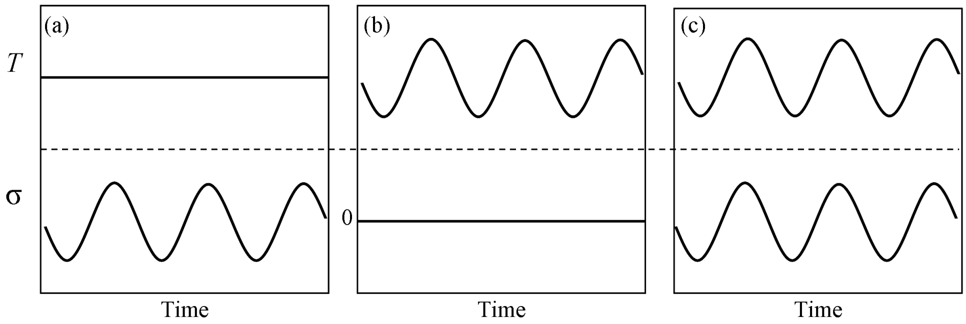

Figure 2.27: (a) Isothermal, (b) thermal and (c) thermo-mechanical fatigue.

upper portion of the graphs, while the mechanical stress (σ) is depicted in the lower part. Several combination are possible: as an example, in Thermo-Mechanical fatigue, maximum temperature peaks could coincide with maximum values of stress (in-phase cycles) or with lowest values (out-of-phase cycles). Some examples of thermal and thermo-mechanical loading in daily engineering practice are available in [53].

Fatigue damage due to thermo-mechanical cyclic loads differs from that related to only temperature oscillations, and, in general, it is difficult to perform a life prediction for thermo-mechanical fatigue on the basis of data representative of thermal fatigue, and vice versa [54, 55]. As will be shown in the following, some predictive models are available in literature to perform a preliminary assessment of fatigue performance at high temperatures.

Referring to Figure 2.27a, where only mechanical loads are considered to vary in time, further considerations can be carried out in order to understand the effect of high temperature on fatigue performances. In general, the fatigue strength of a metal decreases with increasing temperature above room temperature. At high temperatures (greater than half the melting point for the material), creep becomes important, and damage due to both fatigue and creep have to be taken into account.

The transition from fatigue failure to creep failure with increasing temperature will result in a change in the type of failure from the usual transcrystalline fatigue failure to the intercrystalline creep failure. A strain-controlled fatigue test with a holding period (hold time) during some portion of the test, can be adopted to investigate on this mechanism, because creep is allowed to take place, see Figure 2.28. In pure fatigue tests (higher frequencies and short hold times) the fatigue mode dominates and failures start near the surface and propagate transgranularly. As the hold time is increased, or the frequency decreases, the creep component begins to play a role with increasing creep-fatigue interaction. In this region, fractures are of a mixed

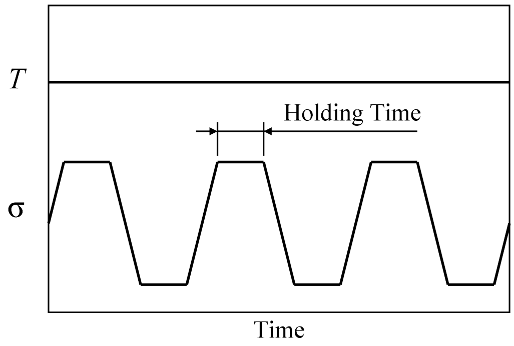

Figure 2.28: Schematic of fatigue-creep test.

mode involving both fatigue cracking and creep. With prolonged hold times, creep processes completely dominate and damage can be treated almost as pure cases of creep. The life of the component under the mixed mode can be drastically shortened, probably because the intercrystalline cracking bypasses the large number of cycles required to initiate a crack in the sub-creep range [56].

A complete review of these and others experimental approaches, as well as the description of damage rules that have been developed in order to model materials behavior under creep-fatigue conditions can be found in [42, 31, 57], while some examples of creep failures are available in [23, 58].

Considering some actions that can improve fatigue performance, it has to be noted that the metallurgical treatment which produces the best high temperature fatigue properties does not necessarily result in the best creep of stress-rupture properties. Grain size can be adopted as a key parameter to understanding this effect. In fact, while the fine grain size is desirable at room temperature, coarser grains become more advantageous in the creep range, and recent works on turbine blades provide the best performances adopting a controlled solidification with the development of single crystals with no grain boundaries [31].

2.3.4 Predictive Models

The most accurate approach to determine the fatigue characteristic of a material is to establish its behavior by actual experiment. However, it frequently is impractical to attempt an extensive experimental program either because facilities are lacking, because the simulated environmental conditions are too difficult or expensive, or because it is desirable to first scan a large number of materials in order to find a few promising ones that can later be studied more extensively. Literature data usually refer to room-temperature fatigue tests, relatively easy to be obtained, but some corrections can be applied in order to get some informations about material response at high temperatures.

It is also desirable to be able to estimate the life in advance of laboratory tests in order to appropriately choose the test parameters. Several methods have been developed for this purpose, and a comprehensive overview about these models can be found in [31]. In the following a brief summary of available techniques to evaluate the life without involving prior knowledge of fatigue behavior is given. More precisely, the possibility to realize S-N and ε-N curves on the basis of *static* tensile properties of a material is investigated, which could be of practical use in an industrial approach.

Estimated S-N curve

The usual method to describe the cyclic behavior of a material with a S-N curve if only static properties are available is to detect two distinct points into the diagram and then connect them with a straight line, in order to obtain the power relationship of Equation (2.16). As stated before, for metals this procedure is valid only in the range from 10^3 to 10^6 cycles, and in terms of stress, the lower value, corresponding to 10^6 cycles, is represented by the so-called *endurance limit*, σ_l. Through many years of experience, the ratio between the endurance limit and the ultimate tensile strength was found to range from 0.35 to 0.60, depending on the material. For steel, the

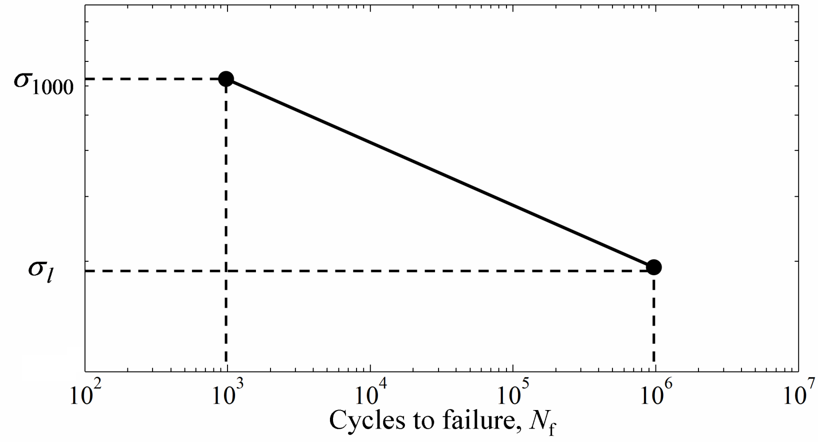

Figure 2.29: Simplified approach to obtain a S-N curve from static tensile properties.

endurance strength can be approximated by:

$$\begin{cases} \sigma_l = 0.5\sigma_{UTS} \text{ if } \sigma_{UTS} < 1400MPa \\ \sigma_l = 700MPa \text{ if } \sigma_{UTS} > 1400MPa \end{cases} \tag{2.23}$$

In addition to this relationship, for steels the stress level corresponding to 1000 cycles can be approximated by:

$$\sigma_{1000} = 0.9\sigma_{UTS} \tag{2.24}$$

Utilizing these approximations, a generalized $S-N$ curve for wrought steels can be created by connecting the σ_{1000} cycles with the endurance limit, as shown in Figure 2.29. In this case coefficient a of Equation (2.16) can be written as:

$$a = \frac{\log N_2 - \log N_1}{\log\sigma_1 - \log\sigma_2} \tag{2.25}$$

while coefficient K is directly achievable from Equation (2.16):

$$K = \sigma_{1000}^a \cdot 10^3 = \sigma_l^a \cdot 10^6 \tag{2.26}$$

Although the proposed procedure is very general, and it does not account for factor affecting fatigue, it remain useful for engineers in assessing preliminary fatigue performance starting from static tensile properties.

Estimated ε-N curve

A possible approach to establish the strain-life relation using only static tensile test properties is illustrated by Manson himself [31] and leads to the definition of Universal Slopes equation. Elaborating fatigue data for 29 different materials in the early 1960s, he noted that a good fitting of the results could be obtained adopting 0.12 and 0.6 for the slopes of the elastic and plastic line, respectively (hence the name universal slopes). On the basis of the average values, it was also possible to define the intercept point of the two lines on the strain axis at $N_f = 1$. For the elastic line, this intercept point was found to depend only on the ultimate tensile strength σ_{UTS} and the elastic modulus E. For the plastic line, the intercept point was found to depend only on ductility D, defined as:

$$D = \log\frac{100}{100 - \%RA} \tag{2.27}$$

where RA is the reduction of area in a tensile test. On the basis of these parameters, the Universal Slopes Equation becomes:

$$\Delta\varepsilon_{tot} = 3.5\frac{\sigma_{UTS}}{E}N_f^{-0.12} + D^{0.6}N_f^{-0.6} \tag{2.28}$$

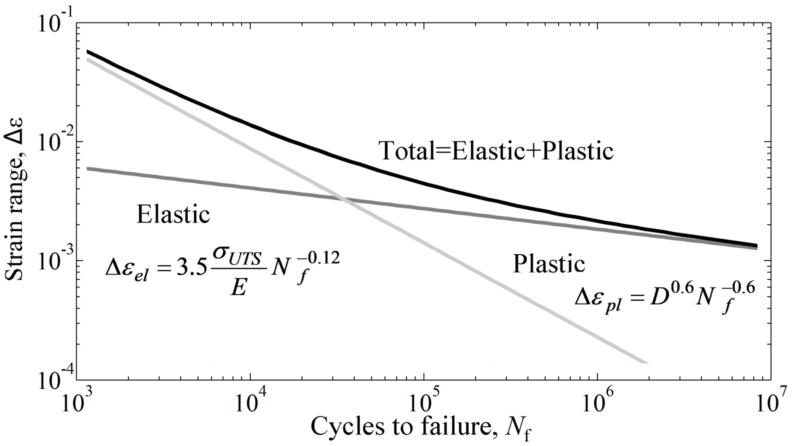

Figure 2.30: Universal Slopes method.

Thus, only the tensile properties σ_{UTS}, D, and E are required to determine the relations between cyclic life and strain range. After a more detailed experimental campaign, on the basis of data from many more materials, a modified equation has been proposed, which predicts the average fatigue behavior of the tested materials slightly better than the original equation. In individual cases, however, one or the other could be better. That is the reason why in this work only the original equation has been cited, further details about the modified method being available in [31]. A careful study of this relation reveals that when the imposed strain is high (of the order of 1 to 5%, or more, for most materials) the governing property is ductility; the higher the ductility, the longer will be the life. Below this strain range most materials benefit more from improved tensile strength than from increased ductility. So the question of trade-off between strength and ductility (generally if one increases, the other decreases) needs to be carefully evaluated on the basis of operative strain levels. Another remarkable effect concerns the fact that, even if stress is uniaxial, the strain is always triaxial. An equivalent strain range has to be then computed:

$$\Delta\varepsilon_{eq} = \frac{\sqrt{2}}{3}\sqrt{\left[\Delta\left(\varepsilon_1 - \varepsilon_2\right)\right]^2 + \left[\Delta\left(\varepsilon_1 - \varepsilon_3\right)\right]^2 + \left[\Delta\left(\varepsilon_2 - \varepsilon_3\right)\right]^2} \tag{2.29}$$

where $\Delta\left(\varepsilon_i - \varepsilon_j\right)$ is the range of the relative difference between principal strains ε_i and ε_j. In order to use $\Delta\varepsilon_{eq}$ with the uniaxial ε-N curve, the elastic part in Equation (2.28) must be corrected as suggested in [9], while the plastic line remains unchanged. The curve for total strain range is thus displaced slightly downward, the displacement being the greatest in the region of high-cycle fatigue where the elastic component dominates. The following relation is finally obtained:

$$\Delta\varepsilon_{eq} = \frac{2}{3}(1+\nu)\left(3.5\frac{\sigma_{UTS}}{E}\right) {N_f}^{-0.12} + D^{0.6}{N_f}^{-0.6} \tag{2.30}$$

The approach for high-temperature fatigue analysis on the basis of the Universal Slope equation is of great interest when treating thermal stresses problems. Equation (2.30) has been shown to provide reasonable estimates of the life at sub-creep temperatures. However, at elevated temperatures, where creep and environmental interaction may occur, this equation has been found to be non-conservative. Data from experimental tests at high temperatures give rise to the development of the 10% rule, in which approximate results can be obtained by assuming that the life under creep and environmental interaction conditions could cause as much as 90% loss of cyclic life, leaving only 10% of that calculated by the Universal Slopes Method. Results are normally expressed in terms of life bounds: the Universal Slopes Equation gives the upper-bound life, while the 10% rule gives the lowest expected life. Median expected life is estimated to be two times the lower-bound life.

This strategy is characterized by simplicity and allow a preliminary estimate of fatigue at high temperatures. Although it specifies only upper and lower bounds, and hence it cannot be adopted for refined calculations, it remains an useful tool for engineers in assessing preliminary fatigue performance at high temperatures, without the necessity to implement a creep formulation of the material.

Furthermore, as it will be proposed in the following chapter dealing with the thermo-mechanical analysis of an anode, Equation (2.30) can be improved if the relation between plastic (or elastic) strain range and life is available from literature data, or when, in presence of softening and hardening behavior, the stabilized curves are available.

Chapter 3

Steel Industry Applications

Several examples of thermal stresses problems can be found in steel industry, where the high temperatures required to produce and shape metallic products may cause relevant stresses in the constitutive elements of the plant.

Usually the design of steelmaking plants makes use of well established methodologies. In fact the uncertainties related to a strongly approximated simulation of the technological process, as well as the lack of accurate mathematical models of the structural behavior, could be easily overcome simply by over sizing the most critical mechanical elements. Recently, the demand of a strong improvement in term of productivity and reliability, accompanied by cost reduction requirements are changing completely the design approach of such components. Therefore it is necessary to take into account, often with Finite Element (FE) models, quite complex phenomena such as plasticity at different temperatures, creep, low-cycle thermal fatigue, phase transition.

These aspects have been already developed, particularly in the field of aeronautic and automotive applications. On the other hand, it is not completely clarified how these approaches can be adapted to steel making plants design. A possible approach to evaluate thermal stresses in two mechanical components of a steel making plant will be presented. Simplified, but effective, procedures are adopted due to the difficulty in achieving reliable experimental data, related to both operative conditions and to material properties, and interpretative models are provided to explain the stress-strain response under cyclic loads. Fatigue-life relations are also provided, in order to gain insights for an optimization of the component design. In particular, two elements of a steelmaking plant will be considered:

- A water cooled anode, a crucial part of electric arc furnaces.

- A copper mold, a key component in continuous casting process.

The behavior under operative conditions of these components is presented in the following, while some preliminary results have been proposed in [59, 60, 61, 62].

3.1 Thermo-Mechanical Analysis of an Anode

A possible approach for the thermo-mechanical analysis of a water cooled conductive jacket of a bottom electrode for an arc furnace is presented. The behavior after a single heating is firstly considered, in order to evaluate the influence of phase transition in modeling. The operative condition, in which the heat flux oscillates between two boundary values, is then evaluated and the response of two different sets of materials is investigated.

3.1.1 Component Description

An electric arc furnace melts the charged material by means of an electric arc. Conventional alternating current arc furnaces operate with an electric current flowing from one electrode to another through the scrap charge. The equipment needed for a direct current electric furnace shows a similar configuration, with an additional bottom electrode (anode) [63, 64]. This work deals with direct current furnaces equipped with billet type anodes, as sketched in Figure 3.1. The anode is constituted by a steel billet welded to a water-cooled copper jacket. The component has an axial-symmetric geometry and it can be considered simply supported, therefore only thermal loads have to be taken into account. The billet in contact with the steel bath may melt almost up to furnace shell due to high temperature levels reached inside the furnace. As the component is surrounded by a thick layer of refractory material, adiabatic condition can be considered along the lateral surface. The thermo-mechanical load is therefore due to a non-uniform temperature field given by an input thermal flux on the upper part of the component and a water convective cooling in the lower part. During furnace operation the thermal flux fluctuates between a lower value ($\dot{q}_{min}$) and an upper value ($\dot{q}_{max}$). The extensive melting of the billets imposes extreme working conditions on the copper jacket that may lead to severe damage. The main design requirement is to avoid the risk of crack formation on the lower part of the component that is water cooled, in order to prevent leaks of cooling fluid in the internal part of the furnace. A damage of the upper part of the component during operation could be tolerated as periodic maintenance is planned

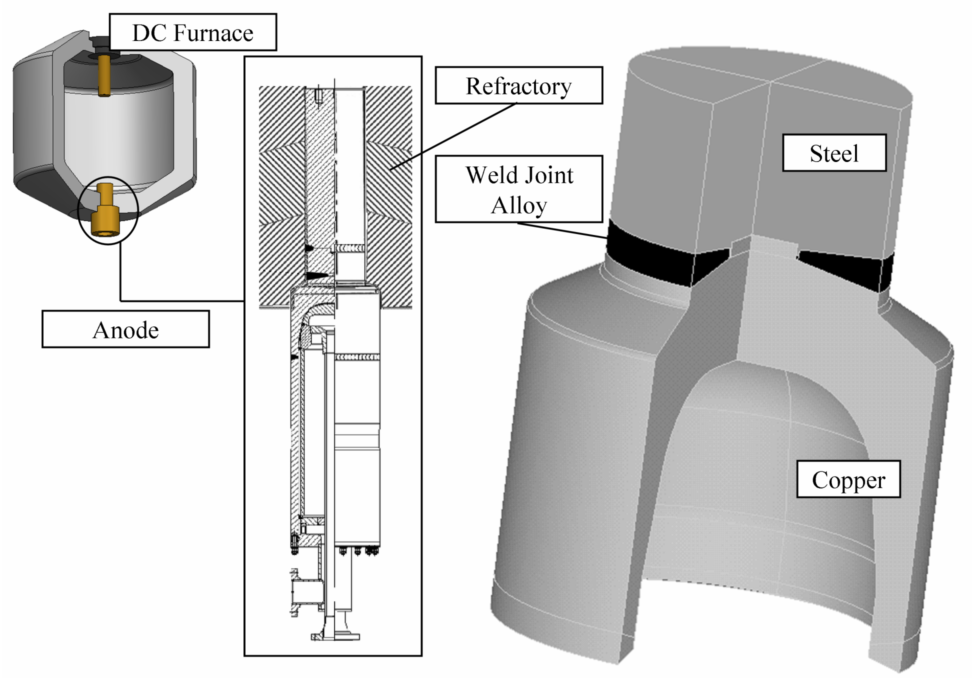

Figure 3.1: Geometry of the component [59].

when the plant is switched off and the furnace can be partially or completely emptied.

3.1.2 FE Model and Behavior After a Single Heating

The thermo-mechanical behavior of the component is modeled using the Finite Element method. Due to axial symmetry of geometry, loading and boundary conditions, a 2D axial-symmetric model can be adopted. As can be seen in Figure 3.2, the mesh is mapped for the most part of the domain and refinements are improved in the transition area between steel and copper. The strongly non-linear dependence of material properties (λ, E, σ_y) with temperature need to be taken into account. As already pointed out in Chapter 1 in the case of steel, also for copper alloys these quantities are shown to decrease with increasing temperatures [65]. Starting from a value of 390 W/m^2K 118 GPa and 70 MPa for conductivity, Young's modulus and yield strength at 20 °C respectively , a suitable variation with temperature is imposed.

Preliminary computational tests allow assessing that flux variation has a period significantly higher than that of the thermal transient observed in the model, therefore a steady state analysis is performed. Since the result-

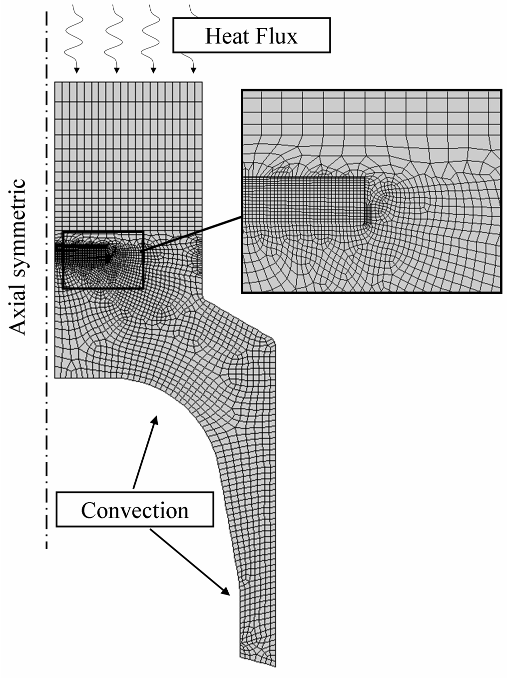

Figure 3.2: Finite element model of the component.

ing displacements do not affect the temperature field, the thermo-mechanical phenomenon is considered uncoupled. A thermal analysis followed by a subsequent mechanical analysis is then considered, as pointed out in Chapter 1.

The thermal analysis is performed imposing an appropriate (resulting from in plant measurements) thermal flux on the top of the electrode. The cooling water flowing in the inner side can be modeled imposing convective heat transfer on the lower part of the anode. In this operative conditions, the material partially melts and therefore phase changes have to be taken into account.

As previously mentioned in Chapter 1, at melting point the enthalpy shows a sharp variation, corresponding to the latent heat of the given material, which may give rise to numerical problems. Furthermore, this approach requires a transient analysis to be performed, thus strongly increasing the computational time. The alternative simplified approach illustrated in Chapter 1 is followed to reduce the computational time without introducing significant errors in results.

Considering the heating from room temperature (no input flux) to that corresponding to a thermal flux $\dot{q}_{min}$ in steady state condition, the final thermal configuration is that represented in Figure 3.3: as can be seen, this

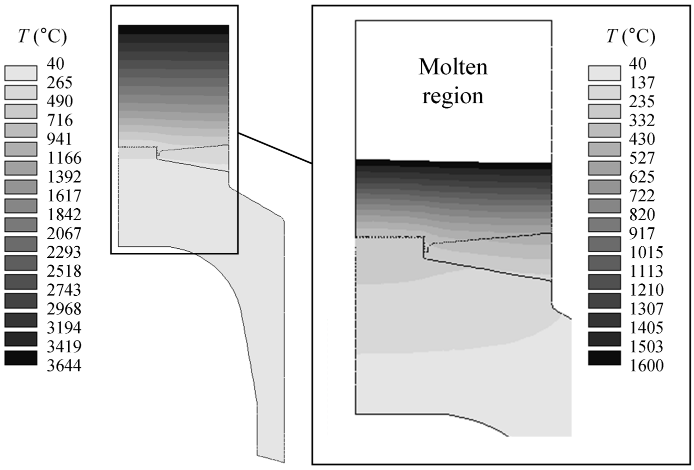

Figure 3.3: Temperature contour map after a single heating with close view of molten region [59].

steady state analysis provide results with no physic sense on the top region, where the temperatures exceed the melting point of the steel ($T_{m,steel} = 1600°C$).

As proposed in Chapter 1, the crucial point to avoid a more sophisticated transient analysis with enthalpy variation is related to a possible interpretation of the effect of the molten region on the mechanical behavior of the structure. This area is clearly identified with white color in the close view of Figure 3.3, where the temperature scale is limited to $T_{m,steel}$. This region (that is assumed to be liquid) does not affect the mechanical behavior of the underlying structure (still solid). As already pointed out, this portion simply represents a mechanical constrain at the interface between solid and molten material. For this reason three techniques have been investigated: a "lower bound", where molten elements are simply removed; an "upper bound", obtained by over-constraining displacements at the boundary nodes imposing a fictitious room temperature to the portion of anode that melts. Figure 3.5 shows the Von Mises stress (σ_{VM}) contours obtained following this strategies. It can be shown that results are quite similar, particularly if the portion close to the molten material is not considered.

According to the simplified model proposed in Chapter 1 the temperature of all elements exceeding melting point can be modified by simply imposing the melting temperature. This strategy permits to improve convergence and it also accounts for the leveling of temperatures that occurs during phase

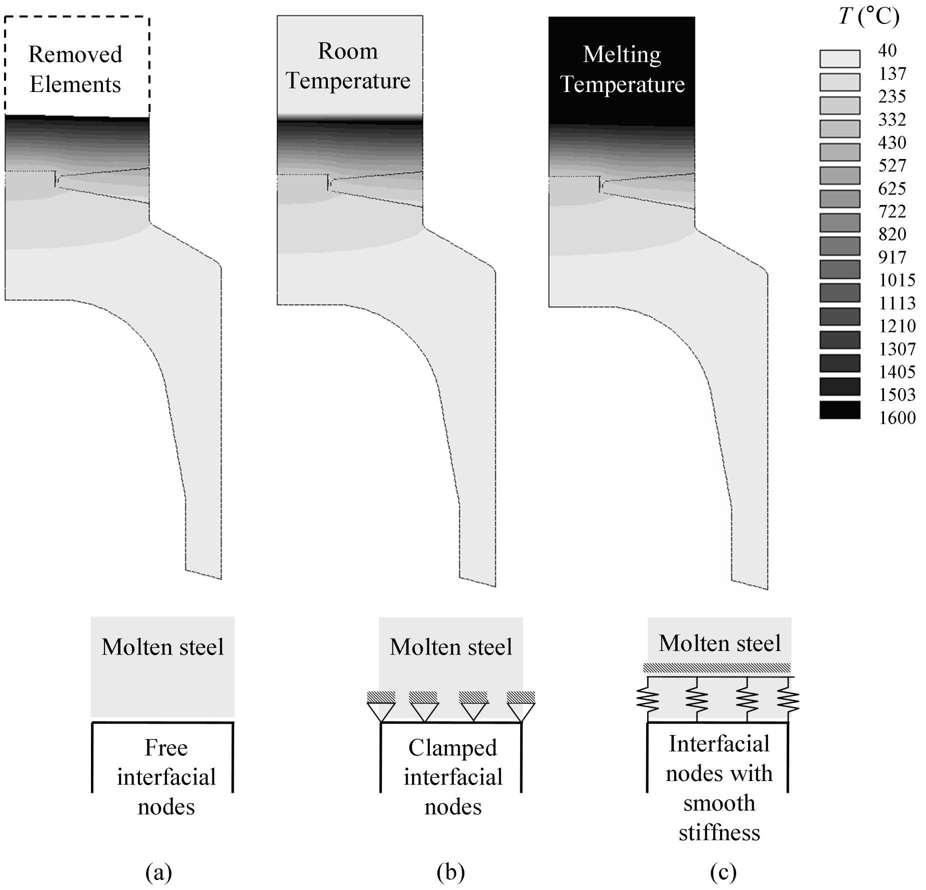

Figure 3.4: Techniques to simulate melting: (a) removed elements , (b) room temperature imposed and (c) melting temperature imposed.

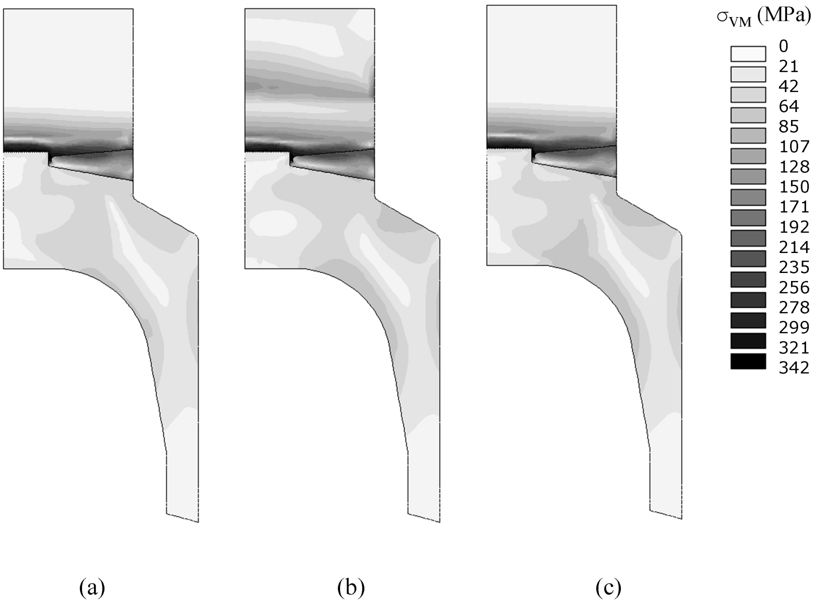

Figure 3.5: Von Mises stress contours after heating with $\dot{q}_{min}$: (a) removed elements , (b) room temperature imposed and (c) melting temperature imposed.

changes.

3.1.3 Considerations About Selected Materials

As already stated, the most critical part of the component is made of copper. The yield strength and the cyclic behavior of pure copper is strongly influenced by previous thermo-mechanical treatments. According to experimental tests performed in [41], two values were considered, respectively referring to an annealed material and to a cold worked copper. Annealed copper is shown to have very low values of yield stress, but after repeated cycles it exhibits a strong tendency to hardening behavior. On the opposite, cold worked copper tends to soften from cycle to cycle as it is loaded repeatedly. In [41] Ramberg-Osgood coefficients for the cyclic curve are provided for both materials, so the cyclic yield stress can be evaluated setting it at 0.2% of the strain and the comparison with static values is provided in Table 3.1.

As already pointed out, a numerical simulation involving hardening or softening behavior requires a huge amount of cycles to be modeled in order to achieve a stable condition, as clearly arguable from Figure 2.21. For this reason, a bilinear model with kinematic hardening is adopted, according to

Table 3.1: Parameters for annealed and cold worked copper.

		Annealed	**Cold Worked**
Static	E, GPa	118	118
	σ_y, MPa	25	230
	σ_{UTS}, MPa	211	385
Cyclic	H', MPa	326.6	418.7
	n'	0.147	0.102
	$\sigma_y^{'}$, MPa	93.5	175
ε-N	Y	0.83	0.51
	y	-0.59	-0.59

the theoretical dissertation introduced in the previous Chapter. Only the asymptotic condition represented by the cyclic yield stress is considered, neglecting the initial hardening or softening. A suitable variation of material properties with temperature is taken into account.

As it will be clarified in the following, the most critical area is subjected to cyclic strains produced by cyclic temperature gradients, occurring far from this region, which is maintained at constant temperature by the cooling fluid. It is thus possible to refer to this particular loading condition as thermal fatigue under *isothermal* condition. In particular, there is no necessity of fatigue data at high temperatures, because the considered zone does not see any temperature variation. Starting from these considerations, a relation between cyclic load and life for the two considered materials has to be found. Since the component is only thermally loaded, the total amount of strain has been shown to be insensitive to elastic-plastic model adopted, so a total-strain life methodology is followed.

As already pointed out, the basic relation between total strain range and cyclic life consists of two power-law terms, one for the plastic strain, and the other for the elastic strain. As the plastic contribution is known experimentally, a mixed approach is adopted: the plastic component is described according to Equation (2.17) with the values of the coefficient and exponent proposed by [41], while the elastic part is evaluated according to the first term on the right hand side of Equation (2.30). Since the filleted part is characterized by a biaxial stress status, an equivalent strain range $\Delta\varepsilon_{eq}$ need to be calculated, according to Equation (2.29). The following relation is obtained for the two materials, and it is plotted in Figure 3.7.

$$\Delta\varepsilon_{eq} = \frac{2}{3}(1+\nu)\left(3.5\frac{\sigma_{UTS}}{E}\right){N_f}^{-0.12} + Y{N_f}^{y} \qquad (3.1)$$

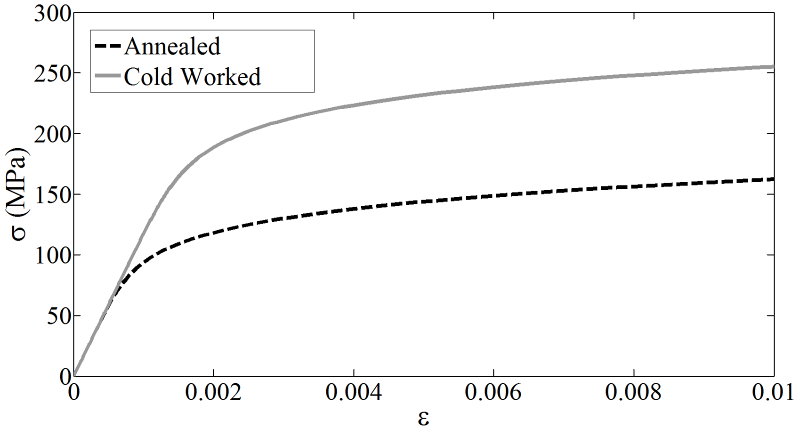

Figure 3.6: Cyclic stress-strain curves for materials under investigation.

Although cold worked material shows higher values of cyclic yield stress (even after softening), it is characterized by lower ductility (measured elongation is about 14 % for cold worked and 64 % for annealed cooper [41]). This lead to a lower response in terms of cycles to failure in the low cycle region, where annealed material shows better performances [41]. An opposite trend is observed for higher values of equivalent strain range. In fact as N_f increases, elastic strain range, that is only related to σ_{UTS}, tends to prevail. It is then crucial to investigate the stress-strain levels of the filleted region under operative conditions, in order to perform the correct material choice.

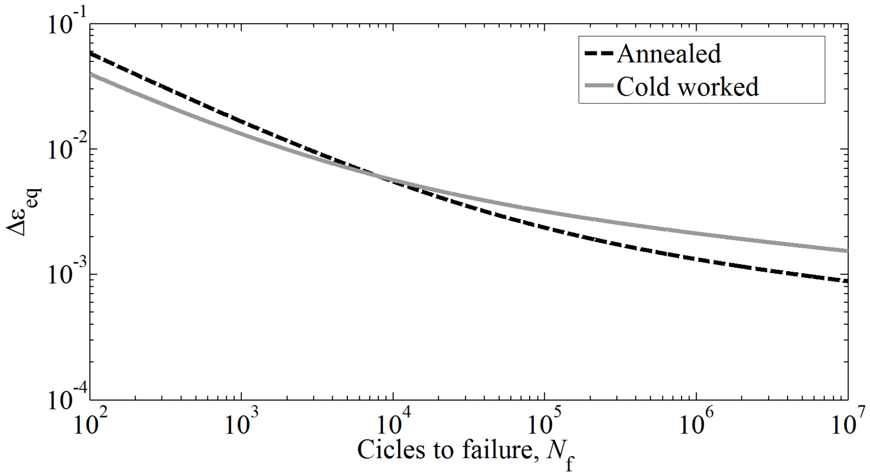

Figure 3.7: Equivalent strain range versus cycles to failure.

3.1.4 Behavior Under Repeated Thermal Loads

The thermo-mechanical analysis is performed as shown in Figure 3.8. Two thermal analyses corresponding respectively to thermal fluxes $\dot{q}_{max}$ and $\dot{q}_{min}$ are performed. According to the previously proposed methodology, those nodal temperatures exceeding the phase transition point are then modified imposing the melting temperature.

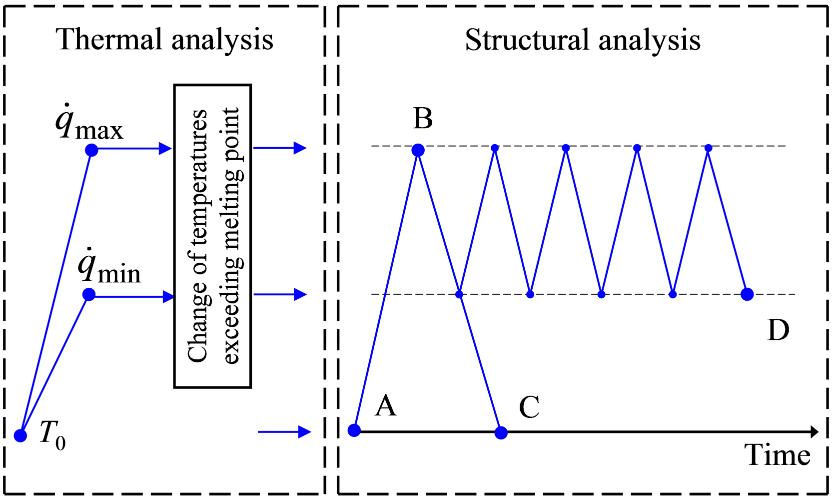

Figure 3.8: Load cycles [60].

Firstly, the simple case of the component heated up to the maximum operative conditions $\dot{q}_{max}$ and subsequently cooled to room temperature, without intermediate oscillations, is considered (ABC path in Figure 3.8). This corresponds to simulate furnace start-up and switch off and it allows to gain insights into the physic of the problem. Figure 3.9 shows the Von Mises stresses at point B and C of the cycle in the case of cold worked copper. Even if the component is only thermally loaded and free to expand, relevant stresses occur. This is particularly evident in the central portion of the component. In practice, due to the high thermal gradient and to the thermal expansion mismatch between the three different materials (steel, copper, weld alloy), free thermal expansion is partially constrained. The lower and the upper part of the component are almost free to expand and virtually stress-free. A possible interpretative model of the filleted area, according to the theoretical dissertation of Chapter (1), is that of a structure subjected to partial constraint. The part closer to the cooling fluid is maintained at constant, low temperature even if it is surrounded by a significant amount of copper material characterized by a relevant thermal gradient. As schematically represented in Figure 3.10, these areas can be compared to the two-bar assembly of Figure 1.12, where the expansion of area 2 is partially restrained by bar 1, and a stress status develops in both regions. In this particular case, due to the proximity of refrigerant fluid, area 1 is considered to be the most critical, and the choice of performing fatigue calculation referring to *isothermal* condition is here justified, because severe stress oscillations concerns a region characterized by a constant temperature.

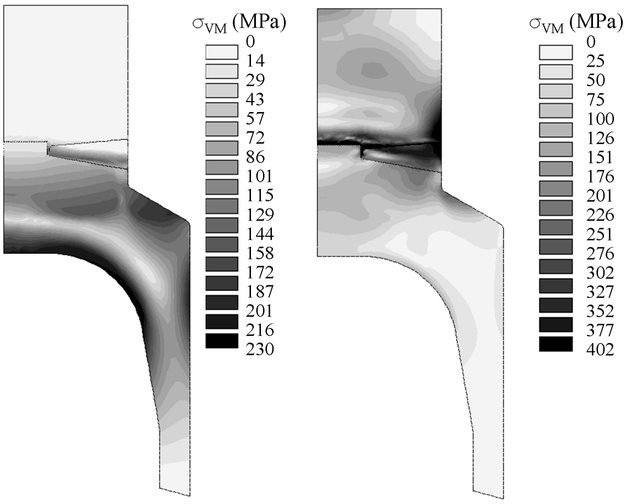

Figure 3.9: Von Mises stress contours (a) after heating up to $\dot{q}_{max}$, (b) after cooling to room temperature [59].

Figure 3.11 shows stress versus strain plotted for a sequence of cycles with a thermal load oscillating between $\dot{q}_{min}$ and $\dot{q}_{max}$ (ABD path in Figure 3.8, 10 complete cycles). The most critical point on the surface of the filleted area, where the highest values of plastic strain is reached, was considered. In this region the stress state is biaxial and thus characterized by a hoop stress and an in-plane stress, tangent to the component profile, while the radial stress vanishes. These two principal stresses are plotted in Figure 3.11 for the two materials considered in this work. After the first heating step both materials yields. A reduction of the thermal flux to $\dot{q}_{min}$ evidences a different behavior for the two materials. In the case of the annealed copper, yield occurs also in this phase, while the cold worked material shows only an elastic recovery. Further load cycles show a similar behavior. In conclusion, depending from the material properties, after the initial plastic strain corresponding to the first heating, two resulting stress cycles are obtained: the first may present a relevant inelastic deformation, the second is characterized by a pure elastic shakedown. These trends are in good agreement with those

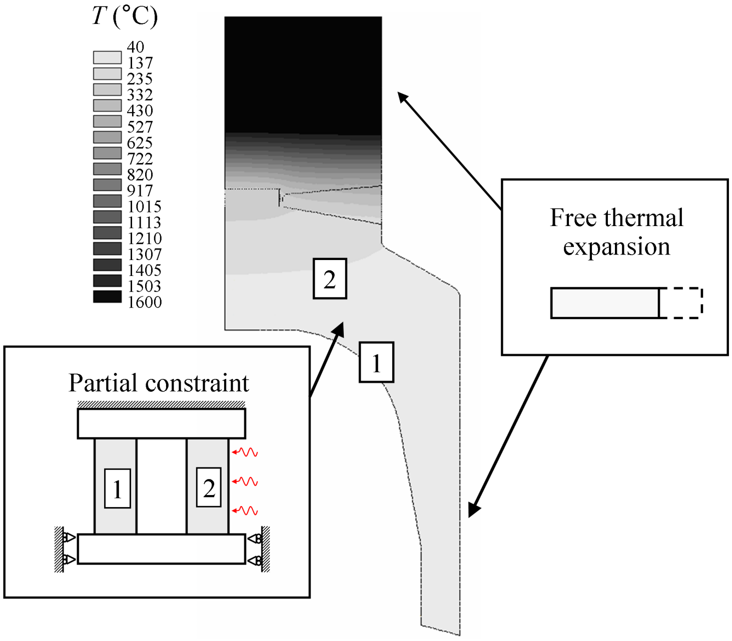

Figure 3.10: Interpretative models referring to temperature distribution.

proposed in Figure 2.2, where the effect of increasing values of ΔT has been evaluated. Here the amount of thermal load is the same for both materials, and the difference in resulting stress-strain patterns is imputable only to the difference in material properties between annealed and cold-worked copper.

The values of $\Delta\varepsilon_{eq}$ obtained from numerical analysis for the two considered materials are reported in Table 3.2. It is therefore possible to obtain from Equation (3.1) the value of N_f respectively for the annealed and cold worked material. These results are reported in Table 3.2. It can thus be shown that the cold worked material permits a longer life to be achieved.

Table 3.2: Calculated strain range and cycles to failure.

	Annealed	**Cold Worked**
$\Delta\varepsilon_{eq}$	0.0019	0.0016
N_f	212090	7289100

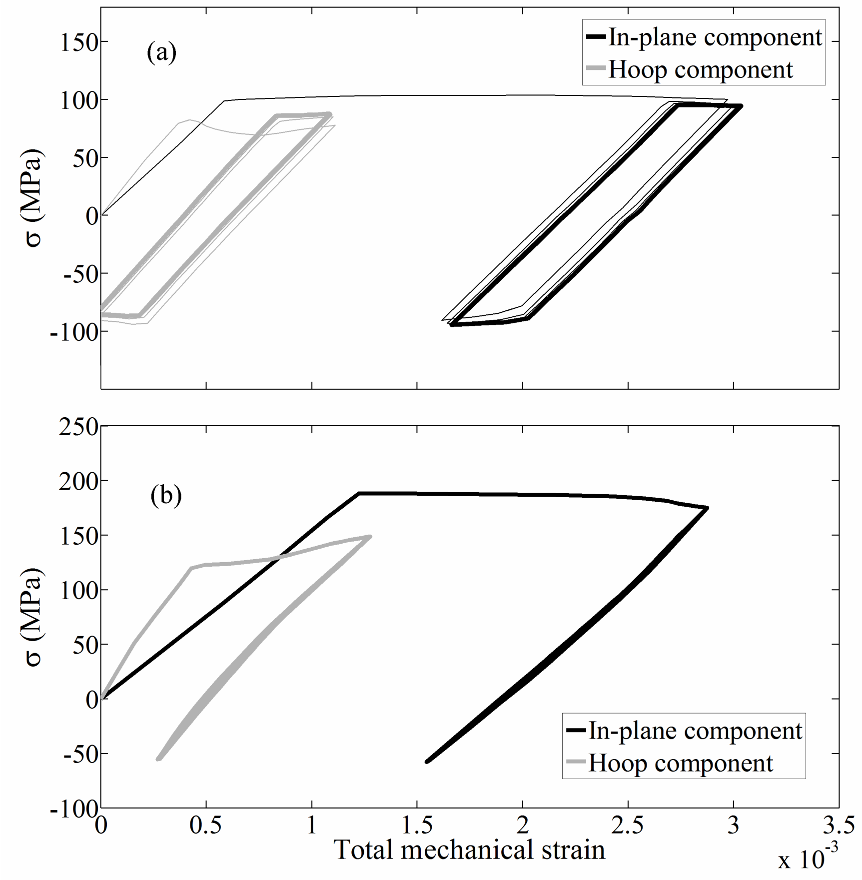

Figure 3.11: Stress-strain hysteresis loops: (a) annealed and (b) cold worked copper.

3.2 Design Improvements for a Copper Mold

This Section focuses on the thermo-mechanical analysis of a copper mold, a crucial component for the process of continuous casting of steel. Numerical and analytical models are developed to perform an accurate thermal analysis, in order to obtain some useful supports for the prediction of the residual life in actual operation; moreover the effective evaluation of different design improvement strategies can be achieved.

3.2.1 Component Description

In the continuous casting process molten steel flows through a water-cooled mold (or crystallizer) which induces the solidification of the outer shell. The main function of this component is to establish a solid shell into the steel to contain its liquid core upon entry into the secondary cooling zone. The mold is basically an open-ended box structure, usually made of a copper alloy. Different cross sections may be adopted (square, rectangular or rounded shapes) according the final geometry of the product (billets, blooms or slabs). The mold controls the shape and the initial solidification of steel, governing heat transfer and the surface quality of the product [66, 67, 68]. A reliable, crack-free mold within close dimensional tolerances is a key factor to guarantee a suitable level of safety, reliable quality and top productivity.

The molten steel induces high thermal fluxes and temperature gradients into the copper, which in turn generate high stresses levels and plastic strains, especially in the region close to the meniscus [69, 70]. After the operating period, a cooling to room temperature induces residual stresses which may increase with repeated thermal cycling over a campaign. Another source of cyclic thermal loading during operative condition is represented by the fluctuation of melt metal level, with a resulting variation of the temperature peak on the surface of the mold.

Conventional molds consist of a copper tube surrounded by a steel jacket: in the gap between the two elements cooling water flows [71]. In order to improve the thermo-mechanical performances, an enhanced design configuration has been recently developed. It consists of a thicker copper tube provided with drilled holes for cooling Figure 3.12. In this way a high stiffness with excellent heat transfer capacity are achieved at the same time. As will be shown in the following, high stress levels are still reached and the meniscus area, which is found to be the most critical for the component, can be progressively damaged. Several works in literature account for the presence of cracks in this location [72, 67], and sometimes cracks were observed after only 2 or 3 casting sequences [73]. In thin-slab continuous casters the mold

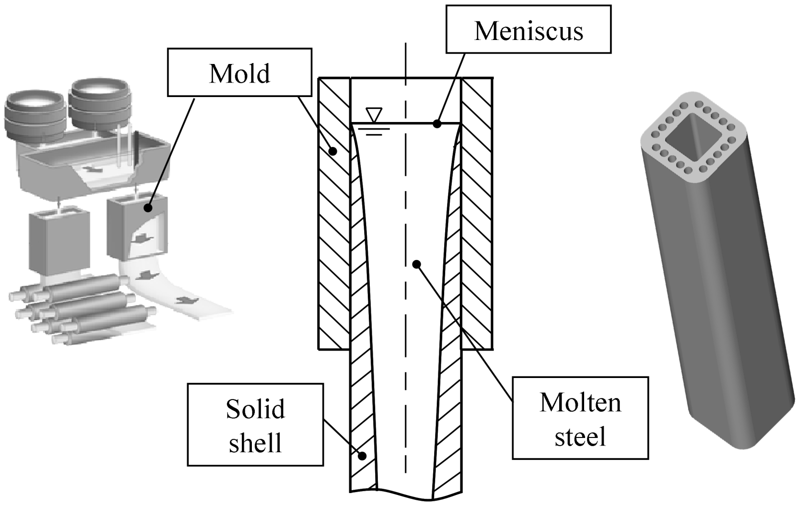

Figure 3.12: Geometry of the component [61].

surface is periodically machined to remove cracks [74], but for billet casting this practice cannot be adopted due to restrictions in the cross section.

Figure 3.13 shows the inner surface of a mold after several sequences of production at 30% productivity higher than conventional. The portion of the component subjected to higher heat loads clearly appears as a darker surface. As enhanced by the extended view, in this region several micro-cracks appear after operation.

3.2.2 Numerical Results and Interpretative Models

The component is characterized by four planes of symmetry, therefore it is possible to adopt a reduced model as represented in Figure 3.14. Even if a plane approach could be useful as a preliminary thermo-mechanical analysis, due to the non-uniform distribution of the thermal flux in the direction of the mold longitudinal axis, a three-dimensional (3D) model is necessary.

In this section a linear elastic behavior is previously considered, in order to gain insights in the physic of the problem. As it will be shown in the following, in the most critical portion of the mold, stresses exceed the elastic limit and therefore an elastic-plastic model is needed. The results of the elastoplastic analysis, which differ from the linear case only in limited localized areas, will be presented in the following sections.

The thermal analysis is performed considering an imposed thermal flux acting on the inner part of the mold, whose characteristic trend is proposed

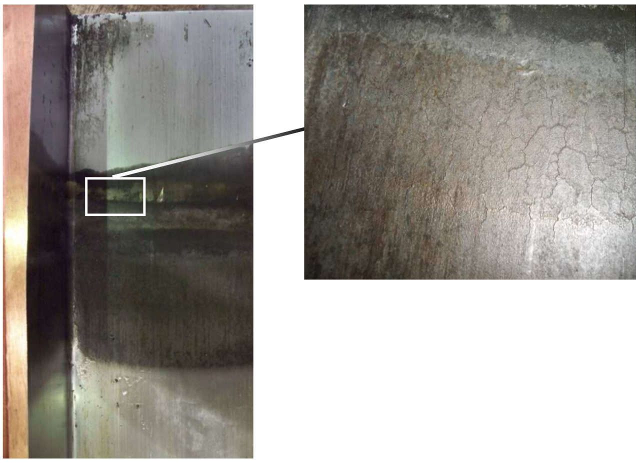

Figure 3.13: Inner mold surface with closed view of the meniscus region with cracks [61].

in [67, 69], and the steady state condition is evaluated. The outer surface is characterized by adiabatic condition, while a convective boundary condition is imposed in the inner surface of the water cooling channels. A non-linear thermal analysis is required in order to take into account the variation of thermal conductivity and specific heat with temperature. As the problem is uncoupled, a subsequent mechanical analysis is performed imposing the nodal temperature distribution obtained from the previous analysis. The in-plane and axial thermal expansion of the component are allowed. It follows that stress-strain behavior depends only on the internal temperature distribution. Also in this case a non-linear analysis is required. In fact the dependence of Young's modulus and yield stress with temperature needs to be considered. Figure 3.15a shows the temperature distribution obtained at the maximum flux in the steady state condition. It can be noticed that the

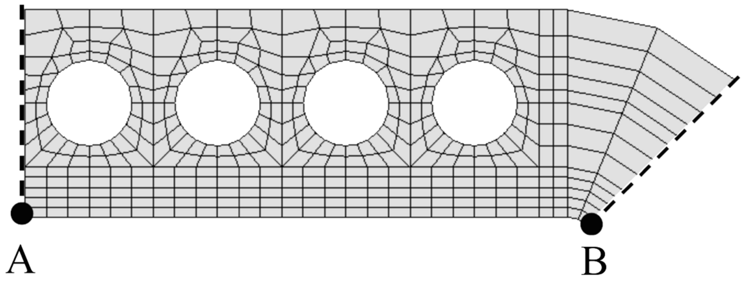

Figure 3.14: Top view of 3-D FE mechanical model [61].

maximum temperature occurs in the region close to the meniscus. If a section orthogonal to the mold axis in proximity of the meniscus is considered, it can be shown that a relevant ”radial” temperature gradient occurs up to the inner portion of the cooling pipes. In the outer part of the mold a quite constant room temperature is observed.

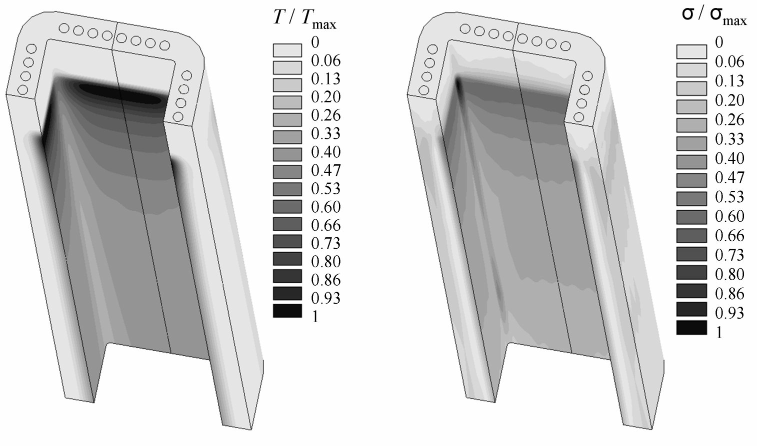

Figure 3.15: (a) Temperature and (b) stress distribution during operative condition [62].

Figure 3.15b shows the Von Mises stress distribution corresponding to the previous thermal analysis. It can be noticed that the maximum stress occurs close to the corner (point B in Figure 3.14), although higher temperatures occur at point A. The outer part of the mold shows a uniform negligible stress state. According to the procedure previously followed for the anode, some interpretative models can be adopted also to describe the behavior of some particular areas of the mold, as shown in Figure 3.16.

The stress distribution around at the corner (point B of Figure 3.14) can be interpreted using a simple structural model which refers to a square frame filleted at the corners undergoing a thermal gradient across its thickness. If the temperature variation is linear it causes a uniform bending moment and therefore maximum stresses occur at the corners which behave as curved beams. Figure 3.17 shows the ”hoop” stress variation along the thickness evaluated with the finite element (FE) model (r_e represents the outer curved beam radius), compared with that obtained according to curved-beam theory [11]: a quite good agreement can be noticed. Even if stress in point B reaches the maximum value, it occurs in the colder portion of the inner part of the component (see Figure 3.14), at a safe distance from water. It follows that the most critical portion of the mold is located at the meniscus mid-face

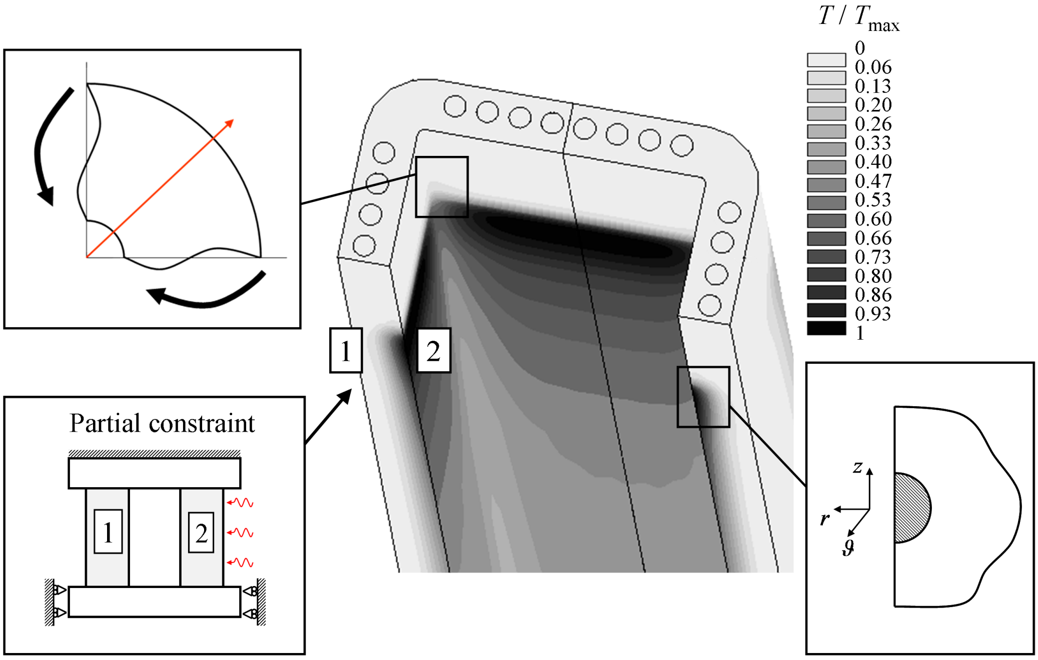

Figure 3.16: Interpretative models referring to temperature distribution.

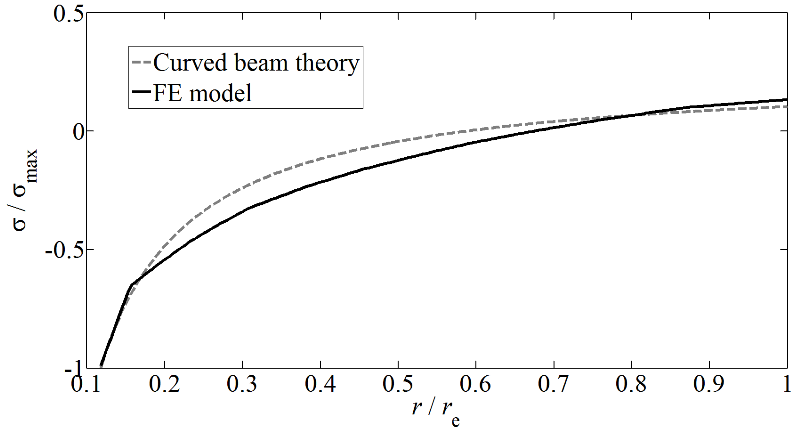

Figure 3.17: Stress variation through the thickness at the corner [62].

(point A). In order to develop an interpretative model of stress distribution in this area it is useful to investigate the principal stress pattern along the thickness. In Figure 3.18 axial, "hoop" and "radial" are represented respectively

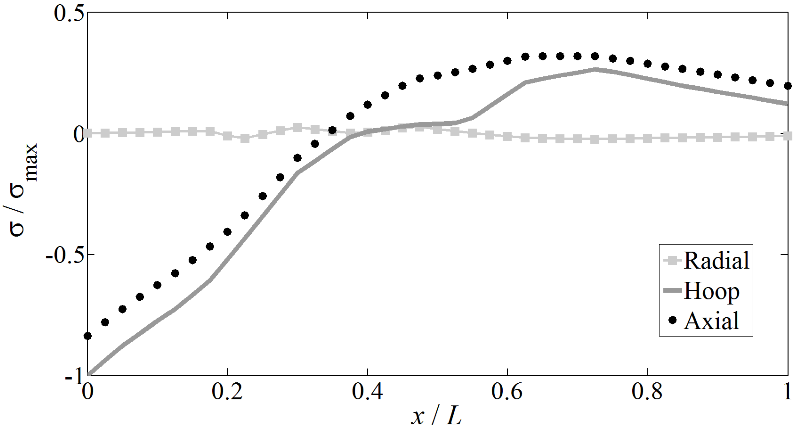

Figure 3.18: Stress variation through the thickness in the hottest part [61].

stresses (i.e. the principal stresses in the axial direction and those contained in a plane orthogonal to the longitudinal axis and respectively parallel and perpendicular to the inner mold surface). It can be noticed that the latter stress assumes negligible values in the whole range (L represents thickness). In the inner mold surface axial and "hoop" stresses show similar compressive values which decrease almost linearly maintaining quite comparable values. It can therefore be concluded that the hottest portion undergoes a plane hydrostatic state of stress, similar to that described in Figure 1.14, where a restricted region located on the surface is heated an amount of ΔT from the reference temperature, while the surrounding material is maintained at room temperature. In a cylindrical coordinate system Equation (1.66) becomes:

$$\sigma_\vartheta = \sigma_z = -\frac{\alpha E \Delta T}{1-\nu} \tag{3.2}$$

In other words a small heated part would freely expand but it is "laterally" constrained by the surrounding large cold portion.

Figure 3.19 shows the principal stress evaluated on the mold surface along the axial direction ($z = 0$ corresponds to the upper edge of the mould whose height is l). It can be clearly noticed that a plane hydrostatic stress state occurs and it is directly proportional to temperature, according to Equation (3.2). The analogy with the two-bar assembly of Figure 1.12, where the expansion of area 2 is is partially restrained by bar 1, is once again suitable

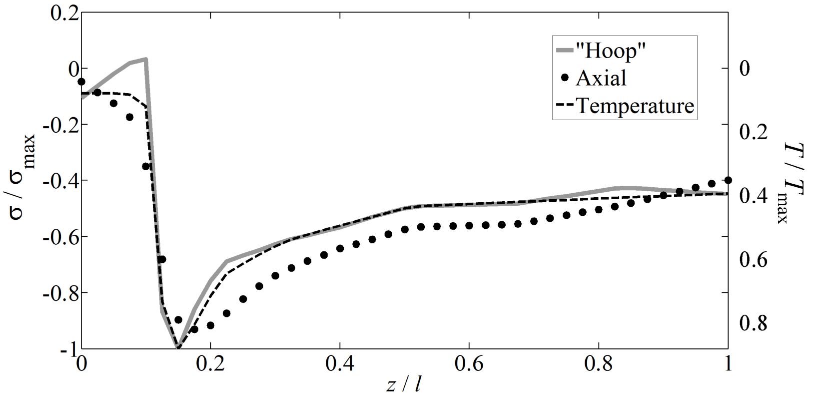

Figure 3.19: Principal stresses on the mold surface along the axial direction [61].

to describe the rising of thermal stress. Differently from the anode, here the most critical area near the refrigerant fluid is the hottest one. From a physical point of view the component can therefore be considered as constituted by two layers: an inner hot layer (that would expand) constrained by a colder layer that is maintained at low temperature by water cooling. It is thus possible to conclude that a suitable interpretative structural model of the stress and strain status in the area surrounding point A could be that of a hollow cylinder whose external part (from a radius r_f corresponding to the position of inner surface of the water channel) is maintained at constant temperature, such as depicted in Figure 3.20. The inner surface undergoes a thermal flux, and following the procedure described in Chapter 1, it is possible to find the temperature variation along the radial coordinate:

$$\begin{cases} T^A(r) = \dfrac{T_i - T_f}{\log \frac{r_i}{r_f}} \log \dfrac{r}{r_f} + T_f \\ T^B(r) = T_f \end{cases} \tag{3.3}$$

The solution in terms of stresses has the same expression of that obtained in Chapter 1 for the case of an hollow cylinder free to expand in axial direction (this condition is the most similar to the actual mold state). The representative stress state is then given by Equation (1.88), but in this case, due to the fact that the temperature is described by two functions, four constants C_i have to be determined, respectively for the inner and the outer part. The values of C_i can be analytically obtained by imposing at the interface ($r = r_i$) the compatibility condition in terms of radial displacements and the

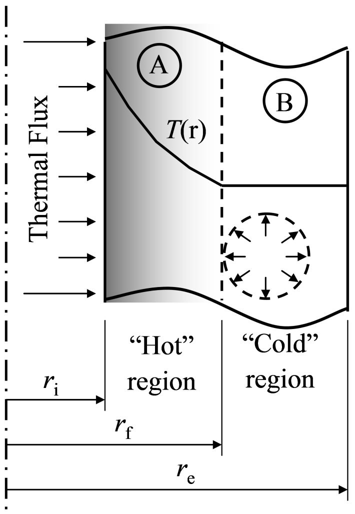

Figure 3.20: Hollow cylinder constituted by a "hot" and a "cold" part.

continuity of stresses:

$$\begin{cases} {\sigma_r}^A(r_i) = 0 \\ {\sigma_r}^B(r_e) = 0 \\ {\sigma_r}^A(r_f) = {\sigma_r}^B(r_f) \\ u^A(r_f) = u^B(r_f) \end{cases} \tag{3.4}$$

In this way the expression of C_1 , C_2 and C'_1, C'_2can be obtained:

$$\begin{aligned} C_2 &= -\frac{\frac{1}{(1-\nu){r_f}^2}\alpha C''_2 + \frac{1}{(1+\nu)C''_3}\left(\frac{1+\nu}{(1-\nu)r_f}\alpha C''_2 - C''_1 r_f\right)\left(\frac{1}{{r_e}^2} - \frac{1}{{r_f}^2}\right) + \frac{1}{(1+\nu)-(1-2\nu)}C''_1}{\frac{1}{1+\nu}\left(\frac{1}{{r_i}^2} - \frac{1}{{r_f}^2}\right) - \frac{1}{(1+\nu)C''_3}\left((1-2\nu)\frac{r_f}{{r_i}^2} + \frac{1}{r_f}\right)\left(\frac{1}{{r_e}^2} - \frac{1}{{r_f}^2}\right)} \\ C_1 &= C_2\frac{1-2\nu}{{r_i}^2} \\ C'_1 &= \frac{1-2\nu}{{r_e}^2}\left[\left(\frac{1+\nu}{(1-\nu)r_f}\alpha C''_2 - C''_1 r_f\right)\frac{1}{C''_3} + C_2\left((1-2\nu)\frac{r_f}{{r_i}^2} + \frac{1}{r_f}\right)\frac{1}{C''_3}\right] \\ C'_2 &= \left(\frac{1+\nu}{(1-\nu)r_f}\alpha C''_2 - C''_1 r_f\right)\frac{1}{C''_3} + C_2\left((1-2\nu)\frac{r_f}{{r_i}^2} + \frac{1}{r_f}\right)\frac{1}{C''_3} \end{aligned} \tag{3.5}$$

where:

$$\begin{aligned}
C_1'' =& \frac{T_f \alpha (1+\nu)(1-2\nu)}{2(1-\nu){r_e}^2} \left({r_e}^2 - {r_f}^2\right) \\
C_2'' =& \frac{T_i - T_f}{\ln \frac{r_i}{r_f}} \left(\frac{{r_f}^2}{2} \ln r_f - \frac{{r_f}^2}{4} - \frac{{r_i}^2}{2} \ln r_i + \frac{{r_i}^2}{4} - \frac{{r_f}^2}{2} \ln r_f + \frac{{r_f}^2}{2} \ln r_i \right) \\
& + \frac{T_f}{2} \left({r_f}^2 - {r_i}^2\right) \\
C_3'' =& (1-2\nu)\frac{r_f}{{r_e}^2} + \frac{1}{r_f}
\end{aligned} \tag{3.6}$$

Figure 3.21 shows the stress in radial, hoop and axial direction. By comparing Figure 3.21 with Figure 3.18 it is possible to notice a significant similarity especially in the more stressed area.

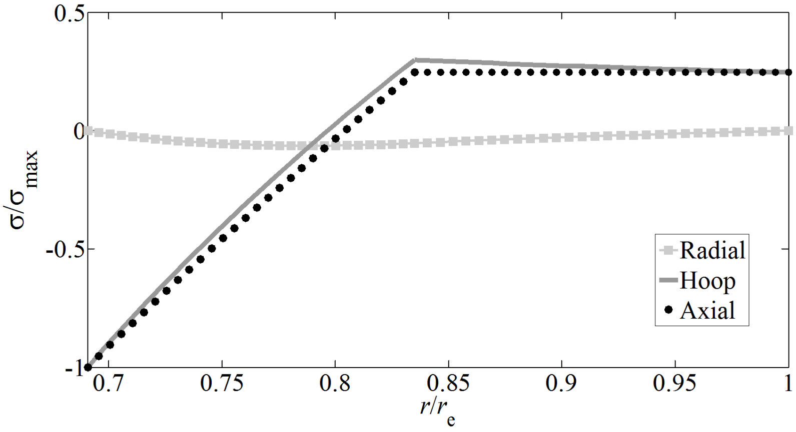

Figure 3.21: Stress distribution according to the proposed structural model.

This analytic model will be adopted in the following to quickly perform a sensitivity analysis and to evaluate the effect on stress distribution of some geometrical parameters. An optimization strategy can then be assessed.

3.2.3 Cycling Loads and Life Assessment

The component undergoes two typologies of loading cycles (see Figure 3.22 and Figure 3.23). The first one, which may be referenced as macro-cycle, is characterized by a load cycle between the condition of uniform room temperature and that one corresponding to the maximum heat flux during the

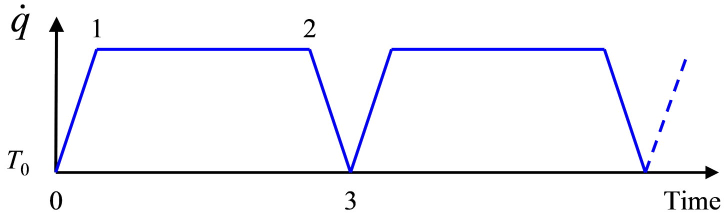

Figure 3.22: Scheme of the macro-cycle [61].

steady production. It represents the interval time production between a start-up and shut-down sequence.

The second loading condition, which may be named micro-cycle, is representative of metal-level fluctuations normally occurring during casting conditions. Mold oscillation is necessary to minimize friction of the solidifying shell, and avoid shell tearing and liquid steel breakouts, which can lead to severe damage on equipment [67]. Whereas the first load cycle occurs in a quite long period of time compared to that required to achieve the steady state condition, in the second case the frequency is high enough to establish a continuous shift in the temperature map across the nominal meniscus position. For this reason, whether in the former case a static thermal analysis could be a satisfactory approximation, for this latter condition a transient thermal analysis is compulsory, as long as a full steady state condition is never established.

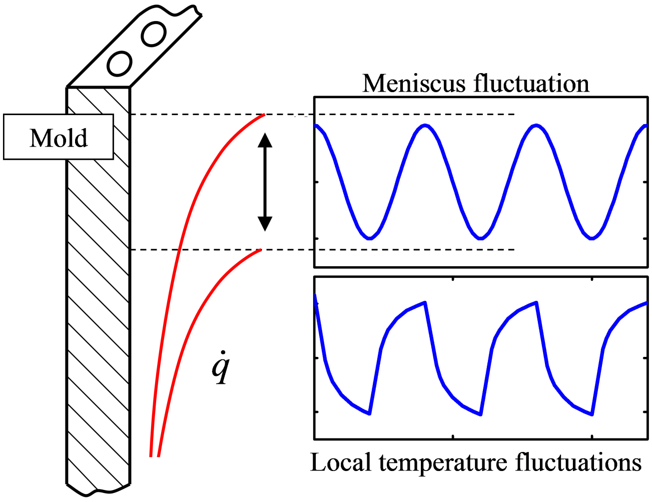

Figure 3.23: Scheme of the micro-cycle [61].

Due to the fact that in the most critical portion of the mold stresses are shown to exceed the elastic limit, an elastic-plastic model is adopted to model in a proper way the material behavior. For this purpose a bilinear model with Von Mises plasticity and kinematic hardening rule is adopted, because, as pointed out in Chapter 2, despite its simplicity, it allows to obtain accurate results dealing with thermal stress (strain imposed) problems. Cyclic stress-strain curves and their temperature dependency for the particular copper alloy adopted are available in [75]. Figure 3.24 shows the stress-strain relation in point A when the mold undergoes the two types of load cycles; only "hoop" stresses are reported, since similar trends can be obtained considering axial stresses. In the case of the "start-up and switch-off" cycles, after the first heating, a compressive stress is produced which strongly exceeds the yield strength of the material. In the subsequent cooling phase (point 3 of Figure 3.14) residual tensile stresses are produced. A value of equivalent stress slightly higher than the yield stress of the material is reached. The subsequent cycles are therefore characterized by the typical elastoplastic hysteresis loop. In the case of the micro cycles due to the meniscus oscillation, a similar behavior is produced, but in this case the yield stress of the material is exceeded only in the first heating, therefore the following cycles occur only in the elastic domain.

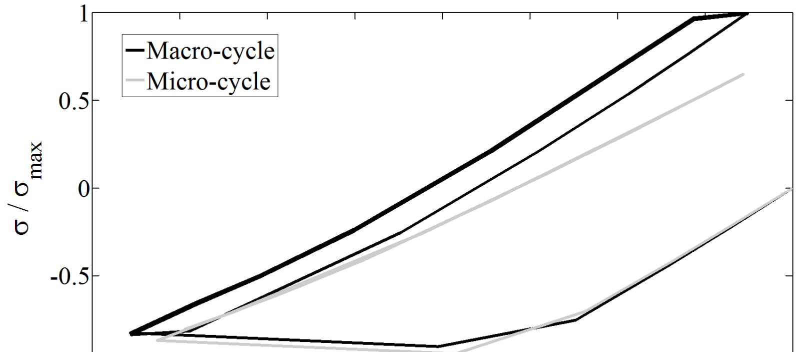

Figure 3.24: Stress-strain macro-cycles and micro-cycles [61].

The durability of the critical zone in the inner part of the mold can be then connected to the cyclic loading adopting a strain-based thermal fatigue approach. The durability analysis of continuous casting molds is deeply investigated in literature [74, 76, 75, 77]. As it is well known [73] the usual method to relate strain and life refers to the evaluation of the plastic strain range which the material undergoes. In this work a different approach has been followed, according to the considerations pointed out in Chapter 2: the mechanical component here considered is characterized by self-imposed constrained thermal expansion as a consequence of cyclic temperature gradients. It follows that the total strain depends only on temperature distribution and it is independent from the elastoplastic model of the material. A total strain range approach seems than the most appropriate choice.

Figure 3.25: Manufacturing operation to obtain the tensile-test specimens [61].

It is therefore necessary to find a relation between total strain range and number of cycles to failure, such that proposed in Equation (2.30). All the coefficients and exponents proposed in that relation need to be determined experimentally; in the case of the copper alloy considered in this work experimental data of low cycle-fatigue test are available in terms of plastic strain only [74]. Other works present correlation between total strain range and life, but in different temperature-testing conditions or for different copper alloys [76, 75]. The Universal Slopes method proposed in Chapter 2 could be a alternative approach of practical use. In fact it relates only parameter obtained from tensile test (ultimate tensile strength, ductility, and modulus of elasticity) to fatigue life for a given strain range. In order to characterize the mechanical properties of the copper alloy after use, more than 20 test specimens have been obtained (see Figure 3.25) in different locations. The results of the tensile tests are reported in Table 3.3. The values obtained show a limited scatter confirming that the material properties are not significantly affected by service condition. The elevate temperature reached in this area justifies the adoption of 10% rule to obtain the lowest expected life,

Table 3.3: Mechanical characteristics of CuCrZr alloy.

	Mean Value	**Std. Deviation**
E, GPa)	130	-
σ_y, MPa	260	21
D	0.84	0.05

while the median expected life is estimated to be two times the lower bound life.

The resulting curve is plotted in Figure 3.26. Values proposed in literature for copper alloy with chemical composition that only slightly differs from that of the material used in this work are also reported.

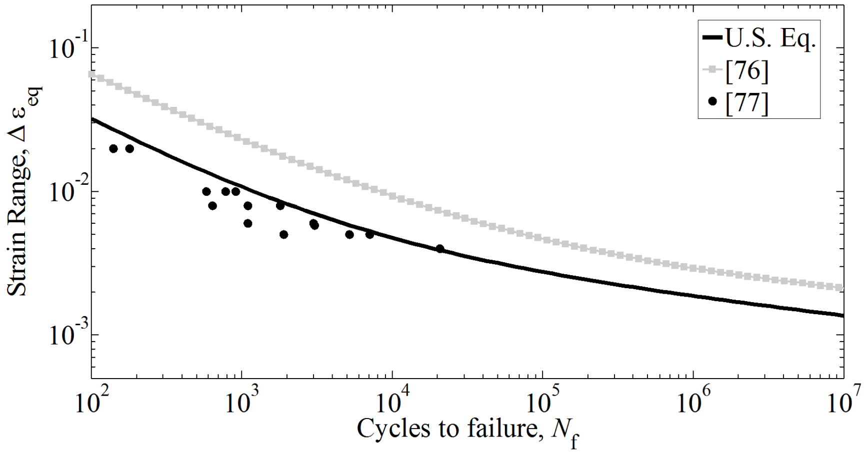

Figure 3.26: Equivalent strain range versus cycles to failure [61].

It can be noticed that the curve proposed in [76] refers to a series of test performed at room temperature; these data fits well with the Universal Slopes Equation without temperature correction. In [77] experimental test were performed at 300 °C; also in this case the obtained results are in good agreement with USE corrected with the 10% rule, and the median estimated life falls in a range between these two experimental data. These comparison seems therefore to confirm the correctness of the procedure proposed in this work. The results of the durability analysis are summarized in Table 3.4. It can be noticed that the number of cycles to failure is strongly lower in the case of the macro-cycle, characterized by a higher level of total strain range. On the other hand this result could be misleading. In fact, in a single operating sequence characterized by a start up and a switch off, a huge amount of

Table 3.4: Fatigue life calculation parameters.

	Frequency	$\Delta\varepsilon_{eq}$	N_f	N_s
Macro-Cycle	1/20 hours	0.0040	6358	6358
Micro-Cycle	0.25 Hz	0.0027	25350	1.5

micro-cycles occurs, due to the high frequency of the meniscus oscillation. Therefore, a lower number of sequences is obtained from micro-cycles. The durability of the component has to be evaluated in term of casting sequences (N_s), and from this perspective it can be noticed that in the failure analysis of the component, the strain range produced by the micro-cycle loads has to be primarily accounted for.

3.2.4 Design Improvements

The proposed models can be an useful support for the prediction of the residual life in actual operation if the tracking of the component load history is performed; moreover, they allow to define some strategies in order to improve mold's life. As already pointed out, the component is simply supported and only thermal loads are present, so stresses are self-induced in some regions where the thermal expansion is partially restrained because of the particular geometry of the mold. As a consequence, some geometrical parameters could be modified in order to obtain a lower (in absolute value) level of stress in the most critical areas. The interpretative analytical model

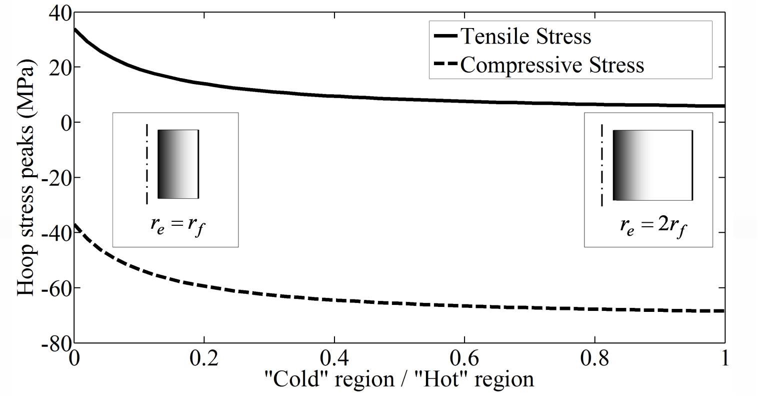

Figure 3.27: Sensitivity analysis related to width variation of cold area.

proposed in the previous Section can be of practical use to identify some useful trends.

As an example, in Figure 3.27 are represented the peak values of compressive stress (occurring at the surface) and tensile stress (in the transition area between hot and cold part) against the variation of "cold" portion width, during the heating phase. It is possible to conclude that, from a thermal stress perspective, the "cold" region should be as restricted as possible, in order to enable the greater thermal expansion of the "hot" region, thus obtaining low stress levels on the surface. On the basis of the present mold design, this result can be achieved reducing the width of material after the cooling channel system. In order to "interrupt" the circumferential fibers and their constraining effect that give rise to thermal stresses, also a portion of the corner could be removed.

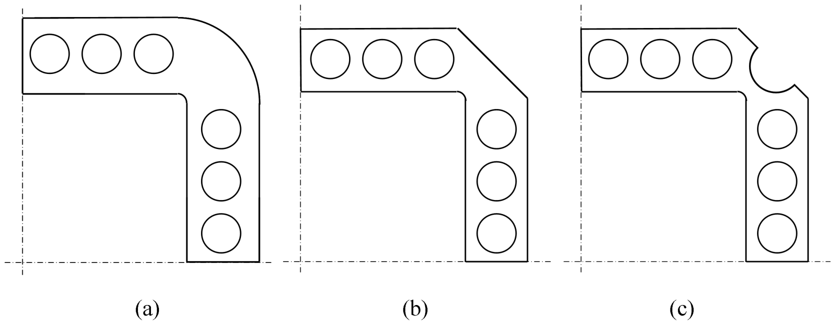

Figure 3.28: Top view of (a) reference and (b, c) enhanced mold configurations.

Some possible enhanced mold geometries are represented in Figure 3.28 against the actual configuration. Life calculations on these two configurations reveal that the increase in performances is about two and four times greater, respectively, related to the number of cycles to failure. Although these actions lead to a "less stressed" mold, they clash with the requirements of structural high stiffness that is required in order to control the shape of the product. For this reason, such geometrical changes could be adopted in the upper portion of the mold, leaving unchanged, with a suitable stiffness, the lower part. Some preliminary tests, in which the actual thermal flux is imposed in the inner part of an hollow cylinder in which the width of the upper portion is suitable modified, have been performed.

In Figure 3.29 the resultant hoop stress (axial stress shows similar trend, as depicted in Figure 3.30) is compared to that obtained in a cylinder with a constant width. It has to be pointed out that this test confirms the validity of the proposed interpretative model, because for a cylinder with constant

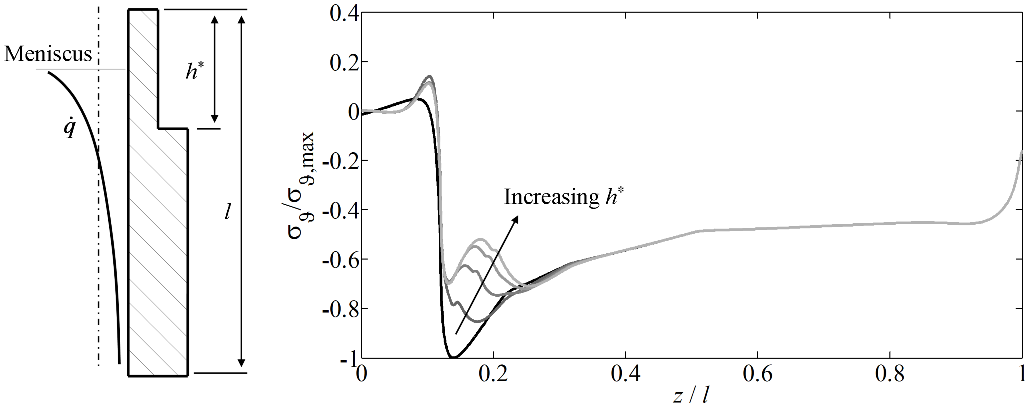

Figure 3.29: Hoop stress distribution in an hollow cylinder with a modified upper portion.

width the stress distribution is similar to that obtained for the mold along a path parallel to the component axis and passing through point A and plotted in Figure 3.19. Furthermore, if the width is reduced on the upper part, the peak values of compressive stress decrease according to the trend pointed out in the sensitivity analysis of Figure 3.27.

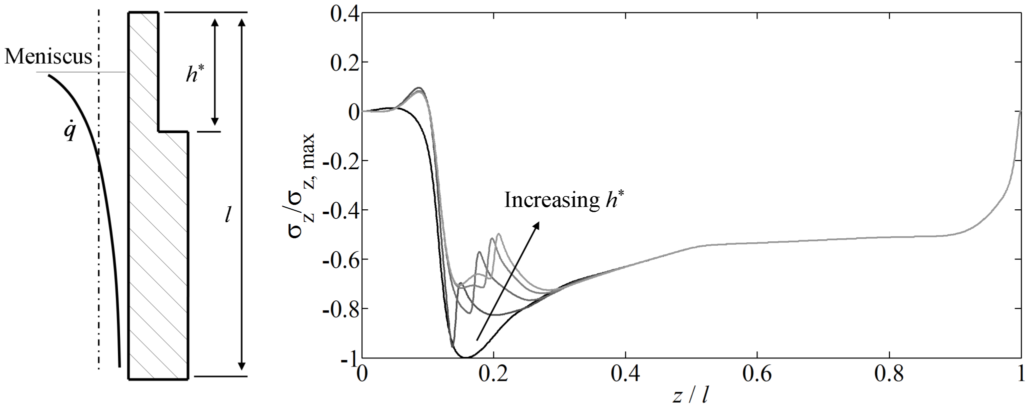

Figure 3.30: Axial stress distribution in an hollow cylinder with a modified upper portion.

A possible enhanced mold can than be that of Figure 3.31, but further analysis and in plant measurements are required in order to assess its reliability.

As previously pointed out, the strain range related to the micro-cycle

Figure 3.31: Example of enhanced mold design.

could significantly affect the life of the component. Some key parameters of optimization are then the frequency and the amplitude of the meniscus fluctuation. A sensitivity analysis has been performed, in which different amplitudes were simulated, in a realistic frequency range (values have been identified from in-plant measurements and literature review). It has to be noticed that only qualitative trends will be discussed in the following, because these informations are protected by industrial confidentiality.

As can be seen in Figure 3.32a, the amount of equivalent strain range increases if the frequency decreases for whole range of amplitudes. This result is actually quite trivial, because the ever increasing transient time give rise to an increase of ΔT. The related number of cycles to failure, plotted in Figure 3.32b, obviously shows a proportional trend: for a given amplitude, the grater is the frequency, the bigger is the amount of cycles that lead to failure. A less intuitive result is obtained considering the number of sequences to failure. In this case, the frequency of meniscus fluctuation plays an important role, and a saddle can be observed in Figure 3.32c.

As a general rule, it can be concluded that designers should avoid high meniscus amplitudes with low frequencies, and a correct evaluation of the saddle point could lead to a considerable increase in mold life.

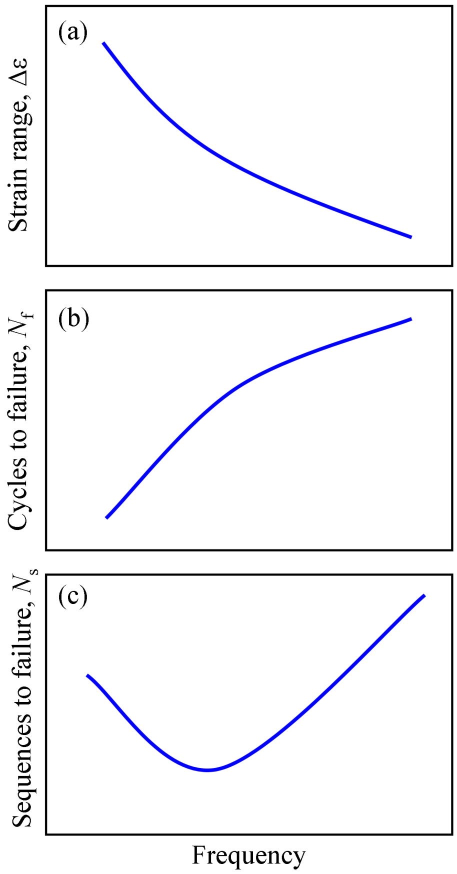

Figure 3.32: Schematic of (a) strain range, (b) cycles to failure and (c) sequences to failure against meniscus fluctuation frequency.

Chapter 4

Naval Application: Fire Doors

Fires doors are subjected to standard fire tests in order to evaluate their fire resistance. The certification process of fire doors, according to FTP code of the International Maritime Organization [78], requires to verify that the door satisfies some requirements: as an example, the mean temperature on the unexposed surface should not exceed a defined value. Furthermore, only small amplitudes of relative displacement between the door and the frame are tolerated, since no flame of smoke should pass through the door.

In this chapter the thermo-mechanical response of fire doors exposed to high temperatures is investigated. A realistic simulation of the heating process is needed during the design phase in order to reduce as much as possible the number of fire tests. Moreover, large size doors, for which an experimental trial is not feasible with standard equipment, must be tested only through computer aided simulations. The problem of defining a suitable Finite Element model (FEM) is then dealt with. The accuracy of the model is evaluated by a comparison between the response of the numerical simulation and the experimental data.

4.1 Component Description

Fire doors are one of the key elements in the fire safety design of buildings in general. They have to fulfill two functionalities at the same time: usability under normal conditions and safety and security under fire conditions. This leads to a complex structure made of different materials that are used either in the movable part (leaf) or in the fixed part (frame). In naval applications, also the athwart-ship bulkhead plays an important role, because it can not be considered as completely rigid (basically it is a steel wall with some longitudinal reinforces). Each of these parts has to show a certain thermal and mechanical stability in order to fulfill the required integrity and insulation criterion and to ensure the mentioned functionalities. The leaf is usually constituted by a steel box filled with insulation material, while the frame is composed by a structure made of steel profiles. Figure 4.1 clarifies how these parts are assembled together.

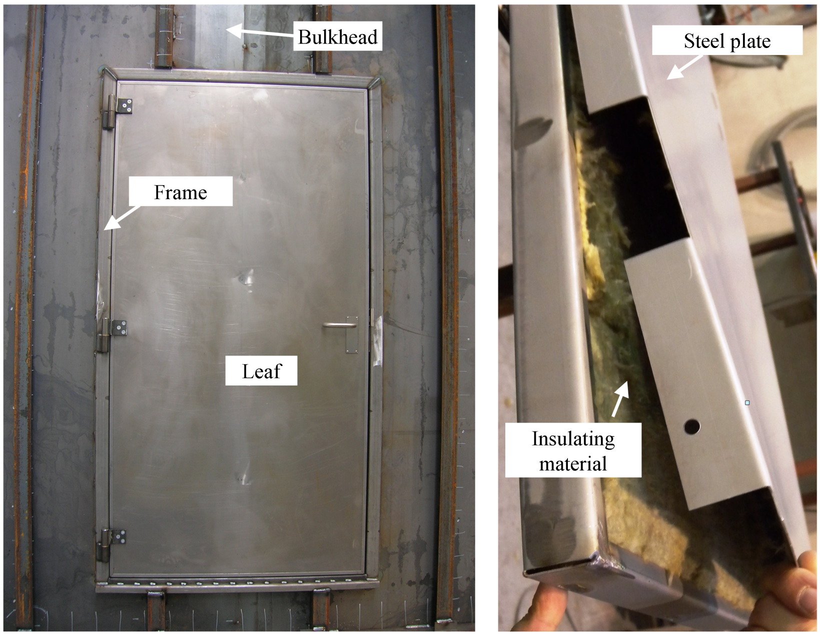

Figure 4.1: Naval fire door assembly, with a closed view of the insulating material.

4.2 Experimental Observation During Standard Fire Tests

The standard fire resistance test is carried out according to a specified standard. For naval equipments, the procedure is codified in the Fire Test Procedures (FTP) code of the International Maritime Organization (IMO). The average temperature rise on the exposed side should be according to the following temperature-time relationship:

$$T_{fi} = 345 \log(8t + 1) + T_a \tag{4.1}$$

where T_{fi} and T_a are the fire and ambient temperatures, expressed in °C, and t is the fire exposure time, in minutes.

Figure 4.2: Experimental set up: thermocouples, thermographic camera, laser sensor and real-time controller.

Endurance tests (60 minutes) are here considered. Fire doors and frames have to demonstrate the required qualifications of insulation and integrity during the entire test. Insulation is concerned with excessive temperature increase on the unexposed surface of the test specimen, while integrity failure is associated with fire spread through gaps in the test specimen [16].

All endurance tests were carried out at *Naval Suppliers* [1], a factory specialized in the production of doors and windows for naval use and off-shore, where fire doors can be tested by means of an appropriate furnace. The standard fire test furnace adopted in the tests is a vertical one (4m horizontally and 3m vertically) with four burners (two per side) that guarantee a quite uniform temperature during the heating phase. The adopted experimental set-up includes:

- A set of 12 magnetic *TC Direct* thermocouples, type *K* [2], to monitor the temperature variation on different point of the unexposed side assembly.
- 4 rigid thermocouples *TC Direct* with mineral insulation [3], located inside the furnace.
- A 16-Channel isothermal thermocouple input module *NI* 9214 [4], embedded in a real-time controller *NI cRIO*-9014 [5], used to log all the output signals from the thermocouples.
- A thermographic camera *Optris PI* 400 [6], adopted to gain insights into the heat transfer mechanisms on the unexposed side.
- A *Leica Disto D*3*a BT* laser sensor [7], to monitor the displacements in several points of the cold side.

Figure 4.2 includes some details of the adopted experimental apparatus. A sample of images recorded from thermographic camera are shown in Figure 4.4, while measurements from thermocouples are plotted in Figure 4.5.

Different fire doors were tested, and, even if each test is different from the others, some basic features were recurrent: from the thermal point of view, on the unexposed side the higher temperatures were measured near the edges

---

[1] `http://www.navalsuppliers.com/`

[2] `http://www.tcdirect.it/deptprod.asp?deptid=180/42`

[3] `http://www.tcdirect.it/deptprod.asp?deptid=190/1`

[4] `http://sine.ni.com/nips/cds/view/p/lang/it/nid/209412`

[5] `http://sine.ni.com/nips/cds/view/p/lang/it/nid/203500`

[6] `http://www.optris.com/thermal-imager-pi400`

[7] `http://www.leica-geosystems.com/en/Leica-DISTO-D3a-BT_81303.htm`

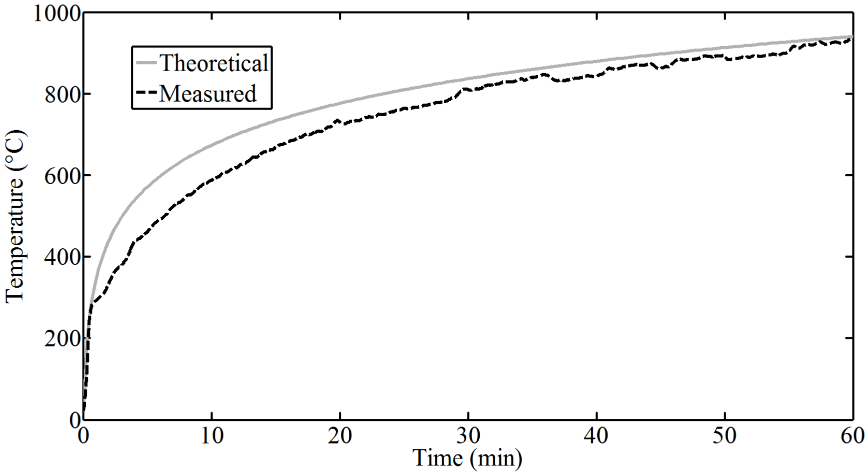

Figure 4.3: Average temperature inside the furnace.

of the door, while the central area results insulated in a better way. This suggest the presence of a thermal bridge, due to the fact that door's edges are constituted of steel with higher thermal conductivity as respect to insulation material.

The higher temperature is reached on the frame (it is not insulated), while the temperatures of the leaf and the bulkhead start increasing only after 20 minutes from the beginning of the test.

The leaf of the door usually shows the greater deformations; the most critical points, in which a dangerous gap between door and frame could arise, are found to be the corners on the lock side, as represented in Figure 4.6. On the opposite side, the presence of three hinges guarantees that displacements of door and frame are similar during the test. Measurements with a laser sensor, plotted in Figure 4.7 clearly shows that the relative displacement Δu between the leaf and the frame after 60 minutes can reach values up to 40 mm.

Although the standard fire resistance test is a convenient way for quality control and grading the relative fire performance of different types of structural members, it is could be not sufficient to completely understand the realistic structural behavior in fire. In [15] the drawbacks of the standard fire resistance test method are explained. The main concerns the fact that the standard fire exposure is only one of numerous types of realistic fire conditions: in many situations, the thermal action from the conventional fire is representative or over-designed compared to the natural fire. Nevertheless, some conditions lead to more severe thermal actions than the one from

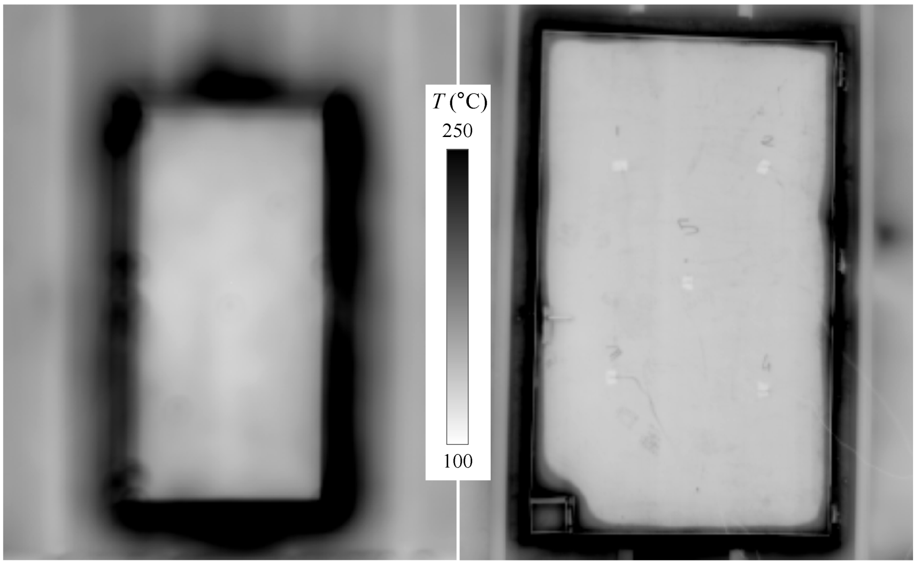

Figure 4.4: Images from thermographic camera during the test.

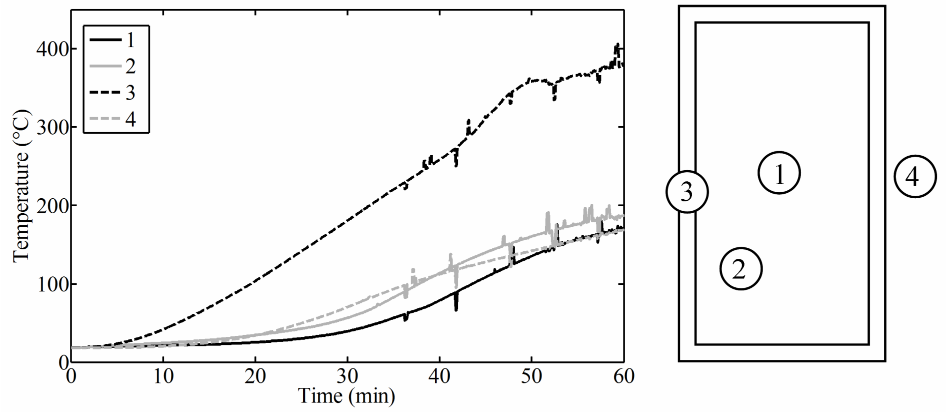

Figure 4.5: Temperature trends at different locations.

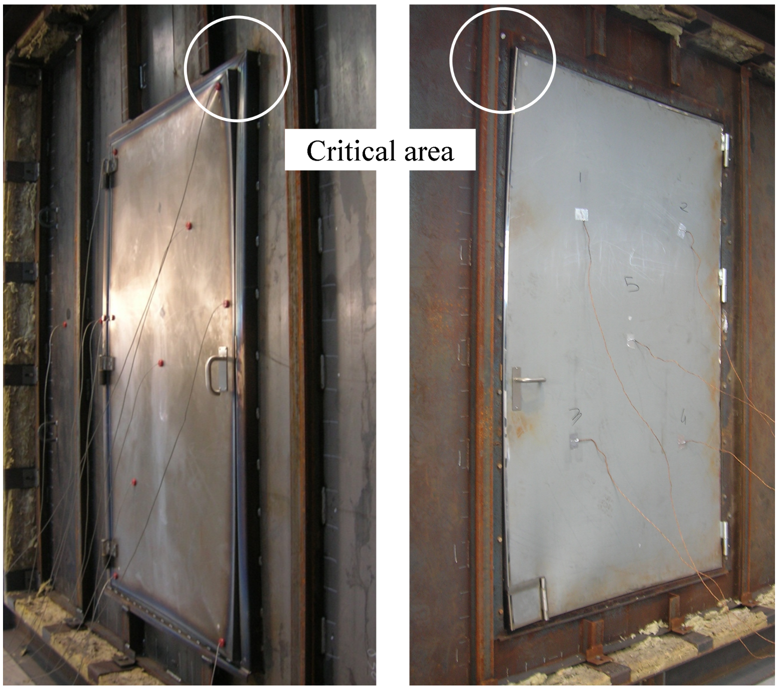

Figure 4.6: Typical deformed shape of fire doors during the test.

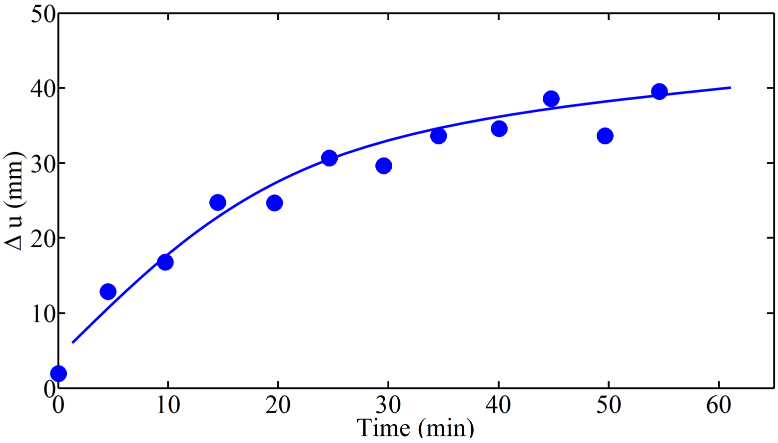

Figure 4.7: Measured gap between leaf and frame during the test.

conventional fire. Some works in literature, such as [79] , attempt to correlate real-world fires with standard fire tests, while in [80] an experimental investigation of fire doors during a natural fire is performed.

Another limitation is related to furnace dimensions: as test furnaces are restricted in size, it is generally impossible to test large elements of construction and thus only representative specimens are tested.

A well calibrated predictive model can be useful to overcome some of these drawbacks: if the model response under a simulated standard fire fits well with experimental measurements, different loading conditions, such as longer or real fire exposure, can be simulated. Furthermore, the behavior of doors with different size can be achieved (in general it is difficult to apply scaling to fire test results due to the nonlinear behavior of materials) reducing the number of tests needed for extended applications.

4.3 Thermo-Structural Analysis

From a thermal point of view, the leaf can be considered as separated from the frame. In fact heat flowing through the hinges can be neglected in preliminary calculations. In order to assess a reliable numerical strategy, only the leaf was firstly modeled. A standard leaf (2m high, 1m wide and 60 cm thick) is considered. As shown in Figure 4.8a the model takes advantage of symmetries, and it is constituted by solid (for the insulating material) and shell (for the steel plates) elements. In the close view of Figure 4.8a shell elements are depicted for seek of clarity with a fictitious realistic thickness.

The thermal analysis is performed taking into account radiative and convective heat exchange on the exposed side of the leaf, while only convection is considered on the unexposed side. As pointed out in Chapter 1, material properties vary with temperature. Suitable laws for thermal conductivity and specific heat of steel and insulating material have then been implemented, according to data available in [15, 16, 81], while values of convective and radiative coefficients are imposed according to [82, 83]. The theoretical temperature law of the furnace is then implemented in a non-linear transient analysis, and the resulting temperature distribution on the door is depicted in Figure 4.8b.

As can be seen, this model can be considered adequate to accurately describe the thermal behavior of the leaf: the temperature of lateral edges are higher than those in the central part for the presence of the thermal bridge, as experimentally observed. Furthermore, as shown in Figure 4.9b, c, the evolution of temperatures at different levels on the unexposed side is similar to the measured trend .

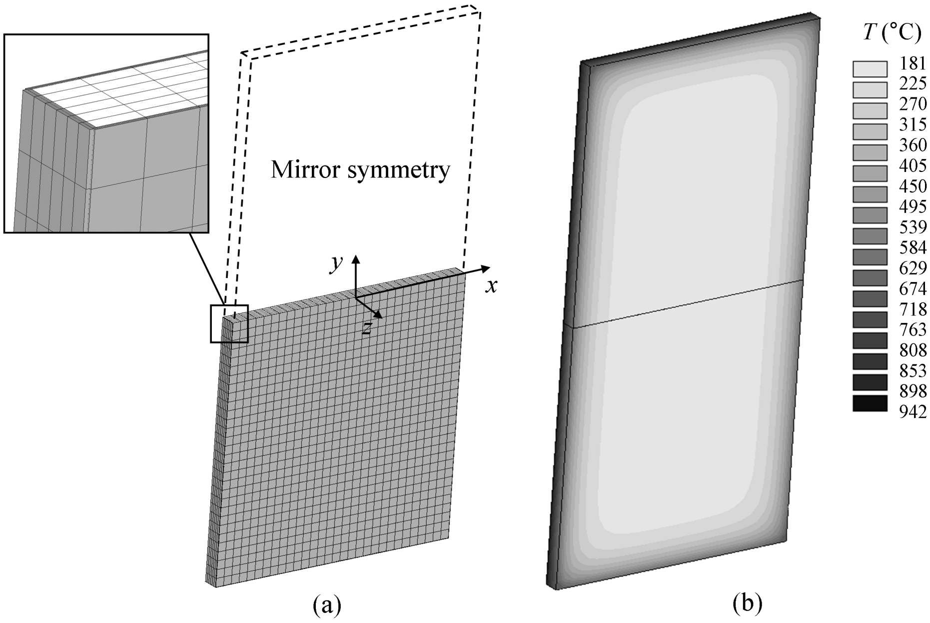

Figure 4.8: (a) Finite element model of the leaf and (b) numerical temperature distribution.

A further consideration can be made observing that the temperature on the hot side reaches the simulated furnace temperature after few minutes from the beginning of the analysis, and the final temperatures after 60 minutes are practically coincident, see Figure 4.9a. Since the slope of these curves, after the initial time interval, is not extremely high, a steady-state thermal analysis can be performed with a tolerable accuracy on the results. As depicted in Figure 4.10, the transient analysis in which radiative and convective heat exchange are considered for the exposed side, can be replaced in a satisfactory way by a steady-state analysis in which a fixed temperature (equal to the temperature after 60 minutes of the heating curve) is directly imposed on the hot side of the leaf.

Adopting this technique, the resulting temperature distribution on the cold side is very similar to that shown in Figure 4.9. The only difference is due to the fact that absolute values are somewhat higher, suggesting that the transient state is not completely concluded. Nevertheless, this drawback plays not an important role in terms of structural behavior: a preliminary structural analysis, in which the displacements of nodes corresponding to hinges positions are restrained, can be performed to assess the validity of the simplified procedure. According to [15], elastic modulus and yield stress

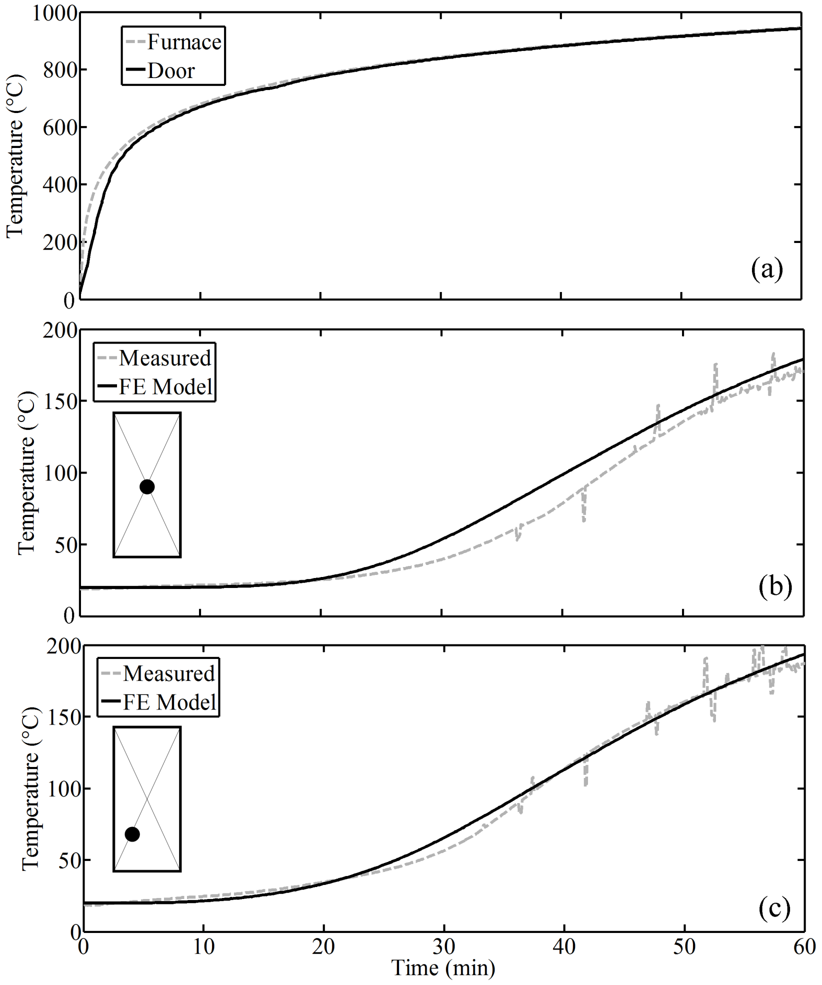

Figure 4.9: Temperatures of (a) the exposed side and (b, c) of the unexposed side.

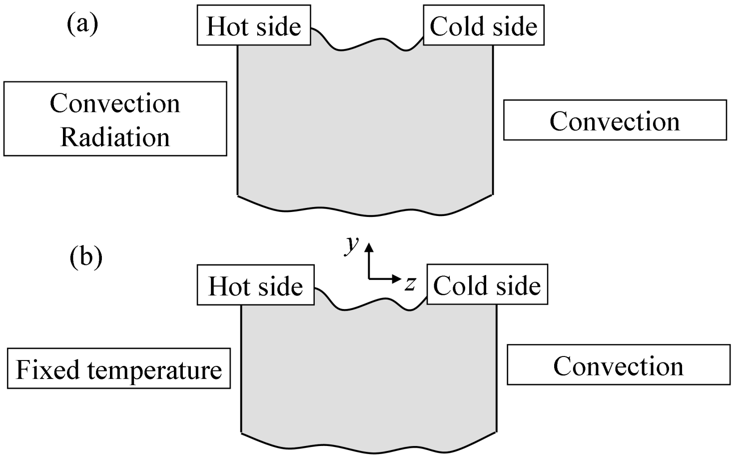

Figure 4.10: Strategies of thermal analysis implemented: (a) transient (b) steady state.

of steel are considered to vary with temperature, while insulating material shows negligible structural properties [83]. Two mechanical analysis (input temperature filed was from the transient thermal analysis for the first and from the steady-state analysis for the second) were then accomplished, obtaining similar results, in which the maximum displacement in z-direction differs only of 6%.

A complete model of leaf, frame and athwart-ship bulkhead has been then performed, in order to validate the calibration of material and simulation strategies previously mentioned, on the basis of relative displacements of the parts measured during the standard fire test.

The finite element model is shown in Figure 4.11, where some close views highlight the particular geometry of reinforcements and frame.

The temperature field obtained is represented in Figure 4.12, where a complete image of the model is represented for the seek of clarity. A rapid comparison between the simulated temperature contour map and the experimental one can be achieved by comparing Figure 4.12 and Figure 4.4. The simulated temperature is in good agreement to that provided by the infrared camera, and the presence of a thermal bridge is once again confirmed.

For the mechanical point of view, the hinges and the lock are modeled by simply coupling the displacements of the relative nodes on the leaf to follow those of the corresponding nodes on the frame.

An elastic-plastic model is implemented, in order to investigate also the unloading phase, i.e. the cooling at room temperature. This feature is needed to evaluate the correct functionality of the door after the exposure to a fire.

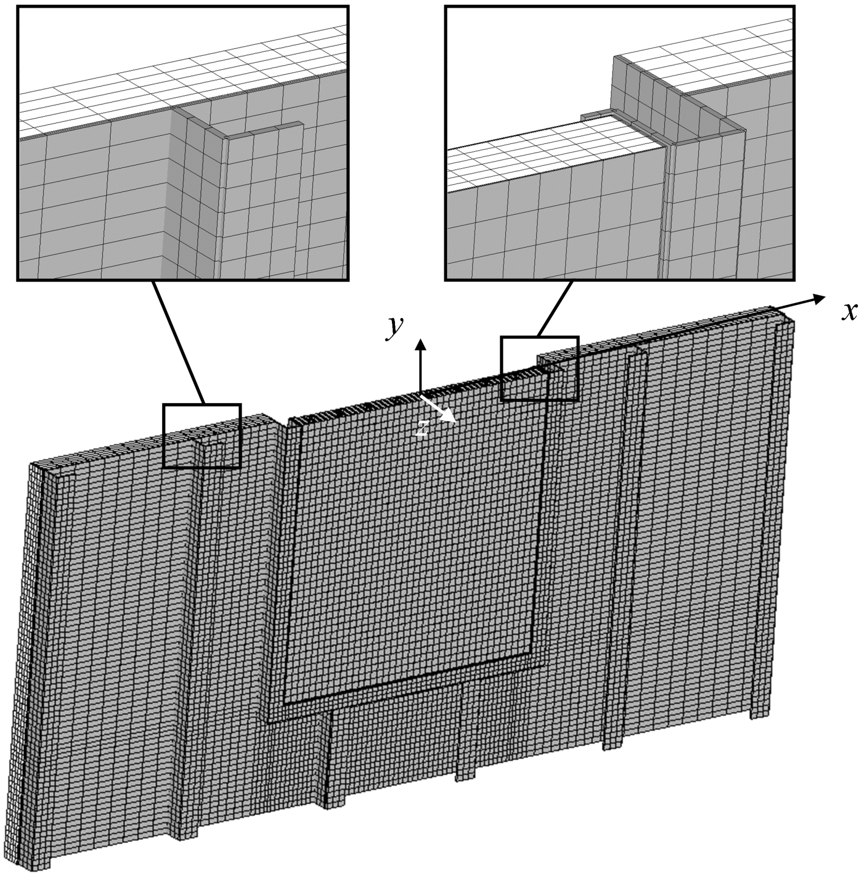

Figure 4.11: Finite element model of leaf, frame and bulkhead structure.

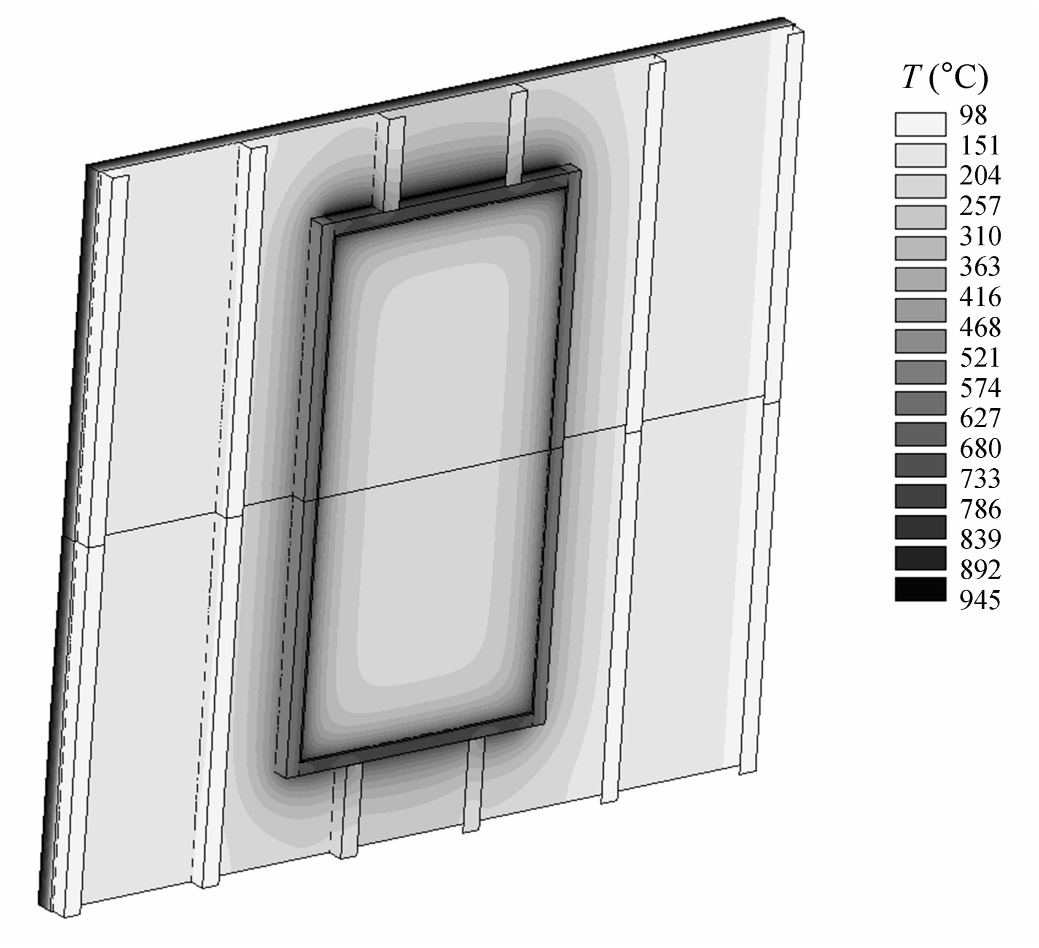

Figure 4.12: Simulated temperature distribution of the structure.

From this standpoint the model is once again in good agreement with the related fire test, and after the cooling phase the gap between the door and the frame is found to be reduced.

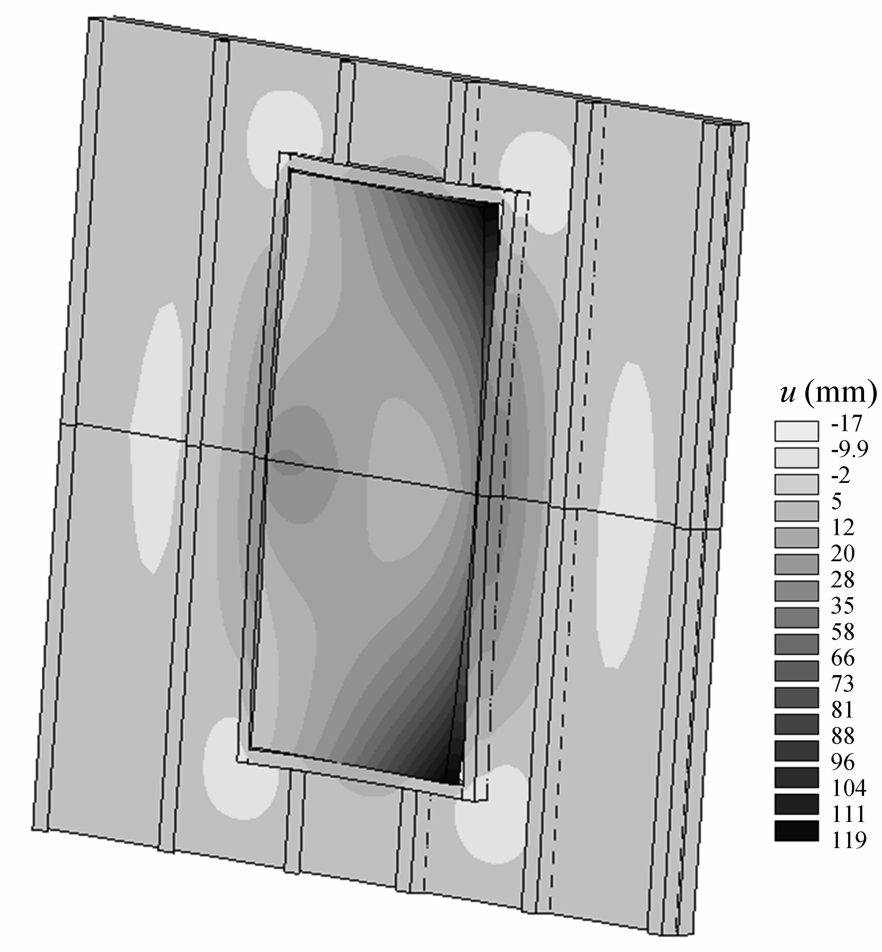

Figure 4.13: Out of plane displacements of the structure.

Figure 4.13 shows the displacement field in z-direction at the end of the heating phase. A comparison with Figure 4.6 clearly evidences that the model can correctly represent all the relevant aspects pointed out during experimental measurements. The most critical area of the leaf is represented by the two corners on the same side of the lock, and a gap between this region and the frame tends to arise during the standard fire test. The simulated out-of-plane maximum displacement is about 10 cm and is very close to that measured with the laser system.

The proposed strategy can be then considered as a valid tool in order to reduce as much as possible the number of real fire tests, to evaluate the behavior under standard fire test of large size doors and also to test fire doors with different loading conditions, such as longer or real fire exposure.

Conclusions

This research work is focused on the structural analysis of mechanical components in presence of thermal loads, with a special focus on an industry-oriented approach. In order to gain insights into mechanisms which give rise to thermal stress and to quickly assess the relevant parameters suitable for design optimization, interpretative analytical models have been developed. Material behavior under cyclic loading conditions has been deeply investigated, with the aim to individuate the best strategy to modeling cyclic plasticity and to obtain accurate life predictions in presence of thermal fatigue. Numerical models have been also implemented, paying particular attention to achieve high accuracy levels with the lowest computational time, a crucial requirement in daily industrial practice. Some highlights of these methodological aspects are summarized in the following.

Dealing with design of mechanical parts under thermal stress, a total strain approach has been proved to be the most suitable choice, at least for two reasons: total strain is directly related to restrained thermal expansion (which remains basically constant for a given temperature field); furthermore, it has been shown that total strain is not dependent from the adopted model of plasticity. This is particularly useful in evaluating the behavior of the component under cyclic thermal loads because no sophisticated models capable of describe material hardening or softening, at the expense of a huge amount of simulated cycles, are required.

Concerning the evaluation of life curves, total strain range turn out to be fundamental: in this work the well know *Universal Slopes* method is found to be suitable for practical engineering problems, when experimental static tensile tests are easy to be obtained with respect to fatigue data. A procedure to convert a stress-based life curve into a strain-based one by means of cyclic stress-strain curve is also proposed and validated on the basis of literature experimental data.

Focusing on numerical models, a suitable approach for dealing with problems involving melting has been developed: in particular, considering the effect of the molten region on the mechanical behavior of the structure, transient analysis with enthalpy variation can sometimes be avoided and a accurate solution can be achieved with a steady-state analysis.

The aforementioned strategies are adopted to evaluate in detail the thermo-mechanical behavior of three different mechanical components: an *anode* used in arc furnaces, a *mold* adopted in continuous casting processes and a *fire door* for naval applications. Although the theoretical framework and the mechanisms responsible of the rise of thermal stress are basically the same, each case study evidences some distinctive features, due to the differences in materials and loading conditions, as well as high temperature effects.

A portion of the anode was shown to partially melt during operational conditions, and the proposed approach was focused on obtain accurate results without introducing a complex modeling of melting. The evaluation of stress and strain levels in cyclic loading conditions, together with an investigation on suitable materials for the most critical area of the anode, allows to define which material permits a longer life to be achieved.

The thermo-mechanical analysis of the mold during operational conditions clearly points out that the micro-cycle, although less damaging in terms of strain levels than the macro-cycle, is responsible of crack formation in the surface due to its high-frequency. A correct evaluation of frequency and amplitude of the cyclic loads is then crucial to increase mold life. An enhanced mold shape, which should show reduced stress level on the most critical area, is also proposed on the basis of simplified analytical and numerical models.

The necessity of validate the proposed methodologies with experimental results is crucial, and temperature variation, as well as displacements induced by temperature gradients, have been monitored during several fire tests performed on standard fire doors. The conceived numerical model can correctly represent all the relevant aspects pointed out during experimental measurements, and it can be adopted as a starting point to evaluate the door behavior with different loading conditions, such as longer or real fire exposure. Furthermore, doors with different size or shape can be simulated, thus reducing the number of tests needed.

Un breve ma sentito ringraziamento ai professori
Francesco de Bona, Denis Benasciutti e Mircea Gh. Munteanu
per i loro preziosi consigli. Lavorare al loro fianco é stato per me
un onore e un piacere.

Bibliography

[1] Y.A. Cengel. *Heat Transfer - A Practical Approach*. McGraw-Hill, New York, second edition, 2003.

[2] W.M. Rohsenow, J.P. Hartnett, and Y.I. Cho. *Handbook of Heat Transfer*. McGraw-Hill, third edition, 1998.

[3] H.D. Baehr and K. Stephan. *Heat and Mass Transfer*. Springer, third edition, 2011.

[4] D. Annarratone. *Engineering Heat Transfer*. Springer, 2010.

[5] J.P. Holman. *Heat Transfer*. McGraw-Hill, seventh edition, 1990.

[6] R.F. Speyer. *Thermal Analysis of Materials*. Marcel Dekker, 1994.

[7] M. Massoud. *Engineering Thermofluids - Thermodynamics, Fluid Mechanics and Heat Transfer*. Springer-Verlag, 2005.

[8] R. Siegel and J.R. Howell. *Thermal Radiation Heat Transfer*. Hemisphere Publishing Corporation, 2^{nd} edition, 1981.

[9] S.S. Manson. *Thermal stress and low-cycle fatigue*. McGraw-Hill, 1966.

[10] R. F. Barron and B. R. Barron. *Design For Thermal Stresses*. Wiley, 2011.

[11] S. Timoshenko and J.N. Goodier. *Theory of elasticity*. McGraw-Hill, 1952.

[12] K.-J Bathe. *Finite Element Procedures*. Prentice Hall, 1996.

[13] R.D. Cook, D.S. Malkus, and M.E. Plesha. *Concepts and Applications of Finite Element Analysis*. John Wiley & Sons, third edition, 1989.

[14] R.G. Budynas and J.K. Nisbett. *Shigley's Mechanical Engineering Design*. McGraw - Hill, eight edition, 2006.

[15] J.A. Purkiss. *Fire safety engineering.* Elsevier, 2^{nd} edition, 2007.

[16] Y.C. Wang. *Steel and Composite Structures: Behaviour and Design for Fire Safety.* Spoon Press, 2002.

[17] C.A. Harper. *Handbook of Building Materials for Fire Protection*, volume 4. McGraw-Hill, 2004.

[18] V. Levitin. *High Temperature Strain of Metals and Alloys.* Wiley-VCH, 2006.

[19] J.C. Gibeling. Creep Deformation of Metals, Polymers, Ceramics, and Composites. In *ASM Handbook: mechanical testing and evaluation, Vol. 8.* ASM International, 2000.

[20] R.B. Hetnarski and M. Reza Eslami. *Thermal stresses - Advanced theory and applications.* Springer, 2009.

[21] R.K. Penny and D.L. Marriott. *Design for Creep.* Chapman & Hall, second edition, 1995.

[22] F.K.G. Odqvist. Mathematical Theory of Creep and Creep Rupture. *Oxford University Press*, 1974.

[23] H.J. Frost and M.F. Ashby. *Deformation-Mechanism Maps.* Pergamon Press, 1982.

[24] A. Weroński and T. Hejwowski. *Thermal Fatigue of Metals.* Marcel Dekker, 1991.

[25] K. Naumenko H. Altenbach. *Modeling of Creep for Structural Analysis.* Springer, 2007.

[26] S. Koric and B.G. Thomas. Thermo-mechanical Models of Steel Solidification Based on Two Elastic Visco-plastic Constitutive Laws. *Journal of Material Processing Technology*, 197:408–418, 2008.

[27] S.L. Lee and R.Y. Tzong. An Enthalpy Formulation For Phase Change Problems With a Large Thermal Diffusivity Jump Across the Interface. *International Journal Heat Mass Transfer*, 34:1491–1502, 1991.

[28] W.F. Chen and D.J. Han. *Plasticity for Structural Engineers.* Springer-Verlag, New York, 1988.

[29] J.-L. Chaboche and G. Cailletaud. On The Calculation Of Structures in Cyclic Plasticity or Viscoplasticity. *Computers & Structures*, 1:23–31, 1986.

[30] J. Lemaitre and J.-L. Chaboche. *Mécanique des Matériaux Solides.* Dunod, 1988.

[31] S.S. Manson and G.R. Halford. *Fatigue and Durability of Structural Materials.* ASM International, 2006.

[32] M.A. Miśkiewicz, H. Matysiak, and K.J. Kurzydlowsky. Finite element method modelling of the properties of a Cu-SiC composite under cyclic loading conditions. *Material Science*, 25(3):687–697, 2007.

[33] E.A. de Souza Neto, D. Peric, and D.R.J. Owen. *Computational Methods for Plasticity: Theory and Applications.* Wiley, 2008.

[34] J. Chakrabarty. *Theory of Plasticity.* Elsevier, third edition, 2006.

[35] V.A. Lubarda. *Elastoplasticity Theory.* CRC Press, 2002.

[36] G.B. Broggiato, F. Campana, and L. Cortese. The Chaboche nonlinear kinematic hardening model: calibration methodology and validation. *Meccanica*, 43:115–124, 2008.

[37] J.H. You and M. Miskiewicz. Material parameters of copper and CuCrZr alloy for cyclic plasticity at elevated temperatures. *Journal of Nuclear Materials*, 373:269–274, 2008.

[38] J.-M. Collin, T. Parenteau, G. Mauvoisin, and P. Pilvin. Material parameters identification using experimental continuous spherical indentation for cyclic hardening. *Computational Materials Science*, 46:333–338, 2009.

[39] J. Lemaitre. *Materials Behavior Handbook.* Academic Press, 2001.

[40] M. Klesnil and P. Lukáš. *Fatigue of Metallic Materials*, volume 71. Elsevier, 1992.

[41] K. Hatanaka and T. Yamada. Low Cycle Fatigue Strength of Copper and α-brass Cold-worked. *Bulletin of JSME*, 24:613–619, 1981.

[42] R. Viswanathan. *Damage Mechanisms and Life Assessment of High-Temperature Components.* ASM International, 1993.

[43] G. Szala. Comparative analysis of cyclic properties of metals obtained in conditions of stress and strain range diversification control on the example of C45 steel . *Journal of Polish CIMAC*, 6:305–312, 2011.

[44] J.F. Martin. Cyclic stress-strain behavior and fatigue resistance of two structural steels. *FCP Report N ° 9*, 1973.

[45] C.R.A. Schneider and S. J. Maddox. Best practice guide on statistical analysis of fatigue data. *International Institute of Welding*, 2003.

[46] J.A. Graham. *Fatigue Design Handbook*, volume 4. Soc. of Automotive Engineers (SAE), New York, 1968.

[47] G.E. Dieter. *Mechanical Metallurgy.* McGraw-Hill, 1961.

[48] *ASM Handbook: fatigue and fracture*, volume 19. 1996.

[49] F.C. Campbell. *Elements of Metallurgy and Engineering Alloys.* ASM International, 2008.

[50] Y. Murakami. *Metal fatigue: Effect of Small Defects and Nonmetallic Inclusions.* Elsevier, 2002.

[51] L. Susmel. *Multiaxial Notch Fatigue.* CRC Press, 2009.

[52] *ASM Speciality Handbook: Heat-Resistant Materials.* 1997.

[53] K.-T. Rie and P.D. Portella. *Low Cycle Fatigue and Elasto-Plastic Behaviour of Materials.* Elsevier, 1998.

[54] G.R. Halford. Low-Cycle Thermal Fatigue. In R.B. Hetnarski, editor, *Thermal Stresses, Vol.2.* Elsevier, 1987.

[55] A. Fissolo, S. Amiable, O. Ancelet, F. Mermaz, J.M. Stelmaszyk, A. Constantinescu, C. Robertson, L. Vincent, V. Maillot, and F. Bouchet. Crack initiation under thermal fatigue: An overview of CEA experience. Part I: Thermal fatigue appears to be more damaging than uniaxial isothermal fatigue. *International Journal of Fatigue*, 31:587–600, 2009.

[56] S.S. Manson and G.R. Halford. *Fatigue and Durability of Metals at High Temperatures.* ASM International, 2009.

[57] J.-L. Chaboche and F. Gallerneau. An overview of the damage approach of durability modelling at elevated temperature. *Fatigue and Fracture of Engineering Materials and Structures*, 24:405–418, 2001.

[58] A.J. McEvily. *Metal Failures: Mechanisms, Analysis, Prevention.* Wiley & Sons, Inc., 2002.

[59] D. Benasciutti, F. De Bona, L. Moro, M. Gh. Munteanu, M. Ansoldi, S. Morsut, and M. Picciotto. Analisi termomeccanica di un elettrodo per forno ad arco elettrico. In *40° Convegno Nazionale AIAS*, 2011.

[60] M. Ansoldi, D. Benasciutti, F. De Bona, L. Moro, S. Morsut, M. Gh. Munteanu, and M. Picciotto. Thermo-mechanical analysis of an electrode for direct current arc furnace. In *9th international AMST conference*, Mali Losinj (CRO), June 2011.

[61] M. Ansoldi, G. Bazzaro, D. Benasciutti, F. De Bona, G. Luvará, L. Moro, M. Gh. Munteanu, and F. Vecchiet. Analisi termomeccanica di una lingottiera per colata continua. In *41° Convegno Nazionale AIAS*, Vicenza (ITA), September 2012.

[62] M. Ansoldi, G. Bazzaro, D. Benasciutti, F. De Bona, G. Luvará, L. Moro, M. Gh. Munteanu, and F. Vecchiet. Thermo-Mechanical Analysis of a Copper Mould for Continuous Casting of Steel. In *International NT2F12 Congress*, Brasov (RO), May 2012.

[63] J. Jones. Understanding Electric Arc Furnaces Operations. *EPRI Centre for Material Production*, 1997.

[64] D. Hurd and J. Kollar. Direct Current Electric Arc Furnaces. *EPRI Centre for Material Production*, 1991.

[65] P. Agostinetti, M. Dalla Palma, S. Dal Bello, B. Heinemann, R. Nocentini, C. Zauner, H. Langer, and J. Klammer. Investigation of the thermomechanical properties of electro-deposited copper for ITER. *Journal of Nuclear Materials*, 417:924–927, 2011.

[66] J.K. Park, B.G. Thomas, and I.V. Samarasekera. Analysis of thermomechanical behaviour in billet casting with different mould corner radii. *Ironmaking and Steelmaking*, 29:1–17, 2002.

[67] B.G. Thomas. Modeling of the Continuous Casting of Steel - Past, Present, and Future. *Metallurgical and Materials Transactions*, 33B:795–812, 2002.

[68] J.E. Kelly, K.P. Michael, T.G. O'Connor, B.G. Thomas, and J.A. Dantzig. Initial Development of Thermal and Stress Fields in Continuously Cast Steel Billets. *Metallurgical and Materials Transactions*, 19A:2589–2602, 1988.

[69] J.K. Park, B.G. Thomas, I.V. Samarasekera, and U.S. Yoon. Thermal and mechanical behavior of copper molds during thin-slab casting (I): plant trial and mathematical modeling. *Metallurgical and Materials transactions*, 33B:1–12, 2002.

[70] B.G. Thomas, G. Li, A. Moitra, and D. Habing. Analysis of Thermal and Mechanical Behavior of Copper Molds during Continuous Casting of Steel Slabs. In *8th Steelmaking Conference Proceedings*, Chicago (IL), 1997.

[71] I.V. Samarasekera, D.L. Anderson, and J.K. Brimacombe. The thermal distortion of continuous-casting billet molds. *Metallurgical Transactions*, 13B:91–104, 1982.

[72] U-S. Yoon, J.K. Park, B.G. Thomas, and I. Samarasekera. Mold Crak Formation of the Funnel Shaped Mold During Thin Slab Casting. In *85th Steelmaking Conference Proceedings*, Warrendale (PA), 2002.

[73] J.K. Park, B.G. Thomas, I.V. Samarasekera, and U.S. Yoon. Thermal and mechanical behavior of copper molds during thin-slab casting (II): mold crack formation. *Metallurgical and Materials transactions*, 33B:437–449, 2002.

[74] T.G. O'Connor and J.A. Dantzig. Modeling the thin-slab continuous-casting mold. *Metallurgical and Materials Transactions*, 25B:443–457, 1994.

[75] A.A.F. Tavassoli. Materials design data for fusion reactors. *Journal of Nuclear Materials*, 258–263, 1998.

[76] P. Marmy and O. Gillia. Investigations of the effect of creep fatigue interaction in a Cu-Cr-Zr alloy. *Proc. Engineering*, 2:407–416, 2010.

[77] S.D. Preston, I. Bretherton, and C.B.A. Forty. The thermophysical and mechanical properties of the copper heat sink material intended for use in ITER. *Fusion Engineering and Design*, 66, 2003.

[78] International Maritime Organisation. *FTP code - International Code for Application of Fire Test Procedures*. IMO, 2012.

[79] T.Z. Harmathy. The Fire Resistance Test and its Relation to Real-world Fires. *Fire and Materials*, 5:112–122, 1981.

[80] D. Joyeux. Experimental investigation of fire door behaviour during a natural fire. *Fire Safety Journal*, 37:605–614, 2002.

[81] K. Ghazi Wakili, L. Wullschleger, and E. Hugi. Thermal behaviour of a steel door frame subjected to the standard fire of ISO 834: Measurements, numerical simulation and parameter study. *Fire Safety Journal*, 43:325–333, 2008.

[82] European Committee for Standardization. *Eurocode 3: Design of steel structures - Part 1.2: General rules structural fire design.* EN 1993-1-2, Brussels, 2005.

[83] M. Tabaddor and P.D. Gandhi. Thermo-mechanical Analysis of Fire Doors Subjected to a Fire Endurance Test. *Journal of Fire Protection Engineering*, 19:51–71, 2009.